REVEALING THE NANOSCALE STRUCTURE AND BEHAVIOR OF THE TWIST-BEND NEMATIC LIQUID CRYSTAL PHASE

by

MICHAEL R. TUCHBAND

B.S., Arizona State University, 2012

M.S., University of Colorado Boulder, 2015

A thesis submitted to the

Faculty of the Graduate School of the

University of Colorado in partial fulfillment

of the requirement for the degree of

Doctor of Philosophy

Department of Physics

2018

This thesis entitled:

Revealing the nanoscale structure and behavior of the twist-bend nematic liquid crystal phase

written by Michael R. Tuchband

has been approved for the Department of Physics

_____

Noel Clark

_____

Joseph Maclennan

Date_____

The final copy of this thesis has been examined by the signatories, and we find that both the content and the form meet acceptable presentation standards of scholarly work in the above-mentioned discipline.

Abstract

Tuchband, Michael R. (Ph.D., Physics)

Revealing the nanoscale structure and behavior of the twist-bend nematic liquid crystal phase

Thesis directed by Professor Noel A. Clark

The nematic phases of liquid crystals have been the most thoroughly investigated since the founding of the liquid crystal field in the early 1900's. The resulting technologies, most notably the liquid crystal display, have spawned an entire industry and changed our world. Consequently, the recent identification of a new type of nematic – the twist-bend nematic – was met with as much surprise as excitement, as it melds the fluid properties and environmental responsiveness of conventional nematics with the spontaneously broken symmetries and complex ordering of bent-core liquid crystals. I summarize the history of the twist-bend nematic phase, charting the development of our understanding from its first identification to the present day. Furthermore, I enumerate and highlight my own efforts in the field to characterize the behavior and nanoscale organization of this fascinating phase.

Dedication

I would like to dedicate this thesis to the many wonderful people who have supported and assisted me throughout my graduate career. Without them, much of my work might not have been possible, and my graduate career would certainly have not been as enriching.

Without guidance from my professors, my research would not have been nearly as interesting and expansive. Noel Clark's amazing physical insight enhanced the content of my work and broadened its scope. I especially appreciate our times mulling over physical models and considering all the possibilities. I'm thankful for Joe Maclennan's eye for detail and adroitness in crafting excellent writing and figures, qualities which I believe have surely rubbed off on me. Matt Glaser has an inquisitiveness and healthy skepticism which has provided me with grounding and direction in my research. I appreciate my other committee members Leo Radzihovsky and Dave Walba for their graciousness in offering me feedback in my work and in seeing me through the final portion of my graduate studies.

Throughout my days in the condensed matter basement, I valued the assistance, encouragement, comradery, and numerous helpful discussions with my many colleagues. In the last couple of years, my discussions and collaborations with Adam Green have helped me solidify my understanding of the physics of liquid crystals. He also nurtured my appreciation for science fiction literature and cinematography, among many other things. I will always fondly remember our many conversations and weekly trips with Cheol Park to get Thai food. I learned about liquid crystals and struggled with FFTEM alongside Min Shuai throughout my graduate career, and I benefitted greatly by her experimental intuition and understanding. Until 2017, Art Klittnick was a permanent fixture in the Univerity of Colorado Boulder's liquid crystal physics lab. I appreciate

him immensely, not only for assisting me with technical issues and custom solutions to my experiments, but for cultivating in me my appreciation for the amazing abundance of nature around us. I will always cherish our interactions. Renfan Shao provided me my first introduction to liquid crystal physics and polarized light microscopy, along with continued technical guidance, for which I am very grateful. I appreciate the opportunity to guide Keri Graber in her research in liquid crystals and I wish her luck in her future. Dong Chen, my graduate student mentor early in my career, helped me get up to speed on the group's experimental techniques and in scientific writing, permitting me to become productive in the group very rapidly, for which I am grateful.

The graduate students and researchers in the CU Boulder chemistry department were all very welcoming and helpful to me; their collaborations and frequent assistance primed me for success in the interdisciplinary field of liquid crystals. I enjoyed a fruitful symbiotic relationship working with Alyssa Scarbrough on the twist-bend project. She synthesized an abundance of twist-bend compounds and candidates for our group and I had the privilege of investigating many of them with her. She has a very broad knowledge of chemistry and I am grateful for her eagerness to help me with my many questions about chemistry. The entire liquid crystal chemistry group, including Lee Foley, Ed Guzman, Eric Carlson, Dayan Wei, Eva Korblova, and Dave Walba, were all very friendly, welcoming, and willing to help me. For them I am very thankful.

I had the good fortune to be able to complete cutting-edge liquid crystal research at the Advance Light Source in Berkeley, CA, from October 2016 – 2017. Chenhui Zhu informed me of the doctoral fellowship in residence at the ALS and sponsored me while I was there, acting as a surrogate advisor to me. I appreciate his graciousness is guiding me during this time. While I was there, I met Mirek Salamończyk, a post-doctoral researcher working to understanding the twist-bend phase as well. Despite the real possibility of an academic rivalry, Mirek selflessly helped me

familiarize myself with the RSoXS beamline and frequently stayed all night with me on experiments. I had the honor to collaborate with him on a project on the twist-bend, for which I hope we will both benefit. I am very grateful for the support and guidance of the RSoXS beamline scientist Cheng Wang and his post-doctoral researchers Greg Su, Isvar Cordova, and Mike Brady for their friendliness and their help in coordinating beamtime for me. While I lived in the east bay, I was fortunate enough to find a room to rent with Yu-Ping Liu, who was friendly, warm, and enthusiastic in sharing her Taiwanese culture with me.

The liquid crystal group's administration office plays an enormous and sometimes unseen role in the smooth operations of the group, and I appreciate their resolute support of myself and the rest of the Soft Materials Research Center. Christine Morrow has a strong dedication to science outreach and I am glad she managed to encourage me out of my comfort zone to experience whole other facets of science beyond research. Annett Baumgartner, Dakota Nanton, and Lauren Moreno have aided me numerous and uncountable times throughout the years, and I appreciate them for their assistance.

I have made many great friends in the CU physics graduate program; they were my support system outside of classes and research. I remember fondly the days of outdoor climbing with Adam Green, Eric Martin, and Adam Higuera on the weekends as some of the most fun and fulfilling experiences of my graduate career. Adam Keith introduced me to the joys of board games, mountain biking, and trail running, and his abundant energy was frequently contagious. I am grateful to have lived with physics graduate students Adam Green and Will Lewis during the earlier years of my PhD. Our mutual support was pivotal for me as we advanced in our degrees.

I am grateful for all the other liquid crystal and condensed matter colleagues who I had the privilege to meet during scientific conferences and summer schools. I enjoyed immensely studying

alongside Pim van der Asdonk, Uroš Jagodič, Amir Sajadi, Luka Cmok, Paul Ackerman, and other friends in Cambridge, England at the I-CAMP 2013 summer school, and Ngaatendwe Pfukwa, Anne Hélène Gélébart, Kazage Utuje, and other friends in Stellenbosch, South Africa at the I-CAMP 2014 summer school. I enjoyed meeting new friends and sharing experiences about research and our homes.

My partner Moné Miller has perhaps done the most to support me through my graduate career. Her unconditional encouragement of me in my endeavors helped lift me when school and research became demanding. Intellectually, she has broadened my perspective of the world and I always appreciate and enjoy our discussions. Her adventurousness and ability to appreciate all aspects of life is inspiring.

Finally, it is only through the endless support of my family that I am where I am today. For that, I am eternally grateful. I have my father to thank for my appreciation of many aspects of the journey of life, including food, plants and nature, and cultural customs and experiences; he nurtured my inquisitiveness about the world throughout my life. I am thankful for my mother's constant and selfless support, her desire for my well-being, and her encouragement for me to enjoy my life. I am grateful for my friendships with my sister Jen and my brother Adam and look forward to continuing to learn from them and grow with them. I love my extended family, who put their care in me and each other before all else.

Many thanks to the countless others who I did not mention specifically but who supported and believed in me throughout my graduate career. I am very fortunate for what I have.

Acknowledgements

Here, I acknowledge my colleagues for their direct contributions and involvement in much of the following research, and without whom my body of work would not have achieved such richness and depth.

From the Department of Physics and the Soft Materials Research Center at the University of Colorado Boulder, I recognize the following colleagues in alphabetical order by last name: Dong Chen, Noel A. Clark, Matthew A. Glaser, Keri A. Graber, Arthur Klittnick, Joseph E. Maclennan, Leo Radzihovsky, Min Shuai, and Joseph Yelk.

From the Department of Chemistry and Biochemistry and the Soft Materials Research Center at the University of Colorado Boulder, I recognize the following colleagues in alphabetical order by last name: Lee Foley, Eva Korblova, Mark Moran, Jan H. Porada, Jessica Riano, Alyssa N. Scarbrough, and David M. Walba.

From the Advanced Light Source at the Lawrence Berkeley National Laboratory, I recognize the following colleagues in alphabetical order by last name: Alexander Hexemer, Victoria A. Norman, Mirosław Salamończyk, Cheng Wang, and Chenhui Zhu.

From the Laboratório de Química Computacional, Instituto de Química, Universidade de Brasilia, I recognize Edgardo Garcia.

From Kent State University, I recognize the following colleagues in alphabetical order by last name: Antal Jákli, Mirosław Salamończyk, and Samuel Sprunt.

From the University of Aberdeen, I recognize the following colleagues in alphabetical order by last name: Ewan Forsyth, Corrie T. Imrie, Daniel A. Paterson, and John M. D. Storey.

I appreciate the meticulous editing of this thesis by Joseph E. Maclennan and Adam A. S. Green. Their extensive efforts improved the readability and content of this thesis by orders of magnitude.

Finally, I am grateful for my funding sources over the years. My work was supported by the Soft Materials Research Center under NSF MRSEC Grants DMR-0820579 and DMR-1420736, and United States Education Department GAANN Award P200A120014, with partial support from the ALS Doctoral Fellowship in Residence Program from October 2016 – 2017. In addition, a portion of my research used resources from the Advanced Light Source, which is a DOE Office of Science User Facility under contract no. DE-AC02-05CH11231.

Contents

FIGURES

Figure

1. INTRODUCTION

This thesis encompasses my body of work on the twist-bend liquid crystal phase, perhaps the most novel and exciting new discovery in the field since the advent of the bent-core liquid crystals in the 1990's. To understand why the twist-bend phase is so exciting, one must first understand its context in the broader field of liquid crystals through some of their unique phase assemblies.

Liquid crystals (LCs) are soft condensed materials which form thermodynamic phases with degrees of ordering and organization between those of an isotropic liquid and a crystalline solid. Their susceptibility to external factors like temperature, pressure, electric and magnetic fields, and surfaces makes them "soft", while their high density of interacting objects makes them a "condensed material". Liquid crystals are constituted of anisotropic objects, whose reduced symmetry promotes unique self-organization. In my work, the LCs are made up of small organic molecules, with the most common molecular geometries being cylindrical, disc, and bent rods. While their shape anisotropy promotes self-assembly at moderate temperatures (200 – 15°C), their flexible chemical groups tend to suppress the formation of a solid crystal. LCs can be made up of a broad range of materials in addition to small organic molecules, such as polymers [1,2], DNA [3–5], nanoparticles [6–8], colloids [9,10], or any other material with shape anisotropy or anisotropic interactions. Here, I will only consider LC materials that are made up of small organic molecules without an accompanying solvent ("thermotropic" LCs). LCs may in principle have any combination of orientational and positional ordering of the molecules between those of an isotropic liquid and a crystalline solid. In the following sections, I will describe the kinds of LC phases and ordering which are most relevant to my research.

1.1. NEMATIC LIQUID CRYSTALS

LCs that form the nematic phase ("nematic LCs", or "nematics") are the workhorse of the LC and soft matter communities. The nematics are a class of phases in which the constituent molecules have only short-ranged positional ordering in 3D space but have long-ranged orientational ordering of the molecules along a given direction. The local direction of ordering is called the "director", while the entire sample can be described by a "director field". The nematics make up the overwhelming majority of technological applications of LCs, as they tend to be the most fluid and robust of the LC phases. The industrial applications of nematic LCs have primarily been focused around the display industry, though today nematics are finding many new uses in such applications as nano-templating [11], artificial muscles [12], and LC elastomer actuators [6,13]. The nematic phases are classified according to the nature of their orientational ordering; though all have long-range orientational organization, their ordering may be uniform along a single direction, helical, or even more complex.

1.1.1. The nematic phase

The conventional nematic phase (most commonly referred to as the "nematic phase"), consists of a fluid of anisotropic molecules which have an uniform average orientation along a single direction, but with the molecules having only short-ranged order in three dimensions, as in a conventional isotropic liquid (Figure 1.1.1) [14–17]. Nematics can be formed through excluded volume interactions by any cylindrically-symmetric object whose aspect ratio (length/width) and volume fraction exceed a certain amount, as given by the Onsager criterion [18]. Nematic LCs are most commonly composed of "rod-shaped" molecules that exhibit an effective cylindrical symmetry when the fast molecular rotations about their long axis are averaged (Figure 1.1.1).

What makes nematics so advantageous for display applications is their birefringence. Birefringence is the phenomenon where the speed at which light travels through a material and the phase it picks up are dependent on the direction of the polarization of the incident light. By measuring the difference in phase between two orthogonally polarized rays of light, we measure the birefringence. The conventional nematic phase is uniaxial – there is one direction of light propagation through the sample in which there is no differential retardation of the two orthogonal polarizations of light; along this axis, there will be no measurable birefringence. Birefringence in a nematic LC sample originates from its degree of orientational order.

Their lack of long-ranged spatial correlation lends nematics their fluidity, with viscosities on the order of 0.1 Pa·s [14], comparable to that of olive oil. The orientational fluctuations in nematics cause them to scatter light, giving them a characteristic milky white color. In a polarized light microscope (PLM) (section 2.1), the long-ranged molecular ordering and defect structure in the nematic sample manifest as the characteristic "Schlieren" texture: dark threads and Maltese

crosses which are line and point defects, respectively. A beneficial feature of nematics is that they can be easily biased to align along a given direction via a significant number of methods, the most commonly employed of which are: application of electric and magnetic fields, mechanical shearing, unidirectional flow, and by surface alignment – confinement by boundaries which have a local preference for a particular orientation. In an LC research laboratory, as well as in the display industry, surface alignment of a nematic is accomplished by confining the LC between two substrates, with the inner surfaces treated with a thin film which is generally mechanically rubbed in a particular direction to yield a directional preference of alignment along the rubbing direction, or "unidirectional planar" anchoring. Alignment of the nematic (or any LC phase) normal to the plane of the cell is called "homeotropic" anchoring.

As the conventional nematic phase has the most symmetric organization of the nematics, it is also the most well understood. The combination of macroscopic molecular orientation, fluidity, and susceptibility to external fields and stimuli make the uniaxial nematic the most widely utilized LC phase. Not only is it used in the LCD industry, but a new crop of researchers are using nematics for their own research and in novel applications, for instance as templating media for aligning fibrous or polymeric materials [11] and nanoparticles [19], magnetic field-controlled ferromagnetic nanoparticles [20], thermal- [21] and light-activated [22,23] LC elastomers, along with biological [24] and gas [25] sensors, to reference just a few. The uses for the LC nematic phase are myriad and widespread, and in the future, they will likely continue to be the most fruitful of the LC phases.

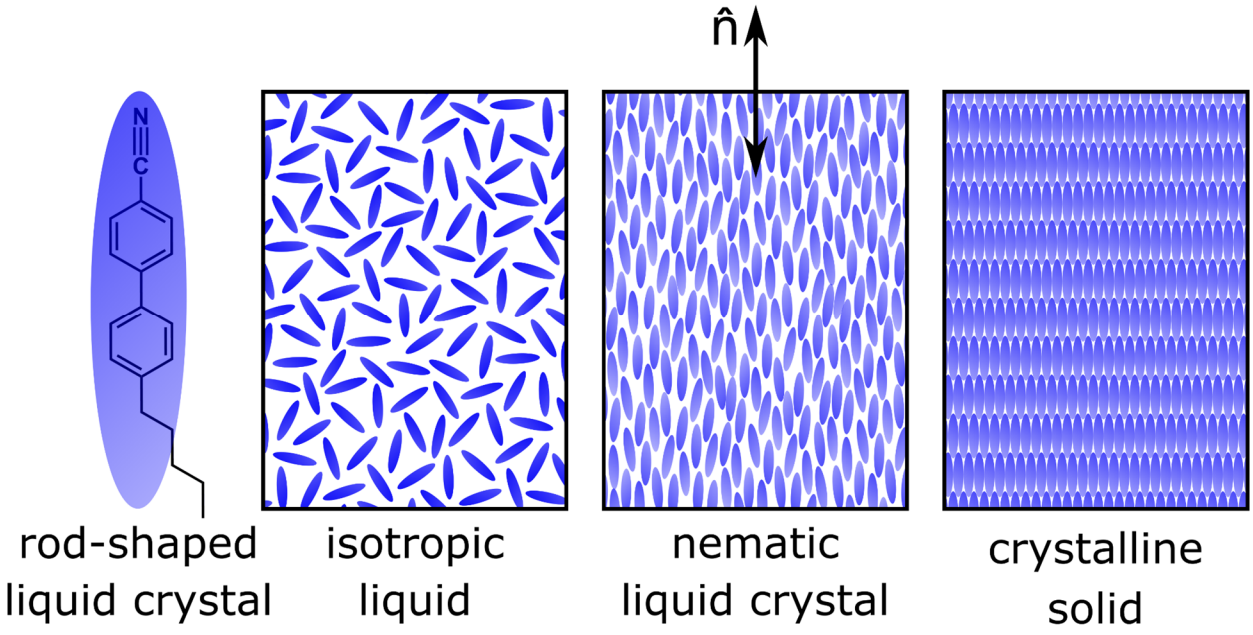

Figure 1.1.1: Introduction to liquid crystals and the nematic LC phase.
Liquid crystals are generally composed of small organic molecules with particular geometric shapes. The 5CB molecule is, on average, shaped like a long rod or an ellipsoid. LCs form an isotropic liquid phase, in which molecules have short-ranged positional order in the three spatial dimensions and are orientationally disordered, and a crystalline solid, in which the molecules are spatially and orientationally ordered in three dimensions. In addition, LC molecules have condensed phases of matter that are informed by their particular geometric symmetries. In the nematic phase, the molecules have short-ranged positional ordering in the three spatial dimensions, but they are orientationally ordered on average along a single given direction, called the director n̂. The director is a double-headed vector because molecules have an equal probability of orienting a particular end upward or downward – i.e., the nematic has head-tail symmetry along the director.

1.1.2. The cholesteric phase

When an LC material is chiral, it has a significant impact on the physical properties of its resulting LC phases. Chirality is the property that an object, molecule, or sample is not superimposable on its mirror image by a simple combination of translation and rotation [26]. Chirality can manifest in all kinds of physical systems at virtually all length-scales, from elementary particles whose quantum spin vectors are either parallel or antiparallel with their velocity vectors, molecules which lack mirror symmetry, all the way to astronomical phenomena like the spiraling of galaxies.

One might initially expect that nature would generally not distinguish between left- and right-handed objects. After all, why should it matter that a snail shell grows with a left-handed winding over a right-handed winding? Or that viney plants wind up a tree branch in a left-handed or a right-handed helical way? In fact, most natural systems do exhibit a differential treatment of left- and right-handedness: distinct species of snails wind their shells with one handedness over the other, and viney plants have either a left- or right-handed preference for how they wind around an object. Although there is debate as to why nature favors a given chirality over another in a particular situation, we know that it does. Our bodies' differential interaction with medicines of left- and right-handed chirality provides the impetus for the pharmaceutical industry to invest enormous amounts of resources into developing effective means for the chiral synthesis of chemicals and drugs [27].

When a molecule contains a single chemical group that causes its structure to not be superimposable on its mirror image, that molecule is chiral, with either a left- or right-handedness. These molecules have their chirality 'built-in' to their chemical structure. If a chiral molecule

forms LC phases, the chirality generally transfers to the structure of the resulting LC phases. For example, when a chemist takes an LC molecule which forms the nematic phase and adds a chemical group to the molecule that makes it chiral, it can cause the material to form a chiral nematic phase [26,28]. One can also create a chiral nematic by adding a small amount of a chiral material to an achiral (not chiral) nematic LC. The simplest chiral version of the nematic phase is called the "cholesteric" phase, so named because it was first observed in cholesteryl benzoate derived from carrots [29,30].

The cholesteric phase consists of molecules ordered locally as in the conventional (achiral) nematic phase, but with a continuous twist perpendicular to the local director (Figure 1.1.2). This helical twist gives rise to a *structural* chirality in the cholesteric phase, manifesting as a helical periodic structure with a pitch on the order of hundreds to many thousands of nanometers. The cholesteric helical superstructure contributes to its particular optical properties – like optical rotation and selective reflection – in which the phase treats left- and right-handed circularly polarized light in disparate ways [15].

The cholesteric phase has historically also been referred to as the "chiral nematic" phase in the literature. However, the existence of several distinct nematic phases (the cholesteric phase, the nematic blue phases, and the twist-bend nematic phase), in which chirality is essential to the structure of the phase, makes this denomination potentially confusing. We therefore refer to the specific form of ordering described in Figure 1.1.2 specifically as the "cholesteric" phase.

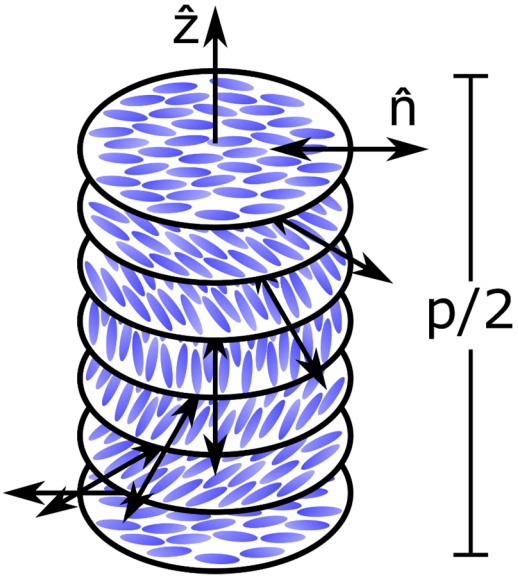

Figure 1.1.2: Schematic of the cholesteric phase.
The cholesteric phase is a simple chiral variant of the conventional nematic phase, in which the molecules are locally oriented along the director $\hat{n}$, but the molecules smoothly twist perpendicular to the nematic director (along $\hat{z}$). This schematic is depicted with different circular planes which rotate by a large amount with respect to the next plane, but in reality, molecules smoothly and continuously rotate in orientation along $\hat{z}$.

1.1.3. Other nematic phases

There are three other distinct kinds of nematic LC phases: the nematic blue phases, the biaxial nematic, and the twist-bend nematic phase.

The nematic blue phases [26,31–36] are nematics in which a strong preference for chirality leads to director twist, as in the cholesteric phase. However, in the nematic blue phases the molecules twist in two orthogonal directions, forming "double-twist cylinders" which pack into one of a number of possible 3D cubic lattices at the energetic expense of an accompanying lattice of disclinations, or line defects [33]. These phases were dubbed "blue phases" because, on initial investigation, they appeared blue both inside and outside of the polarized light microscope [37]. The color of the blue phase arises from the selective reflection of light from the 3D lattice of double-twist cylinders, and it is not necessarily blue. The selective reflection and subsequently observed colors are dependent on the particular lattice, lattice spacing, and the orientation of the lattice with respect to the incident light. Therefore, the blue phases can exhibit any colors in the visible and surrounding parts of the electromagnetic spectrum. Though the blue phase may have been the first LC phase observed [29,30] (along with the cholesteric phase), the nature of the various flavors of the blue phase was not well understood until the 1980s and 90s because the its temperature range tends to be <1°C, making detailed study practically difficult. Eventually, polarized light microscopy studies of blue phases and their crystallites [38], optical Bragg scattering experiments [39–42], and electron microscopy experiments [43,44] help to definitively determined the nanoscale structure of the nematic blue phases.

A much rarer nematic phase is the biaxial nematic [45,46]. The biaxial nematic is a nematic in which the molecules order orientationally both along their long axis and along their other two

lateral axes. One would expect this phase to be observable in the nematic phases of brick-shaped or bent-shaped LC molecules. Although a number of researchers have reported observations of a biaxial nematic phase, many others have raised questions about the veracity of these identifications. The first widely accepted identification of a biaxial nematic occurred in 1980 in lyotropic LC systems (LCs in a solvent) [47]. Their relative lack of representation in thermotropic LCs remains a mystery.

The twist-bend (nematic) phase is the most recently discovered nematic phase, having been definitively identified in 2011 [48]. In this thesis, we will discuss the origins of the twist-bend phase and the experiments that helped reveal its nanoscale structure. To fully understand the twist-bend nematic phase and situate it in the broader context of the LC field, we continue our introductory discussion with the LC smectic phases and the bent-core phases.

1.2. THE SMECTIC PHASES

Another common kind of LC phases are the smectic phases. The smectic phases have orientational ordering of the long axis of the molecules, as in the nematic phase, with a lamellar (positional) ordering in one spatial dimension, while remaining a fluid in the other two dimensions. For this reason, one can think of the smectic phase as a 1D crystal and as a 2D fluid (Figure 1.2.1).

There are many different kinds of LC smectic phases. The smectic phase in which the molecules have their director oriented along the direction of layering is called the smectic A phase, and the phase in which the director tilts away from the direction of layering is called the smectic C phase (Figure 1.2.1). When the molecules develop extended short-ranged ordering in the plane of the layers, they are called higher-order smectic phases. Smectics can exhibit a rich variety of molecular arrangements, including any combination of tilt modulation, short- or long-ranged in-plane ordering on a 2-dimensional lattice, molecular bilayers, or partial molecular intercalation.

The smectic phases make up some of the most familiar natural materials in our daily lives. For example, cell membranes are composed of lipids exhibiting a bilayer smectic phase. Nature has selected the smectic phase as the best candidate for providing an effective boundary for the cell – it is rigid enough to provide structure, yet fluid enough to enable proteins and enzymes to embed themselves, allowing for the selective transport of resources and substances in and out of the cell.

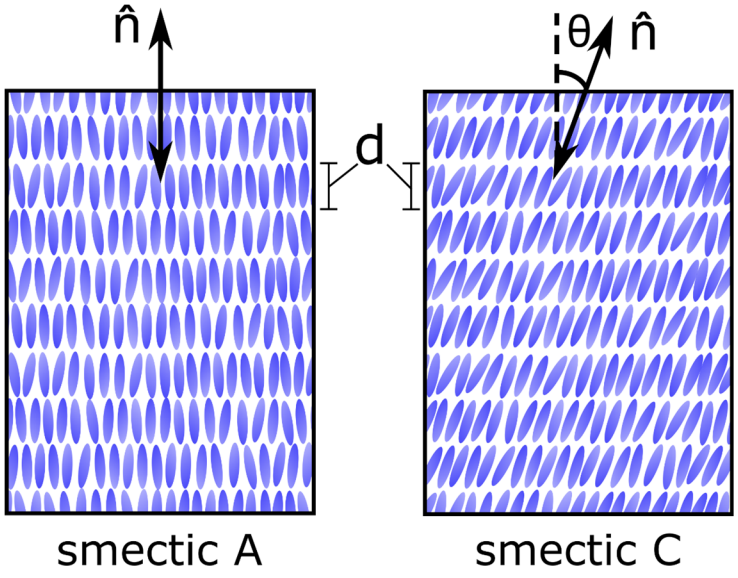

Figure 1.2.1: Schematic of two smectic phases formed of rod-shaped molecules.
The simple smectic phases are composed of molecules which are oriented, and layered in one dimension, but fluid in the other two dimensions. The molecules are organized into layers which are approximately one molecule thick. In the smectic A phase, the director n̂ is along the layer normal direction, while in the smectic C phase, n̂ is inclined from the layer normal direction by the angle θ.

1.3. BENT-CORE LIQUID CRYSTALS

In contrast to the simple rod-shaped LC phases discussed above, the twist-bend nematic phase is composed of bent molecules. The related "bent-core" LCs make up an entire class of LCs which, due to their reduced symmetry, can exhibit more complex phases than those of their rod-shaped relatives [49,50]. Bent-core LC molecules can form nematic and smectic phases just as rod-shaped ones can, but they can also develop additional degrees of ordering along their bend axis. For instance, bent-core LC materials can form the usual smectic A phase, and then transition into a ferroelectric smectic A phase, with the bend in the molecule providing an additional axis about which ordering takes place within the layer (Figure 1.3.1).

Perhaps the most fascinating aspect of bent-core LCs is that they can spontaneously develop structural chirality, even when the molecules themselves are achiral. This can happen when bent-core LCs form tilted smectic phases with polar ordering along their bend axis – the coordinate system defined by the layering normal direction, molecular tilt direction, and polar-ordering direction (which are generally all orthogonal to each other) is left- or right-handed within each layer, making the layers chiral. Therefore, the entire sample can be either homochiral (entirely composed of layers of a single handedness) or racemic (composed of equal amounts of left- and right-handed layers). In the B2 phase of bent-core LCs, there are four combinations of tilted, polar phases: they can be either synclinic (their tilt direction points the same way in neighboring layers) or anticlinic (their tilt direction alternates from layer to layer), and ferroelectric (their polar direction points the same way in neighboring layers) or antiferroelectric (their polar direction alternates from layer to layer) (Figure 1.3.1) [51]. Bent-core LCs form a number of even more exotic phases, including the dark conglomerate sponge phase [52], the helical nanofilament (B4) phase [53], and the polarization modulated B7 phase [54].

The twist-bend phase is another such exotic phase exhibiting complex nanoscale organization driven by spontaneous chiral symmetry breaking. In the following section, I will describe some of the experimental tools we use to investigate and characterize such complex LC phases.

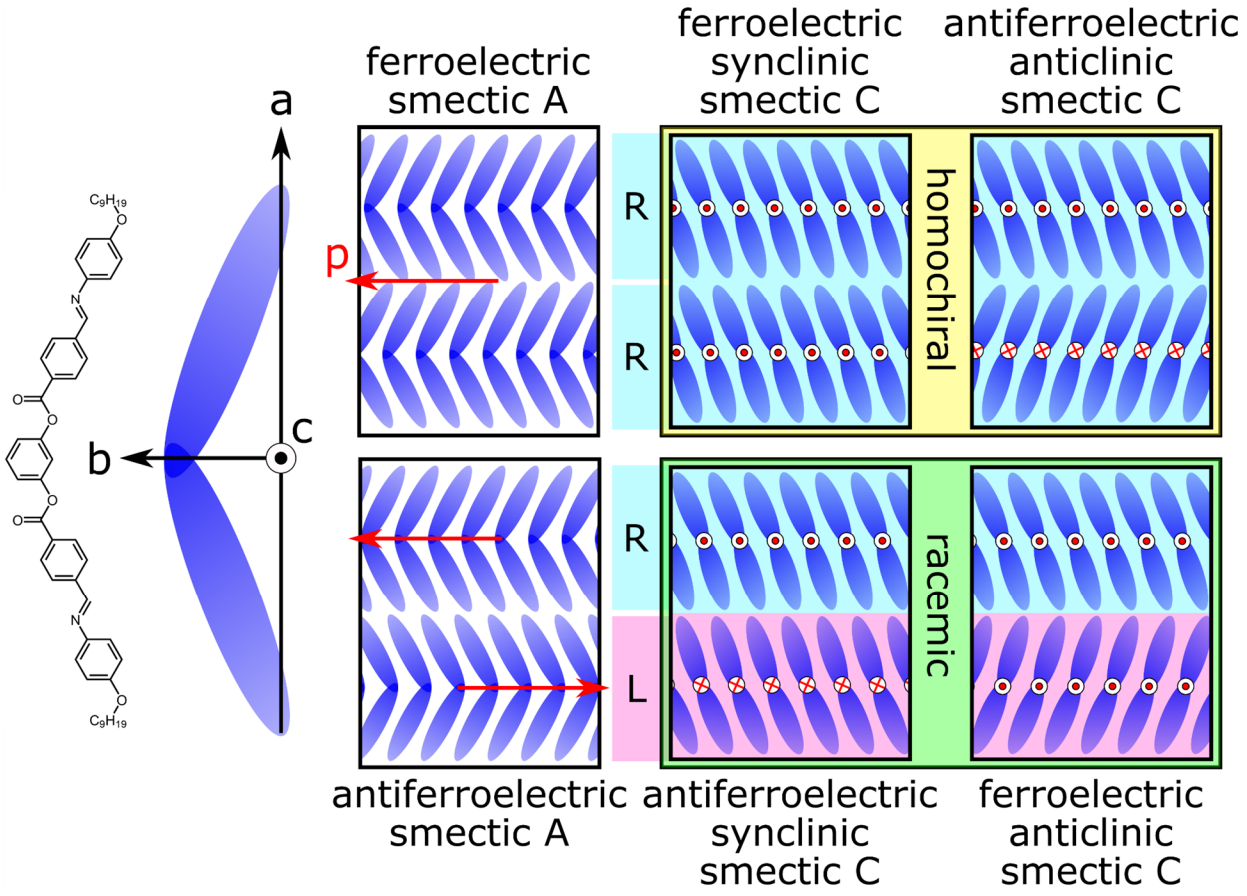

Figure 1.3.1: Introduction to bent-core LCs and selected bent-core LC phases.
Bent-core LCs are composed of small organic molecules with a rigidly fixed bent shape originating from its chemical structure. These molecules can be approximated as bent objects (bananas, bows, boomerangs, etc.) with intrinsic polarity along the direction of the bend, b. When these molecules form condensed phases, they may develop smectic ordering and additional orientational ordering of their bends within the layer. For example, in the ferroelectric smectic A phase, not only do the molecules form layers, but their bends also develop long-ranged in-layer ordering along a single direction. In the antiferroelectric smectic A phase, adjacent layers have their bends in opposite directions. With the introduction of tilt in these phases, the layer normal direction, the tilt direction, and the polarization direction define three coordinate axes which may be either left- or right-handed. This induces the spontaneous onset of chirality, even though the molecules themselves are achiral. Because the layers are chiral, the phase may be composed entirely of layers of a given handedness (homochiral phases), or phases which are globally racemic (composed of an equal amount of left- and right-handed layers). These are only a few of the many bent-core LC phases that have currently been identified.

2. EXPERIMENTAL METHODS

In this section, I introduce the primary experimental approaches we use to investigate the twist-bend phase. Each technique probes certain aspects of the orientational and positional ordering of LC phases, such as macroscopic optical anisotropy, nanoscale structure, and periodic orientation modulations. When taken together, these complementary techniques provide a window into the world of the twist-bend phase.

2.1. POLARIZED LIGHT MICROSCOPY

Polarized light microscopy (PLM) permits the identification of LC phases by the observation of characteristic optical textures and properties exhibited by the organization of the LC molecules. The PLM consists of a common optical microscope [55,56] with two linear optical polarizers in the optical path, generally oriented at 90° with respect to each other, with the LC sample in between them. This configuration makes PLM sensitive to any optical phenomena in the sample that tend to convert a component of the incident polarization along the direction of the second polarizer. In LCs, this most commonly includes optical birefringence and optical rotation. An object with birefringence has indices of refraction which are different for each orthogonal polarization of incident light, yielding elliptically polarized light in general. The elliptically polarized light will may have a component of polarization along the direction of the analyzer, allowing for transmission. This makes the PLM sensitive to average local molecular orientation. Since different LC phases have distinct local ordering, this can yield characteristic optical features, or *textures*, in the PLM which can be used to help identify the phase [15].

Optical rotation arises in samples with chirality, where a chiral structure has a spatially varying dielectric tensor which rotates the plane of polarization. Optical rotation from molecular chirality is generally a very weak effect and difficult to observe in LC cells of typical thickness (several microns). Molecules arranged in a chiral or helical structure, as in the cholesteric phase (Figure 1.1.2), produce considerably stronger optical rotation. By uncrossing the second polarizer with respect to the first in a non-birefringent or optically extinguished domain (the domain being dark under crossed polarizers), one can observe a differential transmission/reflection in the intensity or wavelength of light. This is among the most straightforward methods to determine if an LC sample exhibits structural chirality.

In addition, the nature of the defects in a sample can provide evidence for the possible symmetries or nanoscale organization of the phase. For instance, because the nematic director has head-tail symmetry, nematics can exhibit point defects of order n/2 (defects about which molecules rotate by πn, where n is an integer) and n (defects about which molecules rotate by $2\pi n$), whereas polar phases, due to their lack of reflection symmetry, can only exhibit point defects of order n. The presence of focal conic defects in a cell indicates the presence of a 1D structural periodicity in the phase, as in the smectic phases [57].

In investigating an LC phase under the PLM, one may simply and qualitatively determine the ‘fluidity’ of a phase by creating a glass sandwich cell with LC sample in between and either shearing it or pushing on the top to depress the glass and displace material. When one does this, and the texture continuously deforms, one can be assured that the phase is liquid crystalline. When the texture does not change, and the cell does not shear under moderate application of force, one is likely observing a solid crystalline phase. This technique can be critical in determining whether an unfamiliar phase is liquid crystalline or solid in nature.

To prepare the LC for microscopic observation, one may fill a commercial cell by heating it to the melting temperature of the sample and placing a small amount of sample near the inlet, allowing capillary action to pull the now isotropic sample into the cell. For an initial characterization of a material, one may make a simple sandwich cell by placing a piece of clean glass on a hotplate at the melting temperature, followed by the LC, and then a second piece of clean glass on top. This cell commonly yields mixed anchoring conditions (random planar and homeotropic), which may be sufficient for characterization of well-known phases (conventional nematic, cholesteric, or smectic A phases, for instance). It is best to cool the samples slowly from the isotropic phase to grow large domains with the natural texture of the phase.

2.2. Freeze-fracture transmission electron microscopy

Freeze-fracture transmission electron microscopy (FFTEM) permits the visualization of the nanoscale morphology of LC phases by vitrifying (freezing in) the order of a phase and fracturing the sample to reveal the nanostructured surface. FFTEM is an ideal microscopy technique for investigating LC phases and many other soft materials for two important reasons: These systems are soft and highly sensitive to the preparation and measurement conditions and nanoscale probes which can alter their native state, and these soft systems are generally made of organic materials with low electron densities, yielding very little or no contrast in a direct TEM measurement. In FFTEM, the exposed nanostructure surface is coated by a thin layer of platinum, which is electron dense and scatters electrons efficiently, deposited at 45° to providing contrast in a TEM. Because of the angled deposition, we observe a 'shadow' effect, which provides imaging contrast but does not yield a quantitative measurement of feature height. This is a small sacrifice for the reliability of the FFTEM method over other nanoscale imaging techniques such as AFM and cryo-AFM.

FFTEM can be used to determine the spacing of various structural features or periodic structures. In the bent-core phases, for example, unique structures such as those of helical nanofilaments (Figure 2.2.1a) [53] and the negative gaussian curvature of the smectic layers in the dark conglomerate bent-core phase [52] are clearly visible. In these cases, FFTEM provided the critical evidence for determining the LC structure and ordering.

FFTEM is not a perfect technique, however. FFTEM may fail when the phase of interest is too fluid for the experimenter to reliably vitrify the nanoscale structure of the phase. This can occur in the twist-bend nematic phase and may occur in the other nematic phases of some

particularly fluid LC materials. One may obtain some information from these kinds of samples if they can identify domains with the characteristics of the particular phase and avoid domains without those characteristics (a solid crystal phase, for example). This makes measurement more dubious, and the experimenter may be required to utilize information from other experimental methods to determine the likelihood that their observations are reliable and represent the desired sample.

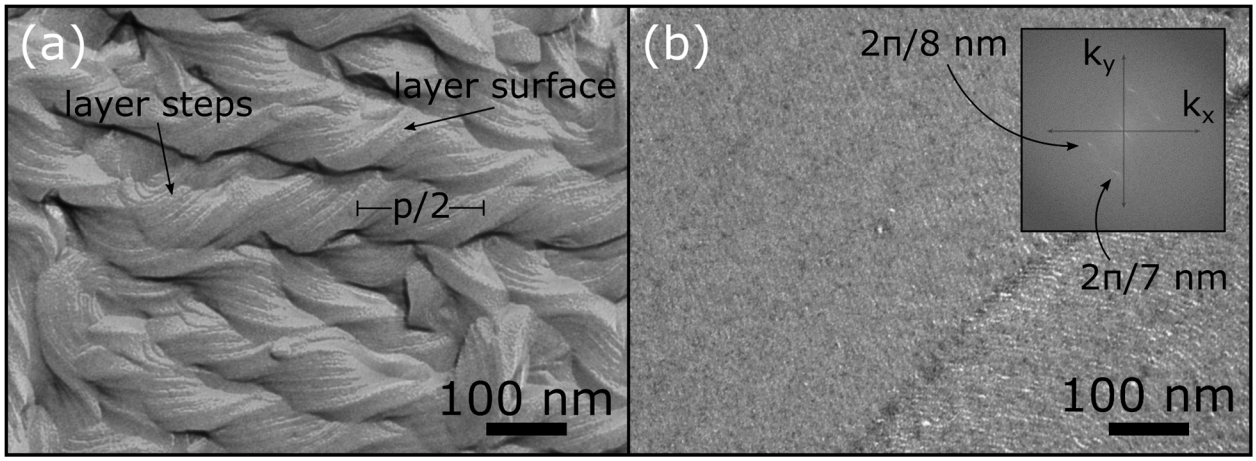

Figure 2.2.1: Examples of systems which benefit from characterization by FFTEM.
(a) The helical nanofilament phase is formed of bent-core molecules in a ferroelectric smectic C phase which also has short-ranged rectangular positional ordering in the layer. A variety of factors and constraints cause the blocks of layers to saddle-splay, yielding twisted blocks of smectic layers forming long filaments, or "helical nanofilaments". FFTEM was instrumental in definitively determining the structure of this phase. (b) FFTEM experiment on the twist-bend LC phase exhibits long-ranged structural modulations along a single direction. A spatial Fourier transform of the image demonstrates a periodicity of 7 and 8 nm in the two domains visible in this particular image.

The rest of this section is written for the experimentalist who wishes to understand our FFTEM procedure in detail: We prepare a sample for FFTEM experiments by sandwiching it between the glass planchettes in its isotropic phase. We then place the cell onto the glass tongue of the custom-made bronze quenching box and place the box in a hot-stage mounted in a PLM. It is best to heat the LC to the isotropic phase to reduce the number of undesirable pinned domain structures and features remaining from the crystal phase. We then approach the desired phase on cooling and permit it to settle for several minutes at the target temperature. After taking an image

of the texture as evidence for the phase, we push the cell into the center of the bronze quenching box to isolate it from the surrounding air. We then remove the entire box from the hot-stage and quickly position the trap door slit of the box over the liquid propane well and push the sample further into the bronze quenching box so that the sample falls out of the trap door and into the liquid propane. We then fill the sample dewar with liquid nitrogen and wait for it to cool and reach liquid nitrogen temperature.

The sample may now be transferred from the liquid propane well to the cleaning area of the sample dewar by carefully lifting the sample out of the liquid propane with tweezers and

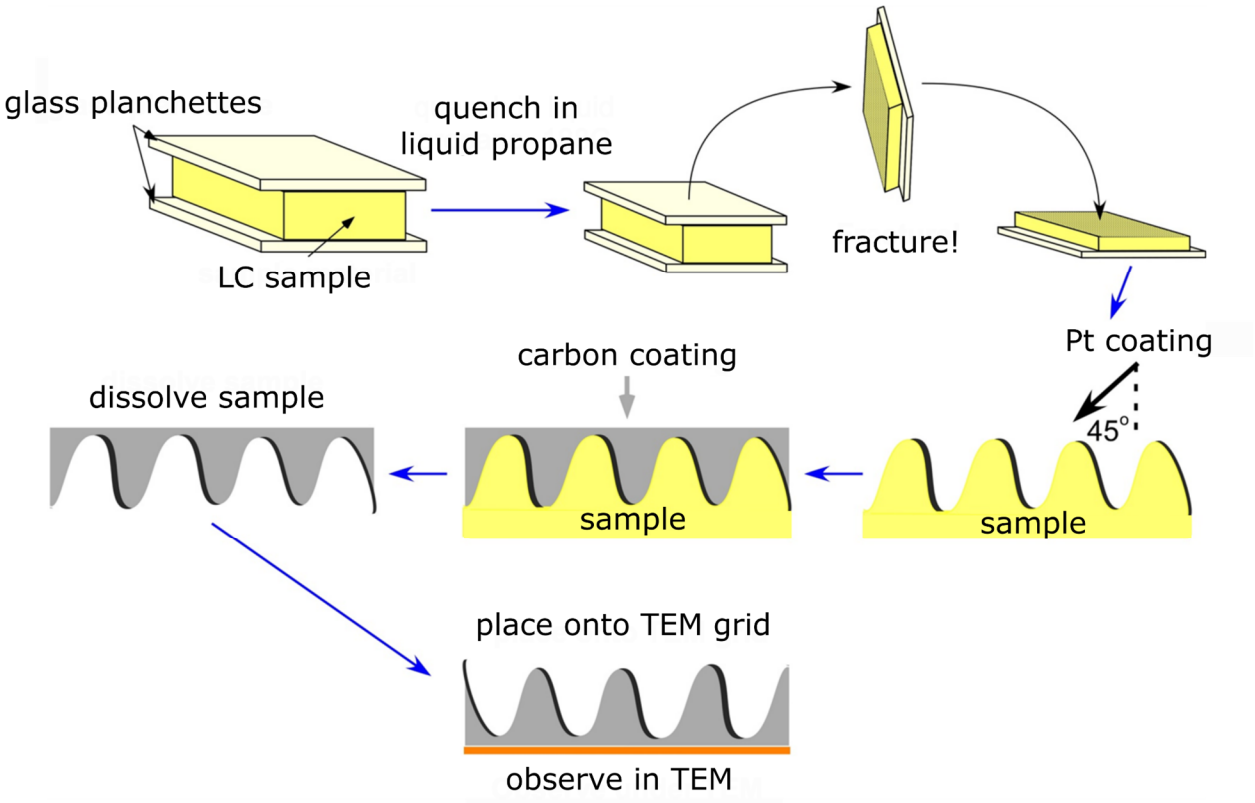

Figure 2.2.2: Schematic of the sample preparation steps in FFTEM.
We sandwich the LC between 2 mm × 3 mm glass slides We rapidly quench the cell to $T < -180°C$ by immersion in liquid propane and transfer it to the freeze-etch machine, where the cell is fractured at $T < -140°C$ under high vacuum. The exposed LC surface is subsequently coated with 2 nm of platinum deposited at 45°, followed by ~25 nm of carbon deposited at 90°. We then remove the LC material on the replica by dissolving in an appropriate solvent. We then collect the Pt–C replica onto a copper TEM grid and image in a TEM, with the platinum providing contrast to the topography of the fracture plane. The surfaces facing the platinum shadowing direction accumulate more platinum and therefore produce darker shadows in the TEM images.

quickly transferring it and propping it up against the raised edge of the cleaning area. You must then permit the liquid propane around the cell to freeze. The frozen liquid propane helps hold the glass cell together as you clean the excess propane from the edges of the planchette cell with a folded filter paper. After cleaning, the cell may slide unimpeded into the cell holder. You may then take the sample dewar to the freeze-etch machine for metal evaporation.

Once the freeze-etch machine is prepped and ready (detailed procedure for prepping and use of the machine is at the machine), you use the sample gun to quickly insert the sample in the vacuum chamber. After the 2nm platinum and 25 nm carbon (for mechanical rigidity) have been evaporated onto the sample, the entire glass planchette (with the LC sample and the replica) is removed from the machine and submerged into a solvent which will readily dissolve the LC. This is usually ethyl acetate, or chloroform if ethyl acetate does not work. This solvent should then be exchanged with a non-reactive solvent that is soluble with the first, such as ethanol, in order to prepare for collection with a FORMVAR-supported TEM grid. Any remaining strong solvents such as chloroform will dissolve the FROMVAR quickly and make the collection of the replicas extremely difficult. Then, use the FORMVAR-supported TEM grid to collect the replica or pieces of replica on the surface. Permit the remaining solvent on the grid to dry so that the replica sticks to the grid. The grid may be used for further collections. These grids may be inserted directly into a TEM for observation.

It is best to record enough TEM images of the sample that the experimenter can be confident that they obtained a representative selection of images. In my experience, this typically amounts to ~30 – 40 images per sample, but less may be satisfactory and more may be necessary depending on the sample, sample preparation, contamination levels, desired accuracy of the quantitative information, variety of interesting structures, etc.

2.3. Resonant soft x-ray scattering

X-ray diffraction techniques are among the most useful for studying the structure of materials on the nanoscale. When positional and orientational ordering in a LC sample are accompanied by electron-density (mass-density) modulation, Bragg scattering becomes a useful probe of the intrinsic order [58]. In a smectic phase for instance, x-ray diffraction can measure such features as the layer spacing, the lateral molecular separation, the associated correlation lengths, and the tilt angle of the molecules. However, there are many ways that molecular organization can occur in LCs and soft materials without an associated electron density modulation. For example, the cholesteric phase (section 1.1.2) is periodic in molecular orientation, but not in electron density. Therefore, conventional x-ray scattering techniques are not sensitive to this helical structure. Other LCs structures which are orientationally modulated and lack an associated electron density modulation include the pitch of the chiral smectic C phase, the helical nanofilament phase [53], the twist-bend phase [59], the twist-grain boundary phase [60,61], and the anticlinic and smectic clock phases [62].

In these cases, conventional x-ray scattering is not enough to probe the LC structure. Fortunately, the resonant soft x-ray scattering (RSoXS) beamline (11.0.1.2) at the Advanced Light Source (ALS) at Lawrence Berkeley National Laboratory is sensitive to these features – the coupling between linearly polarized x-rays and the electron cloud of the molecule yields significant scattering contrast for orientational modulations of the molecules near the K-edge resonance of a particular embedded atom [63]. Hard x-rays (10 keV) can also be used for resonant scattering, but requires a sample which contains an atom with a K-edge resonance in the hard x-ray regime, like phosphorus, or sulfur, for instance [62]. Because LC molecules generally do not include these

heavier atoms in their chemical structure, “hard” resonant x-ray scattering has the significant drawback that it requires the dedicated effort of a new chemical synthesis to create a ‘doped’ molecular LC which may not even exhibit the desired LC phase. For the additional flexibility and ease of use, RSoXS is clearly preferable. The RSoXS technique has been used to investigate such materials as polymer blends [64], block copolymers [65,66], organic bulk heterojunction solar cells [67] and polymeric transistors [68], as well as such LC systems as the half-pitch of the helical nanofilament phase [69] and the helix pitch of the twist-bend phase [70].

To prepare samples for RSoXS, we make sandwich cells consisting of two silicon nitride windows with the sample in between. The silicon nitride windows are 100 nm thick at the “window” to minimize absorption of the incident x-ray beam. The window is supported by a silicon substrate “window frame”, for handling. The SiN window is placed on a hotplate which is held above the isotropic temperature of the material. We then place a minute amount of sample (a few grains) on or near the window and allow it to melt. We then carefully place another window over the first, to create the sandwich cell. The LC layer must be thin ($\leq$1 μm) in order to minimize absorption of the soft x-rays by the sample. These cells may then be loaded onto an x-ray sample stage for RSoXS experiments.

ALS Beamline 11.0.1.2 is optimized for mesoscale studies of soft materials [71]. The beam energy may be tuned from 160 – 1800 eV, permitting the use of the K-edge of the atoms which are most commonly found in organic materials and LCs: C, N, O, F, and others. The apparatus may be used in transmission grazing incidence mode and can perform resonant x-ray diffraction and/or spectroscopy of a sample. The spot size of the incident beam is 100 μm. The experimenter has full control over the incident polarization. The beamline has a hot-stage which can heat up to ~180°C, and a stage which can provide active cooling as well. The sample and detector positions

are controlled from a LabVIEW user module, permitting the user to easily search for signals in the small-angle or wide-angle regimes. We calibrate each combination of motor positions by taking an image of a calibration sample (typically a block copolymer sample with known reflections in the ~10 nm range). 2D detector images are saved as FITS files with the beamline parameters written into the file header as metadata. The data may then be calibrated and processed in the Igor software package using the Nika x-ray scattering data reduction plug-in [72,73].

We typically attempt to obtain a scattering signal with the beamline energy at or near the E_{res} = 284 eV, near the carbon K-edge resonance. Once we find a signal, we must confirm that the signal is indeed resonant in nature. We do this by taking an energy scan about E_{res} (generally 270 eV < E < 290 eV). We run a script with the desired values for the scan in the LabVIEW program with larger steps in energy farther from the carbon K-edge resonance (~1 eV increments, E < 280 eV and E > 287 eV), and smaller steps in energy near the resonance (~0.1 eV, 280 eV < E < 287 eV). This ensures we capture the fine structure of the material, and that we can select either the most intense scattering feature, or the one which corresponds to the desired electron orbital.

We then may scan the temperature as desired. We found that in most cases, the temperature reading of the thermocouple affixed to the hot-stage (inside the vacuum chamber) did not correspond exactly to the transition temperatures of the LC material as obtained from separate and very reliable methods such as differential scanning calorimetry or PLM. This may be for any number of reasons, including: (1) poor thermal contact between the stage and the sample, (2) poor conduction of heat through the sample, (3) thermal gradients in the stage from contact of the hot-stage with the sample holder mounting, (4) temperature scans which do not permit the entire stage to reach equilibrium, among other possibilities. The phase transition temperatures are now usually close enough to that expected from other measurements, though sometimes we need to tweak the

temperature range as obtained from RSoXS to one obtained from a more reliable differential scanning calorimetry measurement if necessary and possible.

3. THE TWIST-BEND NEMATIC PHASE

3.1. INITIAL DESCRIPTION OF THE TWIST-BEND PHASE

The nematic phases were the first class of LCs observed [29,30], and have since proven to be the most applicable and ubiquitous in technology today. For this reason, the identification and characterization of a novel nematic LC phase such as the twist-bend (TB) nematic phase was a significant event in the LC community.

Robert Meyer was the first to consider a hypothetical LC nematic ground state with a defect-free director twist-bend and splay-bend elasticity [74]. In particular, the TB nematic he described is characterized by molecules twisting about an axis and inclined by an angle with respect to that axis. He defined the form of the TB director field $\hat{n}$, written as $\hat{n}(z) = (\sin\theta(z)\cos\varphi(z), \sin\theta(z)\sin\varphi(z), \cos\theta(z))$, where θ is the tilt angle and φ is the azimuthal angle of helical precession, given by $\varphi(z) = qz = (2\pi/p)z$, where p is the pitch of the helix and q the modulus of the corresponding wavevector. Meyer derived these properties from the Frank elastic free energy of the conventional nematic but did not consider the it further since it was purely hypothetical at the time. Meyer's observation is buried in the pages of an LC summer school mini-course; LC researchers did not seriously consider these kinds of phases until the early 2000s [59].

In 2001, Ivan Dozov publish a paper in which he considered the possibility of a nematic ground state in which finite twist-bend and splay-bend coupling would spontaneously arise in a nematic with a negative bend elasticity [75]. The tendency to have a bend elastic constant which becomes negative at a certain temperature would originate from the bent shape of the molecule and cause a spontaneous symmetry breaking of chirality and polarity when the LCs begin to "feel"

each other's bends (when the average excluded volume of a molecule is smaller than that formed by the dimensions of the molecule, like in bent-core LCs). Dozov considered a Frank free energy with higher order terms in the nematic director deformations to obtain the energetically stable defect-free twist-bend and splay-bend phases (Figure 3.1.1).

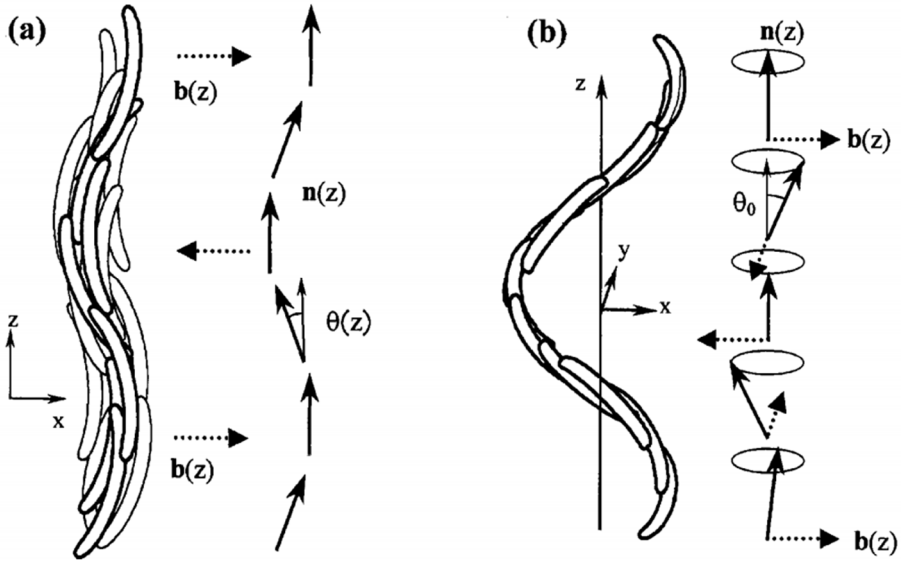

Figure 3.1.1: Sketch of the theoretical (a) splay-bend and (b) twist-bend nematic phases as proposed by Dozov in ref. [75].
(a) The splay-bend phase is a nematic that is sinusoidally modulated in the xz plane, with the local director deviating from the z axis by an angle $\theta(z)$. The splay is maximal at $\theta(z) = \theta_{max}$, and the bend is maximal at $\theta(z) = 0$. (b) The twist-bend phase is a nematic with a uniform director twist and bend throughout, with the molecules precessing about the helix axis with a uniform tilt θ_0. Reprinted from ref. [75].

The splay-bend nematic phase he described has a director in which the local bend oscillates in a single plane continuously from $\mathbf{b}_{max}$ to $-\mathbf{b}_{max}$ along the splay-bend direction z (the xz plane in Figure 3.1.1). This constitutes a modulated nematic phase with no defects and moderate free energy cost, permitting it to spontaneously form under certain conditions in principle. Note that this phase has an associated sinusoidal modulation in mass density along the z axis because of the modulating director bend and splay, giving it the same director field description and order parameter as a conventional smectic phase [70], making a distinction between the two phases somewhat uncertain.

The twist-bend nematic phase described by Dozov has the local director rotating along the helix direction z with the molecules inclined from z by an angle θ (Figure 3.1.1). This yields a phase with constant bend and twist deformation, generating strictly no mass density modulation. The twist-bend nematic phase is two-fold degenerate in twist sense, leading to left- and right-handed possibilities. Dozov estimated that the twist-bend nematic phase should have a pitch of several hundreds of nanometers, making it accessible to experimental observation with conventional LC characterization techniques such as PLM.

Only a year later, Reiner Memmer published a Monte Carlo simulation of a collection of achiral, bent, hard objects (Figure 3.1.2) [76]. He uncovered a number of LC phases, including the conventional nematic and twist-bend nematic phases. The heliconical nematic he identified had essentially all of the features of Dozov's twist-bend nematic phase, with the simulated bent objects spontaneously forming chiral domains with objects precessing about a helix axis and tilted with respect to the axis. Though this supported Dozov's twist-bend nematic

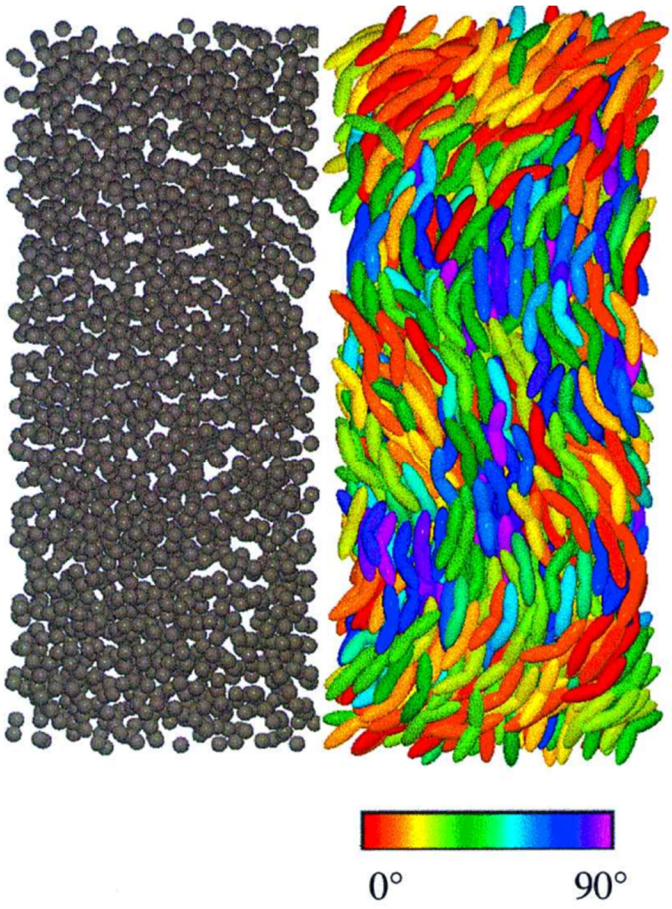

Figure 3.1.2: Simulation of achiral, rigid, bent objects (*right*) and their centers of mass (*left*), performed by Memmer in ref. [76].
The centers of mass are disordered in space, while the rigid, bent objects appear locally nematic with a collective twist of the objects along the vertical direction. The orientation of the molecules is indicated by their respective color-coding. Memmer associated this simulated phase to the twist-bend nematic phase of Dozov [75]. Reprinted from ref. [76].

model, it would take ten more years before the TB phase would be identified experimentally in an LC sample.

The TB phase was first realized in experiment in CB7CB, a cyanobiphenyl twin LC first extensively studied by Barnes *et al.* [77], though they believed it was likely a smectic phase at the time. CB7CB consists of two cyanobiphenyl chemical groups linked together by a 7-carbon alkyl chain (Figure 3.1.3). The odd-number of alkyl groups in the linker causes the minimum-energy configuration of CB7CB to be bent. In 2010, Panov *et al*. investigated CB7CB and several other materials that exhibited a nematic – nematic transition, with their study inspiring the LC community to investigate the unknown lower-temperature nematic phase [78]. Shortly thereafter, Cestari *et al*. used a considerable number of experimental techniques to characterize this unique nematic phase [48], feeling confident enough to identify it as the twist-bend nematic phase of Dozov [75]. Since then, LC groups have primarily been interested in characterizing the detailed structure of this new phase and synthesizing new compounds that exhibit the phase.

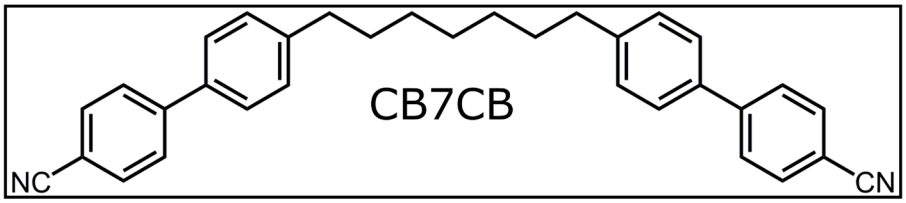

Figure 3.1.3: Chemical structure of the twist-bend nematic LC CB7CB.

A note on terminology: When the anomalous nematic – nematic phase transition was first reported experimentally by Panov *et al*. [78], they were careful not to assign any specific character to the unknown nematic phase, referring to it as the "N_x" phase as x-ray diffraction experiments indicated that the phase remained nematic across the phase transition. Cestari *et al*. was the first group to boldly describe the phase as the "twist-bend nematic" phase (with the abbreviation "N_{TB}") [48] of Dozov [75], as they believed they had demonstrated this beyond a reasonable doubt. Although the apparent majority of groups in the LC community found their study convincing and

began to use N_{TB} to refer to the phase, a number of more cautious groups continued (and continue) to use "N_x" [79–83]. Some researchers believe the community should not use the term twist-bend nematic or "N_{TB}" to describe the experimentally observe twist-bend nematic phase, as it has a number of distinctions from the specific conical twist-bend phase described by Dozov [75]. Dozov's twist-bend nematic phase requires a continuous decrease in the bend elastic energy through zero, an unlikely propsect [84]. Additionally, he estimated the phase should have a helix pitch of ~300 nm, whereas we now know it is generally ~10 nm [59,70,85]. Chen *et al*. decided to refer to the phase as the "heliconical twist-bend nematic" phase, or the "heliconical (HN)" phase, as the term 'heliconical' described the symmetry of the nanoscale structure as we knew it from experiment, and did not necessarily imply that the TB structure was derived from elastic considerations [59]. Despite the unknown mechanisms of the formation of the twist-bend phase, the phase has uniform twist and bend, and the heliconical structure is the only defect-free nematic structure that can fill space with only twist and bend [86]. Therefore, the Boulder group decided to refer to the experimentally observed phase as the "twist-bend (TB)" phase, distinguishing it from the nomenclature of the twist-bend nematic (N_{TB}) phase, which was associated with Dozov's theoretical work [75], and permitting one to refer to the phase based on solely the experimental properties that have been determined so far.

Therefore, in the following text, I use the terminology "twist-bend (TB) phase" to refer to the lower temperature LC phase of CB7CB and all other phases of the same nature, some of which may have been denominated as "N_x" or "N_{TB}" phase in the literature. Because of the newness of the phase, the community is still solidifying its terminology of the phase, and it may yet still change.

3.2. Characterization of the TB phase

3.2.1. Polarized light microscopy textures

Under polarized light microscopy (PLM), the TB phase appears very much like a peculiar smectic phase, which surely had a hand in obfuscating its unique nature until recently. Barnes *et al*. originally synthesized and studied CB7CB in the context of the odd-even effect [77]. They performed a basic characterization of the phases of CB7CB and noted a conventional nematic phase that transitions on cooling into an unknown smectic phase, identifying the final phase on the basis on its "focal conic-like texture and weak transition from the nematic phase". Unfortunately, they did not have the opportunity to perform an investigation of their smectic-like phase with x-ray diffraction at the time. Only in 2010 did Panov *et al.* again study this material and complete a more thorough characterization [78]. When they carried out PLM on cells, they noted a number of textural changes across the phase transition from the N – "N_x" phase, including a coarsening of the typical nematic Schlieren textures, a freezing out of the nematic thermal fluctuations, and the onset of a unique "stripe" texture in aligned cells with a period of twice the cell gap. In a unidirectionally rubbed LC cell, the texture became very different from a smectic (Figure 3.2.1), bringing Panov *et al.* to further investigate it as a novel LC phase.

Since then, some groups have attempted to study the TB textures and investigate their microscopic origin, but few have made concrete advances in understanding them. The most notable study in this vein is that of Challa *et al*. [87], in which they apply strong magnetic fields to the TB phase to align it. On application of a strong field, they found that the striped texture of the TB phase changed into a texture of uniform birefringence, as in a well-aligned nematic phase. When they removed the field, the texture remained. This implies that the striped texture is not an inherent

texture of the phase. They postulated that a mechanical stress induced by a temperature-dependent pitch causes a Helfrich-Hurault buckling instability [88,89], leading to the stripes. This provided an inkling that the TB pitch may vary significantly with temperature, inducing the striped texture which has so vexed LC scientists, even until today.

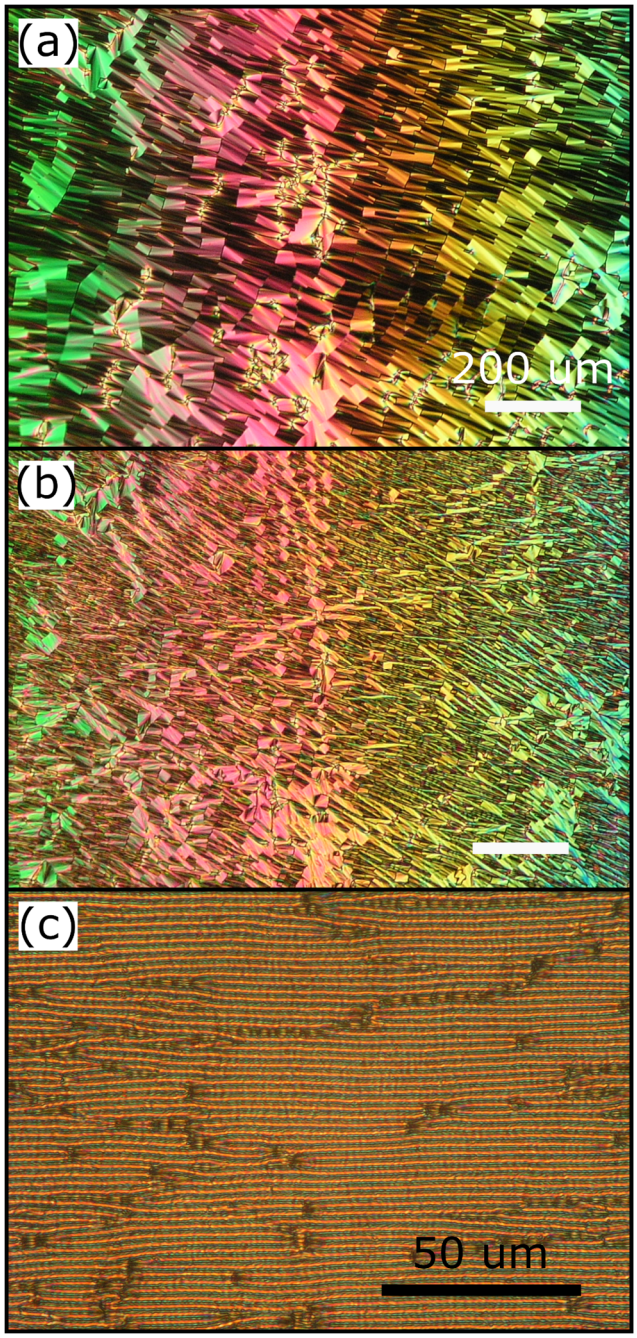

Figure 3.2.1: Characteristic textures of the TB phase.
(a) The "blocky" texture in a cell with nearly unidirectional planar anchoring. This texture is typically the first one observed on cooling from the nematic phase to the TB phase and may easily be confused with the "fan-like" texture of a SmA phase. This texture can generally be observed under all planar alignment conditions. (b) The "striped", "rope-like", or "herringbone" texture in a cell with weak unidirectional planar anchoring. These textures form on further cooling the TB phase from the blocky texture shown in (a). The blocks dissolve into elongated stripe or rope shapes, and the space between is filled with many small focal conic defects. (c) The "striped", "rope-like", or "herringbone" texture formed in a cell with unidirectional planar rubbing in the horizontal direction enforcing uniform alignment at the boundaries. This texture is perhaps the most characteristic of the TB textures. The stripes orient along the rubbing direction, and they exhibit fine periodic features along the stripes, which is the origin of their designation as "rope-like" or "herringbone".

3.2.2. X-ray diffraction: evidence of nematic order in the TB phase

Panov *et al*. performed the first x-ray diffraction experiments in the literature on the TB phase of CB7CB (Figure 3.2.2) [78]. They found that the x-ray scattering arcs exhibited no peak sharpening associated with lamellar ordering through the conventional nematic (uniaxial nematic, "Nu") to TB ("Nx" in Figure 3.2.2) phase transition, controverting the possibility that the Nx phase was a smectic phase, and establishing its nematic nature. They did observe an azimuthal spreading of the peaks in the 2D detector image, indicating that the nematic director either disordered or reorganized such that the molecules tilt away from the original nematic alignment direction. The characteristic PLM textures and nematic-like x-ray scattering in the unknown nematic phase together have since became the de facto diagnostic tool to identify the TB phase and is generally regarded as sufficient evidence to claim the observation of a TB phase in most cases.

For all the dimer LCs that form the TB phase, the x-ray diffraction peak at small angle indicates that the molecules are generally intercalated over nearly half their molecular length in both the nematic and TB phases [48,84,90–97]. This fact will be important in constructing a complete model of the TB phase.

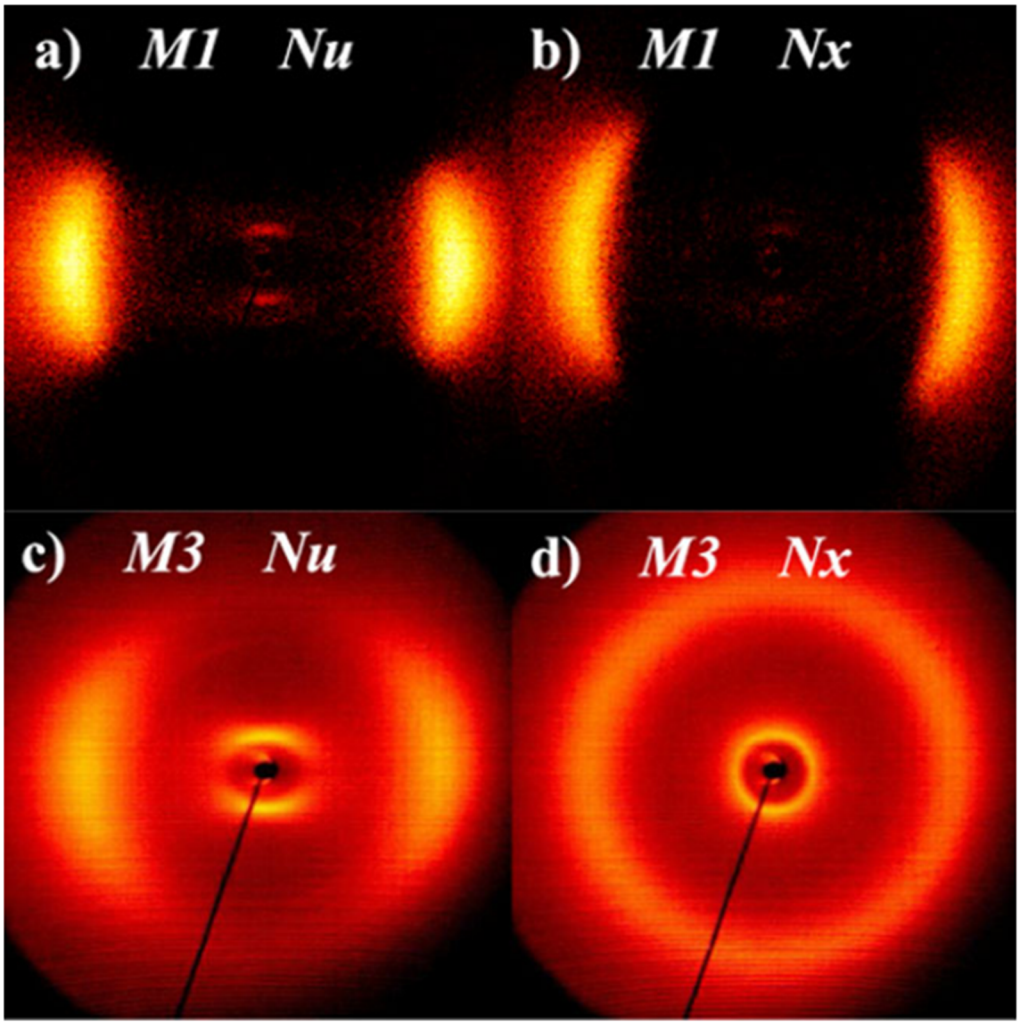

Figure 3.2.2: Conventional x-ray diffraction experiments on two different TB materials.
(a, c) The M1 and M3 materials are well-aligned vertically in their conventional nematic phases (uniaxial nematic, "Nu" here). They both exhibit diffuse inner and outer arcs which correspond to density modulations along and transverse to the director, respectively, typical of usual nematic phases. (b, d) In the TB phase ("Nx" here), the arcs become more distended and circular, indicating that the molecules are disordering or orienting away from the vertical direction. The peaks do not sharpen significantly through the phase transition. Reprinted from ref. [78].

3.2.3. Molecular structure of TB-forming LCs

The LC community today recognizes that the bent shape of the molecule plays a crucial role in the likelihood of observing the TB phase. This consensus is informed by a number of pieces of evidence: Dozov's TB model requires bent molecules to drive a preference for negative bend elasticity in the nematic phase [75], Memmer observed a TB-like phase in simulations of bent objects [76], and the vast number of forming LCs which featuring considerable molecular curvature that form the TB phase (Figure 3.2.3). All TB-forming LCs have substantial molecular curvature (bend). The vast majority are dimers [78,90,93,97–116], though there are a growing number of short oligomers as well [95,108,117–121]. There are only two examples each of rigid bent-core LCs [91,115] and hydrogen-bonded LCs [103,116] that form the TB phase. The archetypal TB-forming LC is a dimer composed of rigid rod-like arms which, on their own, tend to feature nematic phases. These arms are then linked together with an alkyl linker of an odd number of units to support an average bent shape of the molecule (Figure 3.2.4).

A number of groups have studied the effects of the bend angle on the properties of the TB phase. Cestari *et al*. calculated the probability distribution of the angle between the terminal cyano groups in CB7CB in the nematic phase for two different values of the order parameters, finding that it peaks around ~115° [48]. Greco *et al*. used a Maier-Saupe theory for bent objects to study the behavior of the TB director field as a function of temperature for bend angles 140°, 135°, and 130° [122]. Dawood *et al*. used the predictions from Greco *et al*. to guide their synthesis of a molecule with a rarely observed Iso (isotropic) – TB transition [106]. Mandle *et al*. performed a

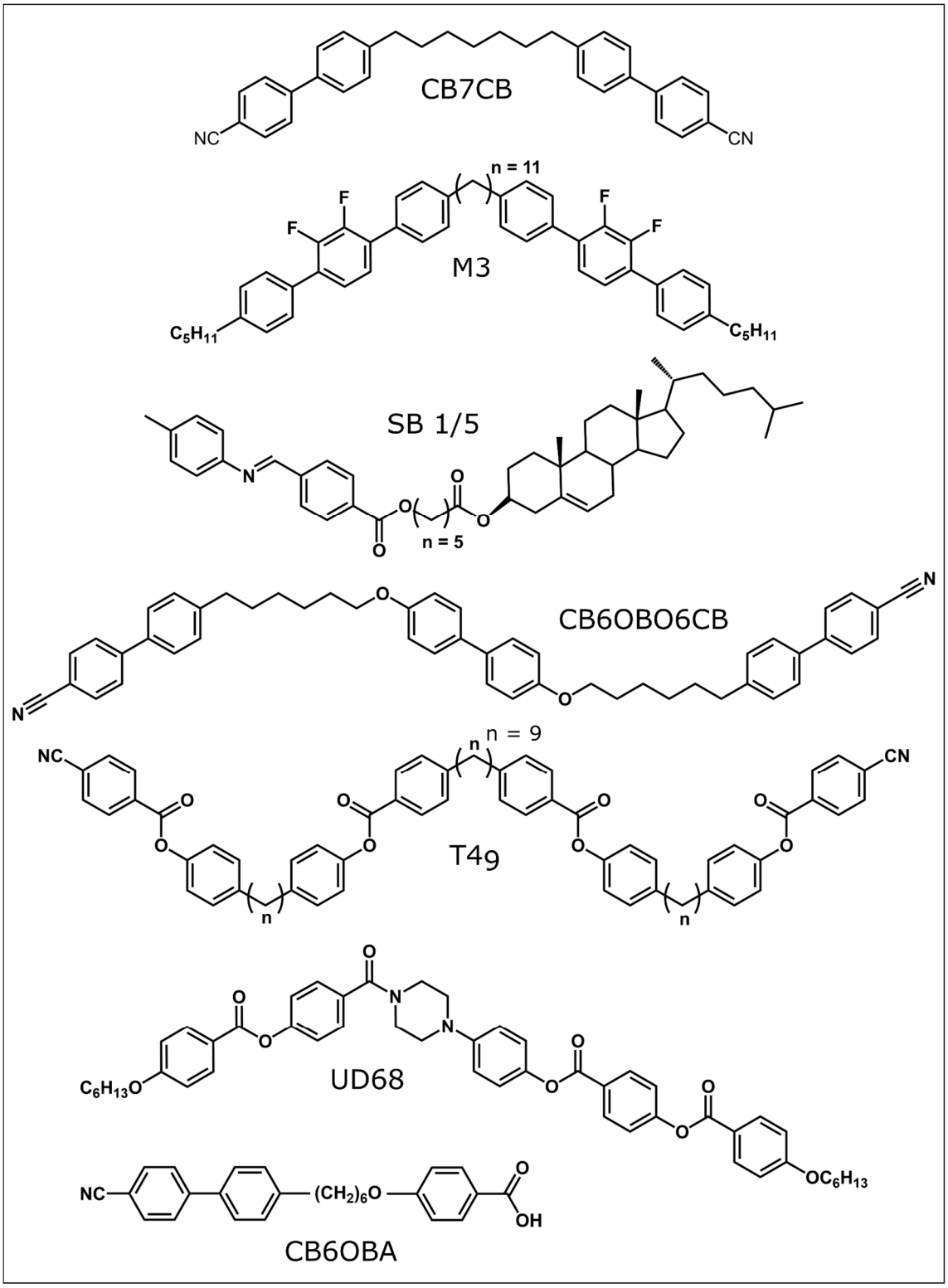

Figure 3.2.3: Chemical structures of selected TB-forming materials.
Molecules which form the TB phase include symmetric dimers (CB7CB [48,78], M3 [78]), asymmetric dimers (SB 1/5 [93]), short oligomers (CB6OBO6CB [120,121], $T4_9$ [118]), rigid bent-core molecules (UD68 [91]), and hydrogen-bonding complexes (CB6OBA [103]).

detailed study of bent dimers with different linking groups yielding a variety of bend angles and linker flexibility [107]. They showed that the TB phase could accommodate a range of bend angles, but that the alkyl linker provides the most thermodynamic stability for the phase. Archbold *et al.* followed up this study by calculating the conformational distributions for a number of the materials they had reported [112]. They found that the thermodynamic stability of the TB phase comes not only from the average bend angle of the molecule but depends on the distribution of conformers of a TB-forming LC and the flexibility of the spacer. The relationship between the molecular bend and the properties and stability of the TB phase is still not clear. The LC community has yet to settle on the underlying rules of molecular design for TB materials to help guide chemical synthesis beyond meeting the basic requirement of a molecule with bend. This will continue be a challenge in the future.

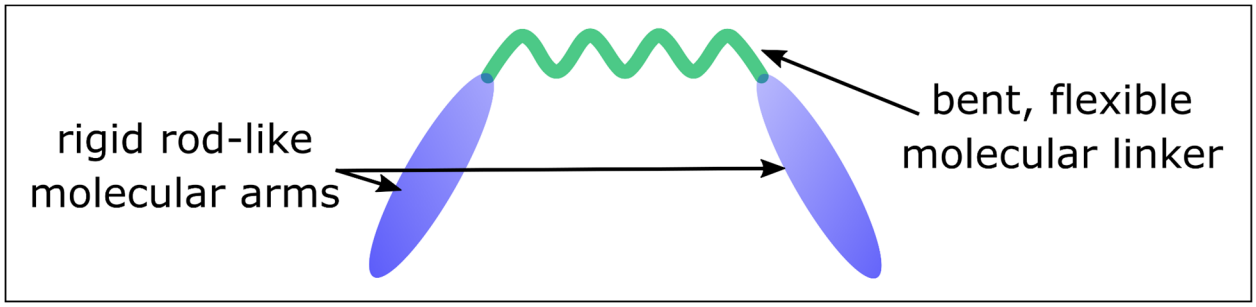

Figure 3.2.4: Schematic of the archetypal molecular geometry of a TB-forming dimer LC.
TB-forming molecules are most commonly dimers composed of two rigid rod-like units (blue) tethered together by a flexible chemical linker (green) of an odd number of units, enforcing molecular bend.

3.2.4. Spontaneous chirality in the TB phase

One of the first inklings of chirality in the TB phase of CB7CB came from Panov *et al.*, who proposed that the electric field effects they measured might be caused by a helical structure uniformly lying in the plane of the cell [123], though they did not attach much weight to this possibility. In a subsequent paper, observed electric field effects in PLM experiments of CB7CB in the TB phase which are typical of chiral systems [124], noting the growth of large domains perpendicular to the rubbing direction in a rubbed cell. These domains were not observably distinct until an electric field was applied, leading to the alternation of dark and light domains (Figure 3.2.5a,b). In 2013, Meyer *et al*. did their own PLM investigation which agreed with the work of Panov *et al*. [124], though they could even observe brightness alternation in TB domains by simply uncrossing the polarizers – not requiring the application of an electric field [125]. When they applied a DC electric field perpendicular to the helix axis, they noted a uniform tilt of the optic axis of the TB phase, only possible in chiral LC phases. They positively identified the electroclinic effect in a uniform lying helix structure and estimates the helix pitch of the TB phase to be ~7 nm at higher temperatures and half that value at lower temperatures. This estimate, as we will see, yielded the correct length-scale of the TB pitch and its temperature-dependence. They claimed that the identification of the electroclinic effect in a nematic phase composed of achiral molecules is diagnostic of the TB phase. Chen *et al*. observed the same behavior in an achiral rigid bent-core molecule which forms the TB phase [91] (Figure 3.2.5a,b).

The other experimental method that has been used to demonstrate chirality in the TB phase is nuclear magnetic resonance (NMR). In 2011, Cestari *et al*. measured the NMR spectra of a deuterated CB7CB sample, with the deuterons attached to the 1’ and 7’ carbons in the flexible

alkyl linker(Figure 3.2.5a,b), along with a number of other samples of CB7CB with deuterated dopants [48]. The spectra indicated that on cooling from the nematic to the TB phase, the 1' and 7' deuterated alkyl groups lose their spectral equivalence, denoting the onset of chirality in the TB phase. They claim that their experiments are consistent with a phase of a single handedness, or with both left- and right-handed domains with slow diffusion of molecules between the two domains. Beguin *et al*. performed a more focused NMR experiment on the TB phase using a variety of deuterated materials (neat, mixtures, and solvents) and came to the same conclusions [126]. Hoffmann *et al*. used NMR to investigate CB9CB, finding the same loss of equivalence of the deuterated chemical groups [79]. However, they proposed a different model for how the chirality manifests in the phase, proposing left- and right-handed domains composed of molecules self-sorting by their chiral conformations, but without a chiral or helical superstructure. Though Hoffmann *et al*. lacked a compelling alternative to the TB model, they highlighted the fact that there were still gaps in our understanding of the TB phase to this point.

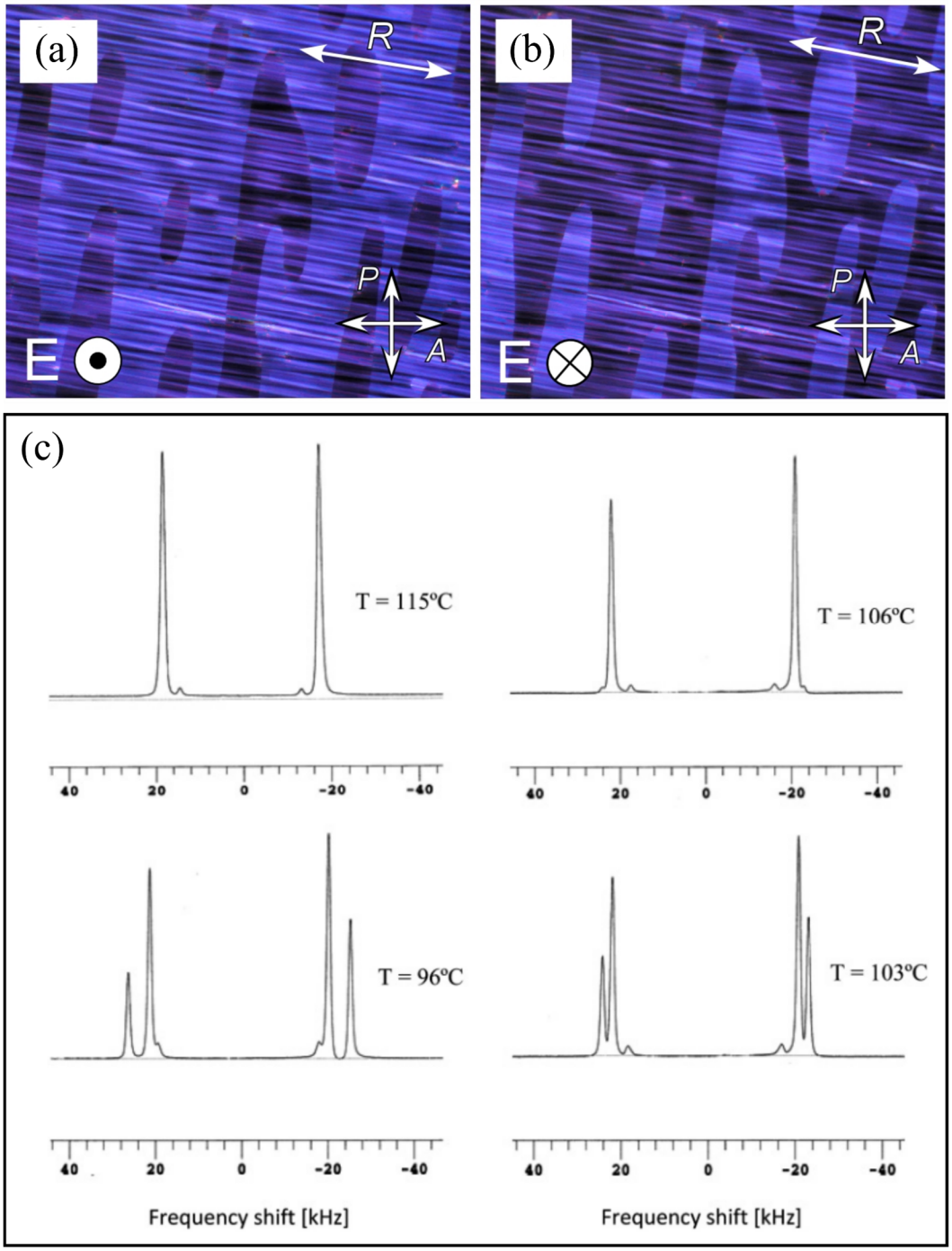

Figure 3.2.5: Evidence for chirality in the TB phase.
(a,b) PLM textures of UD68 in the blocky texture of the TB phase. The phase is well-aligned along the rubbing direction **R**. On application of an electric field into (out) of the page, the domains alternate between dark (bright) and bright (dark). This indicates that the two types of domains are of opposite handedness and that the TB phase forms with relatively large conglomerate domains of equal volume in a given cell. (a,b) reprinted from ref. [91]. (c) NMR experiments on a deuterated CB7CB molecule with deuterons in the 1' and 7' position of the alkyl linker exhibits a peak splitting on transition to the TB phase (T = 103°C), denoting an inequivalence of the 1' and 7' deuterons. This can occur if CB7CB exhibits a chiral or helical conformation, or the 1' and 7' deuterons are present in a chiral environment. (c) reprinted from ref. [48].

3.2.5. Nanoscale orientation modulation

Researchers initially assumed that the nanoscale structure of the TB phase was smectic because of the blocky and focal conic textures in the PLM which generally characterize smectic phases (see section 3.2.1) [77]. The presence of such smectic-like textures, including focal conic defects, indicates the presence of a well-defined structural periodicity below the wavelength of light. However, x-ray diffraction experiments provided evidence for the nematic nature of the TB phase [78]. This was the first inkling for the possibility of a unique nanoscale structure accompanying the nematic ordering in the TB phase.

As mentioned in section 3.2.4, Meyer *et al*. used the presence of an electroclinic effect to estimate the pitch of the TB helix to be ~7 nm based on the electric field switching speed and other known and estimated quantities characterizing the TB phase [125]. Direct evidence of a nanoscale structure was observed soon after. In 2013, the Boulder and Kent State University groups independently published results of FFTEM experiments on the TB phase of CB7CB, demonstrating a 1-dimensional periodic topographical modulation in the surface of the FFTEM replica (Figure 3.2.6) [59,85]. A lack of half-order layer reflections in a spatial Fast Fourier Transform of the images led the Boulder group to conclude that the period of the topographical modulations was in fact the helix pitch of the TB phase [59]. The smooth, consistent topography of the modulation indicates that there are no weak interfaces parallel to the layers, pointing to the homogeneity of the structure making up the modulation. They used geometric arguments about focal conic domains to determine the TB pitch to be 8.6 nm. The Boulder group then searched for a signature of the periodicity observed in FFTEM using small angle x-ray scattering from a synchrotron x-ray light source. They found no scattering signal in a search around the value of the

FFTEM periodicity and its 2nd and 3rd harmonics, leading them to conclude that the FFTEM modulations come with no associated electron density modulation.

The Kent group obtained results which were in agreement and complementary to the work done by the Boulder group [85]. They measured a TB pitch of ~8 – 9 nm, though they do not describe in detail how they obtained this range. Perhaps most significantly, they observed Bouligand arches in the sample [127] which provide definitive experimental evidence of the

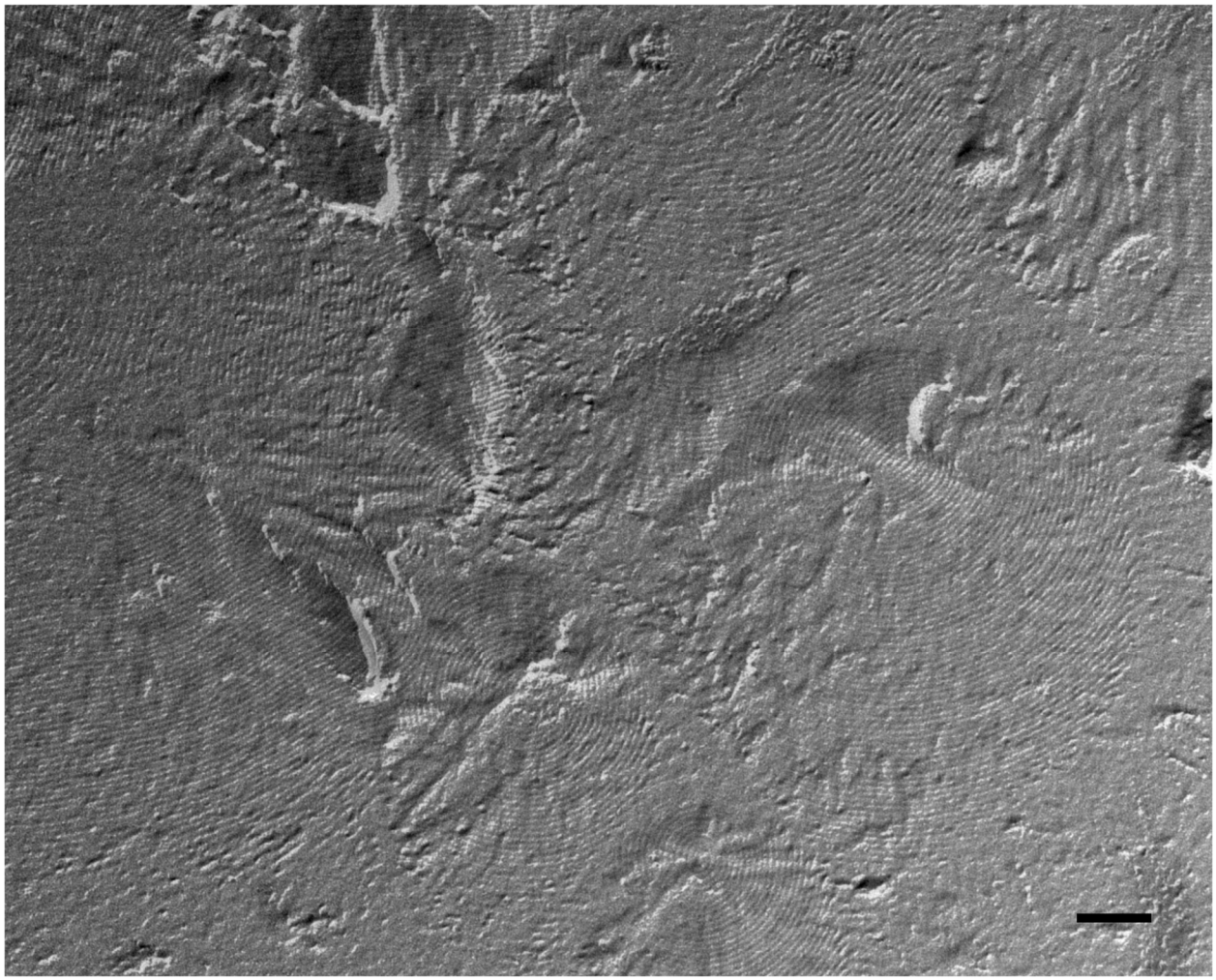

Figure 3.2.6: FFTEM image of CB7CB in the TB phase.
The topography of the fractured surface of the TB phase exhibiting curved sinusoidal modulations, indicating a fluid, periodic nanostructure in the TB phase. The surface modulation has a period of ~8 nm, indicating that the TB helix pitch is near 8 nm. The scale bar is 100 nm.

helical nature of the TB phase. Thus, the community became quite confident in the determination of the TB phase as a heliconical TB nematic structure with a nanometer scale pitch.

The FFTEM experiments demonstrated the existence of a nanometer scale helical pitch. But they only measure the fractured surface of the TB material vitrified at a particular temperature. This indirect method made investigating the thermodynamics of the TB phase quite difficult. Therefore, the Boulder group and Chenhui Zhu from the Advance Light Source at Lawrence Berkeley National Laboratory used resonant soft x-ray scattering (RSoXS) to measure the forbidden Bragg scattering signal directly from the helix pitch of the TB phase of CB7CB [70] corresponding to the FFTEM modulations observed earlier [59,85]. This particular technique had been demonstrated for LCs in the helical nanofilament phase only a year earlier [69].

In addition to providing further evidence that the FFTEM feature was one of orientational molecular organization in the absence of electron density modulation, we became sensitive to the temperature-dependent variation of the TB helix pitch *in-situ* [70]. We found that the pitch was 9 – 10 nm at high temperature near the N – TB transition, and this abruptly approached 8 nm on cooling down to room temperature (Figure 3.2.7). We showed this behavior was reproducible on heating and cooling in CB7CB. Curiously, at high temperatures near the N – TB phase, we found many distinct TB domains characterized by different pitch lengths existing at the same temperature. We attributed this to an asymmetric response of the TB helix to stretching and compressing, along with boundary pinning effects which tend to constrain the pitch. RSoXS has since become the preferred method of studying the TB nanoscale pitch, and a number of other studied have since used resonant x-ray scattering techniques to investigate the TB phase [111,128–130].

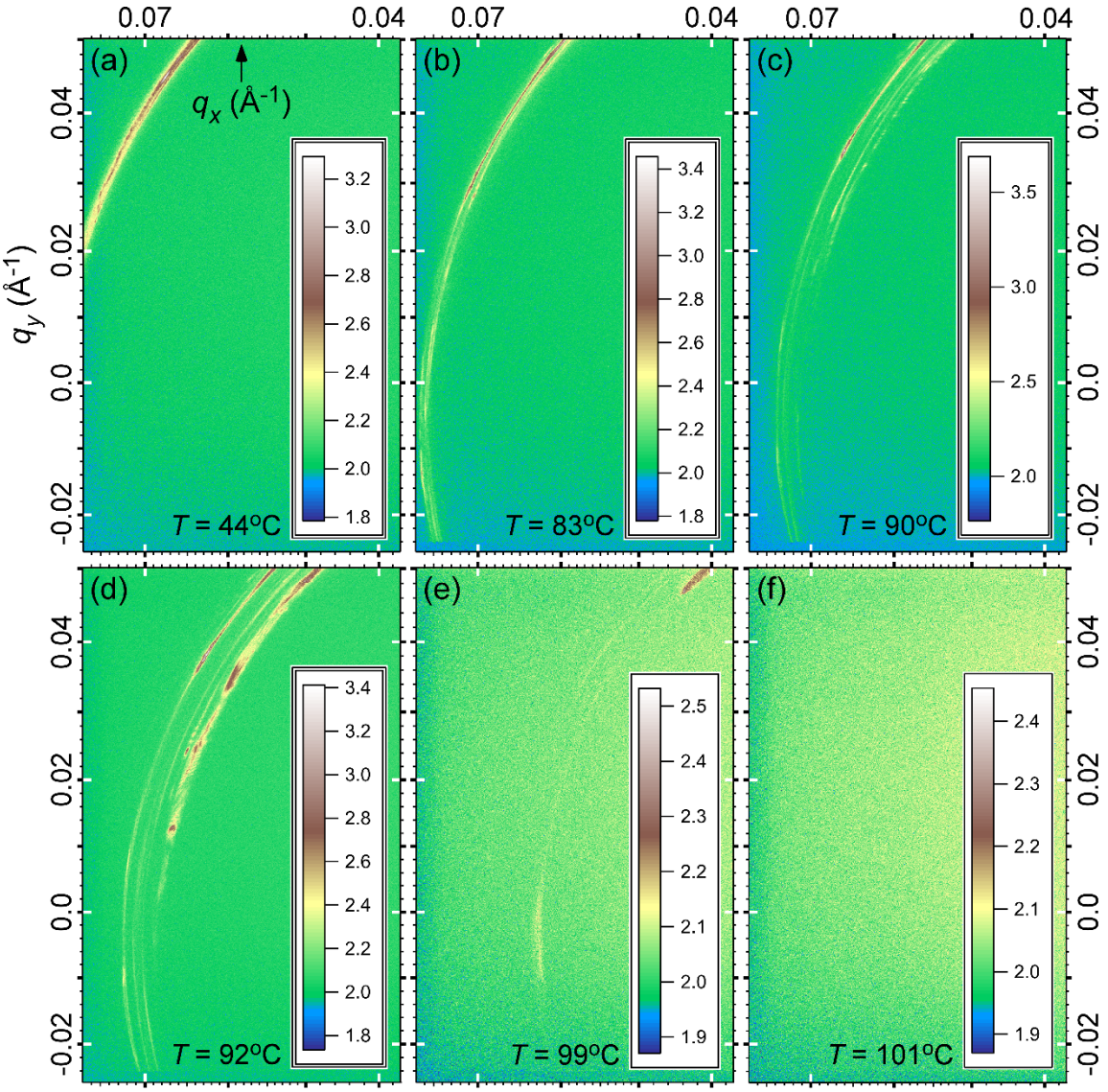

Figure 3.2.7: RSoXS detector images of CB7CB on heating.
The axes are in terms of the q_x and q_y, the components of the scattering wavevector **q**. The arcs in these images correspond to the helix pitch p by the equation $\mathbf{q} = 2\pi/p$. (a) At low temperature in the TB phase, there is a single scattering arc, indicating a collection of randomly oriented TB domains with the same helix pitch. (b-d) On further heating, the initial scattering arc splits into many arcs, indicating that the TB domains are exhibiting a variety of well-defined helix pitches. (e) Near the TB – N transition, the arcs fade away, indicating melting of most of the TB domains. (f) Above the TB – N transition, there is no resonant scattering, indicating a lack of orientation modulation in the nematic phase, as expected. Reprinted from ref. [70].

In the RSoXS experiment lies the most significant outstanding question about the TB model in my opinion. The researchers involved in RSoXS measurements, including myself, have searched without success for a scattering signal which corresponds to the half of the TB pitch. This

signal should be present as we now understand it unless there is a particular and special cancellation occurring in the structure factor of the phase. The lack of scattering where we would expect it puts strong constraints on the types of intermolecular organization possible in the TB phase, and necessitates either a super-structural assembly of the TB helices which necessarily rigorously cancels the expected scattering (such as half the helices being shifted by $p/4$ with respect to the other half [130] in a double or multi-helix structure), or there is some other significant aspect of the structure which we do not know about. In my opinion, this is the most significant experimental hurdle in the understanding of the TB phase today.

3.2.6. The TB cone angle

The nematic and TB phases of typical LCs are uniaxial with positive dielectric anisotropy. This implies that the cone angle θ of the TB phase must be below ~45°. Although one study estimated the value of the TB cone angle [125], it was not studied in detail until 2015. Meyer *et al.* developed a simple methodology for estimating the temperature-dependence of the cone angle [131] in which they first performed a detailed birefringence experiment on the phases of CB7CB as a function of temperature. Then, they fit the data in the nematic phase to the Haller formula [132] to determine the unknown parameters in the equation. By assuming that the birefringence drops solely because of the increasing tilt of the cone angle from zero in the nematic (i.e., not taking order parameter or other factors into account), they wrote a formula for the cone angle $\theta(T)$ as a function of $\Delta n(T)$. Measuring CB7CB using this procedure, they found that θ begins at ~10° and rapidly increases on cooling, until it approaches ~36° at low temperature. This makes

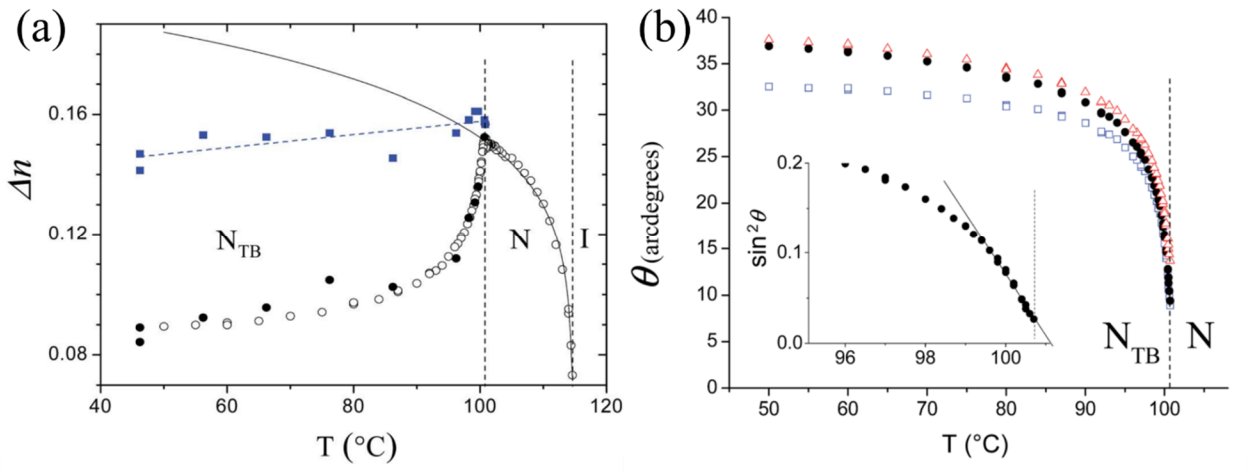

Figure 3.2.8: Birefringence and estimated cone angle of CB7CB as a function of temperature. (a) The birefringence behaves as a typical nematic phase (open and closed circles), following the behavior described by the Haller formula (solid line). On transition to the TB phase near 100°C, the birefringence drops dramatically, indicating that the molecules are orienting away from the direction of the original nematic. (b) The estimated cone angle of CB7CB in the TB phase, estimated using a procedure developed by Meyer *et al*. Reprinted from ref. [131].

for a good approximation of the behavior of the TB cone angle. However, we developed a more complete method which yields the true TB cone angle in principle (Figure 4.2.7) [121].

Around the same time, Jokisaari *et al*. [133] and Robles-Hernández *et al.* [134] determined the cone angle using NMR and an estimation scheme in a vein similar to that of Meyer *et al.* [131]. The NMR data depends on the tensorial order parameter and the cone angle as a function of temperature. Using this, these groups develop a methodology in which they fit the Haller formula with measurements from the higher temperature nematic phase [132]. Performing this analysis on deuterated CB7CB and mixtures of deuterated dopants with CB7CB, they found a temperature-dependent TB cone angle which starts at ~5 – 10° and increases on cooling, to approach ~25° at low temperature. This measurement roughly aligns with the TB cone angle determined from the birefringence measurements of Meyer *et al*. [131].

3.2.7. Simulations of TB phases

Despite the substantial number of experiments and studies on the TB phase, some details of the nanoscale structure of the TB phase have not been observed experimentally. From experiment, we understand the macroscopic symmetries of the phase and the scale of nanoscale modulation and tilt, but not precisely how the molecules are arranged locally. Presently, the best way to "look" at what each molecule is doing is to perform computer simulations.

Memmer published the first simulation of bent objects which exhibit a phase similar to the TB phase [76] (Figure 3.1.2), and he highlighted the similarities between what he found and the TB phase of Dozov, [75]. Since then, a number of groups have reported the results of atomistic simulations [59], bent particles [135], and helical particles [136], all of which exhibit a phase with the same symmetries and general properties as the TB phase.

Beyond verifying the experimental findings of the TB phase, simulations have the potential to elucidate the precise superstructural arrangement of the molecules and their intermolecular interactions, features which are difficult to determine experimentally. In unpublished work by the Boulder group, Joseph Yelk has been investigating the detailed structure of the TB phase from the atomistic simulations completed by the Utah simulations group in ref. [59]. By plotting 2D correlations of various chemical groups in the CB7CB molecule, he has uncovered evidence that the molecules are triply associating, with the end-to-end associations of vertically displaced molecules coupling with the central carbon of a laterally neighboring CB7CB molecule with high probability. This indicates that the CB7CB molecules are forming transient helical chain structures, held together by the triple associations. From this, he can determine how neighboring chains associate: randomly, on a lattice, into double or multiple helical chain structures, or in some

other way. This work will hopefully shed light on the lack of a 2nd harmonic in the RSoXS measurements as well. With these simulations, we will be able to calculate the expected RSoXS diffraction pattern and investigate the expected RSoXS half-pitch scattering features of the TB helix.

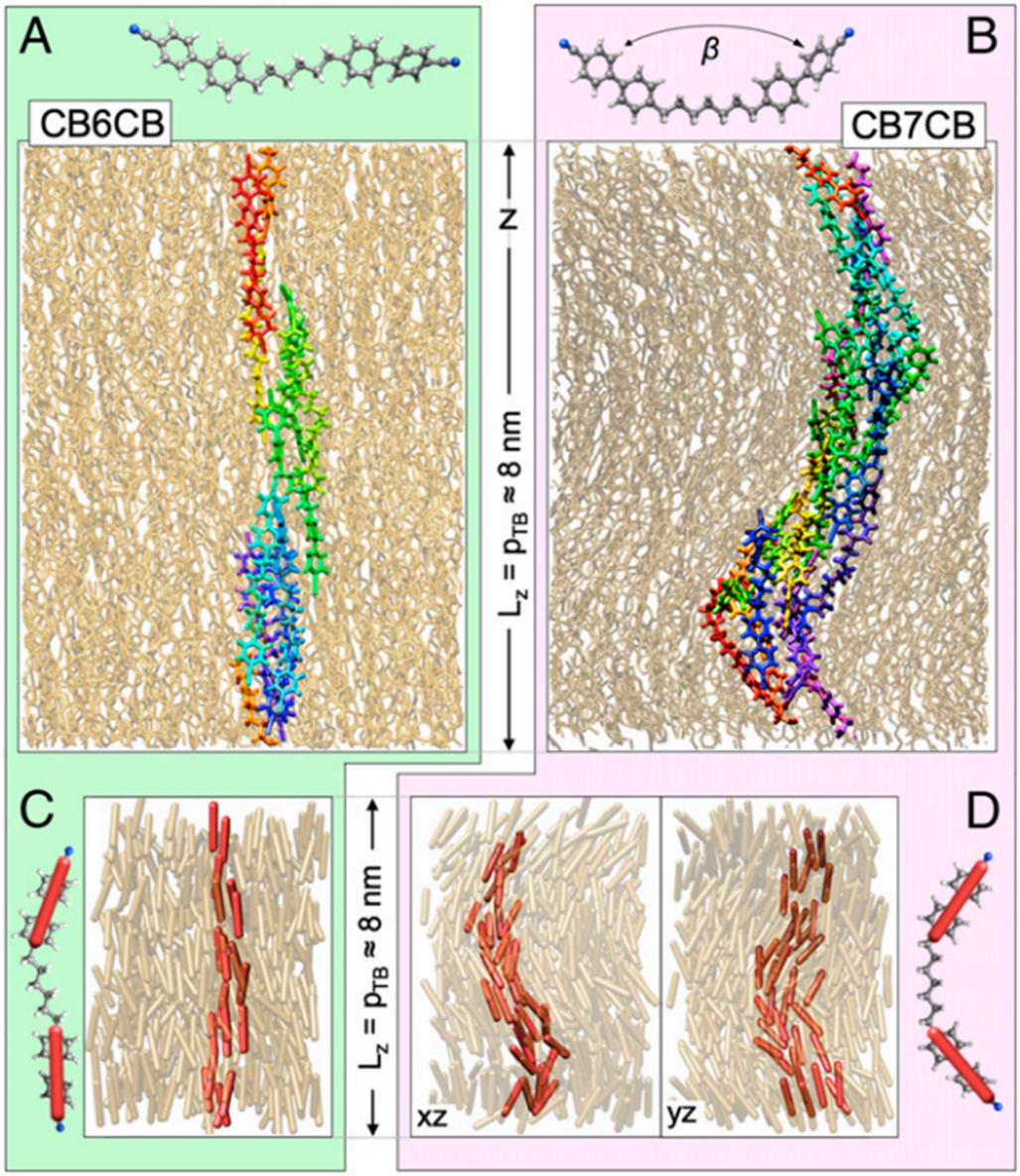

Figure 3.2.9: Atomistic simulations of CB6CB and CB7CB.
(A,C) CB6CB exhibits only the usual nematic LC phase. (B,D) CB7CB, however, exhibits the heliconical organization of the TB phase with a pitch of ~8 nm, in agreement with RSoXS and FFTEM measurements. Reprinted from ref. [59].

3.2.8. Theoretical descriptions of the TB phase

Since the recognition of the TB phase, theorists have been evaluating aspects of Dozov's theory of the TB phase [75], either attempting to improve on it or creating a new theory to explain the experimental observations that continued to be reported. Though many of Dozov's predictions have been borne out by experiment, including an N – TB spontaneous reflection symmetry breaking phase transition [124,126] and a uniform TB cone angle [131,133,134], other predictions, such as a negative bend elastic constant in the TB phase [84] and an estimated of ~300 helix pitch [59,85] have not been observed. Therefore, most scientists in the LC community acknowledge that Dozov's work guided the investigation of the TB phase and provides a good 1st order approximation to the phase, but it is not the final answer to the fundamental nature of the TB phase.

Shamid *et al*. were among the first to modify Dozov's model [137]. They recognized that in considering the Frank elastic free energy of a system that forms the TB phase, because the TB phase is inherently polar (the molecular bends helically precess and point uniformly at a given z) one must consider polarization and bend flexoelectricity contributions to the nematic free energy equation. By doing this, one can minimize the energy with respect to the polarization and group the terms which depend on bend elasticity. The new coefficient is a "renormalized" bend elastic constant, which can become negative at a critical temperature. This can stabilize a nematic phase with spontaneous bend and twist, permitting the formation of the TB phase.

Greco *et al*. used a Maier-Saupe molecular field theory treatment generalized to bent objects. With this, they were able to study the onset of the TB phase and its elastic properties as a function of the bend angle of the objects [122]. Thus, they calculated the temperature-dependence

of various order parameters and the TB pitch and cone angle. In addition, they studied the deformation free energy density as a function of the TB pitch and cone angle, which permits a detailed comparison with RSoXS. This treatment agreed with evidence in CB7CB, which exhibits a large distribution of TB pitches at higher temperature and a softness to dilation but stiffness to compression [70]. At present, this model appears to describe the most experimental features about the TB phase. However, a similar treatment by Vanakaras *et al*. comes to somewhat different conclusions for the nature of the TB phase [82].

A large body of theoretical work has arisen since the identification of the TB phase, all of which approach the TB phase from different theoretical angles and expound on distinct aspects of its structure, order, phase transitions, etc. [138–150]. A comprehensive TB theory will be critical for our understanding of the TB phase and for the future of this phase as a potential technology.

4. EXPERIMENTAL INVESTIGATIONS OF THE TB PHASE: NANOSCALE BEHAVIOR, STRUCTURE-PROPERTY RELATIONSHIPS, AND THE EVOLUTION OF THE TB MODEL

Currently, there are a number of significant gaps in our understanding of the TB phase. Though we know that the TB phase is a nematic with a heliconical symmetry and nanoscale pitch, we do not know if there is any further hierarchical organization. Evidence shows that the molecules couple at their ends to form transient oligomeric helical chains in the TB phase (sections 3.2.7 and 4.2), but these chains may either remain independent of each other or form duplexes or multiplexes or other structures with other chains in their vicinity.

In addition, we still do not confidently understand why the TB phase forms or why so few materials have been shown to exhibit the TB phase so far. A considerable number of flexible linear dimers and oligomers have been studied in the past and bent-core LCs were heavily investigated for the last 25 years or so. These might appear to be good candidates for the TB phase because of their intrinsic molecular bend. However, they nearly always form positionally-ordered LC phases, like smectic and columnar phases. It is possible that suppression of these positionally-ordered phases in favor of nematic phases would yield considerably more examples molecules with the TB phase, though this has not been thoroughly investigated. The resolution of this mystery will likely benefit from theory and the synthesis of additional TB-forming LCs.

The chemistry branch of the LC field is continuing to map the chemical structure phase-space of the TB phase. We only know of two or three molecular design motifs for the TB phase: bent oligomers with flexible linkers make up the vast majority of LCs that form the TB phase, with only two examples each of rigid bent-core molecules and hydrogen-bonded bent LC complexes (section 3.2.3). An investigation of other design motifs will enable us to observe the scope of

possible variations in the properties of the TB phase, provide further insight into the nature of the TB phase, and yield more material candidates for technological applications.

One of the most interesting aspects of LCs is their "structure-property relationships": this is the idea that varying aspects of the chemical structure of an LC affects the organization and properties of the phases it forms. For instance, by changing the structure of a rod-shaped LC to one without mirror symmetry with the addition of a single chemical group, we can observe dramatically different LC phases featuring chirality and leading to unique material properties (e.g. conventional nematic phase → cholesteric phase). The LC community is still investigating the fundamental structure-property relationships of the TB phase by varying the chemistry of the tails, rigid arms, and flexible linker. This is one approach LC scientists use to discover, investigate, and ultimately design LC phases with novel, interesting properties.

In the following sections, I summarize the work of myself and my colleagues and collaborators in answering some of these remaining questions.

4.1. The Boulder model of the TB phase

Our present understanding of the structure of the TB phase comes from experimental evidence, including that from the work in the following sections: The TB phase is a nematic, with only short-ranged positional ordering of the molecules [78] and with long-ranged heliconical orientational ordering about an axis z [125]. The TB phase has a helical pitch p_{TB} generally a few times the length of the molecule [59,70,85], and they are tilted, with their orientations lying on a cone with cone angle θ_{TB} [48,131]. The the short-ranged positional modulation along the TB helix has a characteristic spacing s_{TB} [151], indicating intercalation of the molecules over the length of

one of the monomers making up the molecule (2 monomers in a dimer, 3 in a trimer, etc.), and with an azimuthal rotation of the molecules $\Delta\varphi_{TB}$ per s_{TB}. The TB phase is borne out of spontaneous chiral and polar symmetry breaking from the nematic phase, leading to large conglomerate domains of left- and right-handedness in a sample generally consisting of achiral molecules [91,124,125]. The molecules couple and overlap at their ends by ~3 Å, forming transient helical chain structures (section 4.2). These chains fill space, with neighboring chains displaced in z by s_{TB} (to enforce intercalation) and with the helical phase the same for any given position in z. See Figure 4.1.1 for the model.

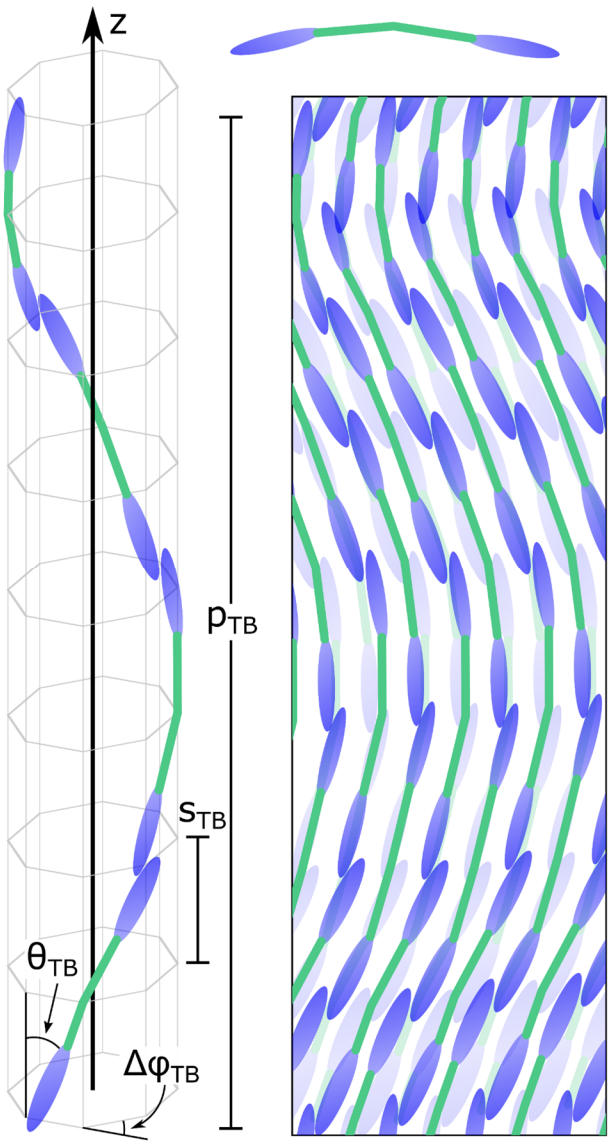

Figure 4.1.1: Boulder model of the TB phase. We model a dimer with two rigid rod-like units in blue attached by an alkyl-based spacer in green, bent in the middle for ease of drawing. The TB phase is depicted with the director precessing on the surface of a polygonal prism, with the shape of the polygon enforcing the azimuthal rotation $\Delta\varphi_{TB}$. In this case, we show an octagonal prism enforcing $\Delta\varphi_{TB} = 45°$. The polygonal prism is composed of levels spaced by s_{TB} and with the monomer units of the molecules lying along the diagonal of an outer rectangular face of the prism with cone angle θ_{TB}. The ends of the molecules overlap each other at the corners of the octagon by several Angstroms. This then forms a transient chain structure with pitch p_{TB} some multiple of s_{TB} ($p_{TB} = 8s_{TB}$ here, not necessarily commensurate in real materials). These chains fill space, with neighboring chains intercalated and twisting in phase.

4.2. Distinct differences in the nanoscale behaviors of the TB phases of dimer and trimer members of a family of flexible linear oligomers

We synthesized the LC dimer and trimer members of a series of flexible linear oligomers and characterized their microscopic and nanoscopic properties using resonant soft x-ray scattering (RSoXS) and a number of other experimental techniques. On the microscopic scale, the TB phases of the dimer and trimer appear essentially identical. However, while the LC dimer exhibits a temperature-dependent variation of its TB helical pitch, varying from 100 – 170 Å on heating, the trimer exhibits an essentially constant pitch of 66 Å, significantly shorter than those reported for other TB-forming materials. We attribute this to a specific combination of intrinsic conformational bend of the trimer molecules and a sterically favorable intercalation of the trimers over a commensurate fraction (two-thirds) of the molecular length. We developed a geometric model of the TB phase for these materials with the molecules arranging into helical chain structures, and fully determined their respective geometric parameters [121].

LC compounds with two or more rigid monomer units connected by flexible linkers can exhibit unique assemblies not encountered in other LCs. LC oligomers bridge the structure-space between conventional small molecule LCs and polymer LCs. This structural motif has generated considerable interest in the LC field because their chemical make-up induces odd-even effects and unique intercalated smectic phases [1,2].

In addition, there have been a number of accounts of short oligomers which form the TB phase [103,95,152–154,120]. However, only one nanoscale structural investigation has previously been performed on TB-forming oligomers of three or more monomeric units [59], although in that

case the compound was not a conventional linear trimer but a bent-core hybrid molecule. A number of studies have found through conventional x-ray diffraction techniques that trimers and tetramers tend to be heavily intercalated in the nematic and TB phases [95,153], but to our knowledge, little other characterization of the nanoscale structure of the TB phase has been carried out on linear, unbranched LC *n*-mers with $n > 2$.

Here, we describe the synthesis of an LC molecular trimer which we designate CB6OBO6CB. We perform a number of nanoscale characterization techniques, including resonant soft x-ray scattering (RSoXS), wide-angle x-ray diffraction (WAXS), and freeze-fracture transmission electron microscopy (FFTEM), and contrast the results to those of the analogous dimer molecule CB6OCB which also forms the TB phase [109]. While CB6OCB exhibits a TB pitch which varies considerably from p_{di} = 100 – 170 Å, we find that CB6OBO6CB exhibits a pitch p_{tri} = 66 – 67 Å over the ~20°C range of its TB phase, making it effectively temperature-independent and the smallest TB-pitch yet reported. Because this molecule is significantly longer than most other conventional TB-forming LCs, we find such a small pitch extraordinary. We account for this fact by considering the degree of intercalation possible in CB6OBO6CB, which permits a sterically favorable interlocking of molecules over ~2/3 of their molecular length, thereby constraining the flexibility and suppressing fluctuations of the helical structure. Our characterization further permits us to construct detailed geometric models of the TB phase in each of these materials and to make predictions about the behaviors of the analogous higher oligomers.

We estimated the end-to-end length of CB6OBO6CB trimer and CB6OCB dimer in their extended *all-trans* conformations using the Spartan'16 molecular calculation and modeling software. Dihedrals connecting the rings to the alkyl chains were initially manually set at their

expected energy minima—values of 0 degrees for CR-CR-O-CT and 90 degrees for CR-CR-CT-CT (where CR is an aromatic ring carbon atom, O is an oxygen atom and CT the tetrahedral alkyl chain carbon). The trimer and the dimer were optimized to reach an equilibrium geometry, in vacuum in the ground state, using the semi-empirical AM1 method as an initial approximation. Subsequently, we initiated a second fully relaxed geometry optimization using the *ab initio* Hartree-Fock method with 6-31G* basis set.

Molecular end-to-end lengths for both the trimer and dimer were then determined by measuring the distance from one terminal nitrogen atom to the other and adding the length of 2 nitrogen radii. The end-to-end nitrogen-nitrogen distance of the trimer was l_{tri} = 46.0 Å, and was l_{di} = 30.4 Å for the dimer, very close to that estimated for the dimer in ref. [109]. We then determined the end-to-end molecular dihedral angles of the trimer by comparing one nitrogen-oxygen plane to the other nitrogen-oxygen plane, finding it to be 134.08°. To find the dihedral angle of the dimer, we compared the nitrogen-oxygen plane to a C_b-nitrogen plane (where C_b is the benzylic carbon attached to the cyanobiphenyl unit) and determined it to be 0.28°.

CB6OBO6CB (the "trimer"), contains three rod-like monomer units linked by two flexible spacers (Figure 4.2.1a). The odd number of atoms separating the monomer units ensures oligomer curvature, while the choice of the methylene link between the spacer and the monomeric cyanobiphenyl groups ensures a sufficient bend to make it a promising candidate to form the TB phase, by analogy to CB6OCB (the "dimer") [109].

We characterized the phase behavior of CB6OBO6CB with a combination of polarized light microscopy (Figure 4.2.1b, c) differential scanning calorimetry (Figure 4.2.1), and a contact

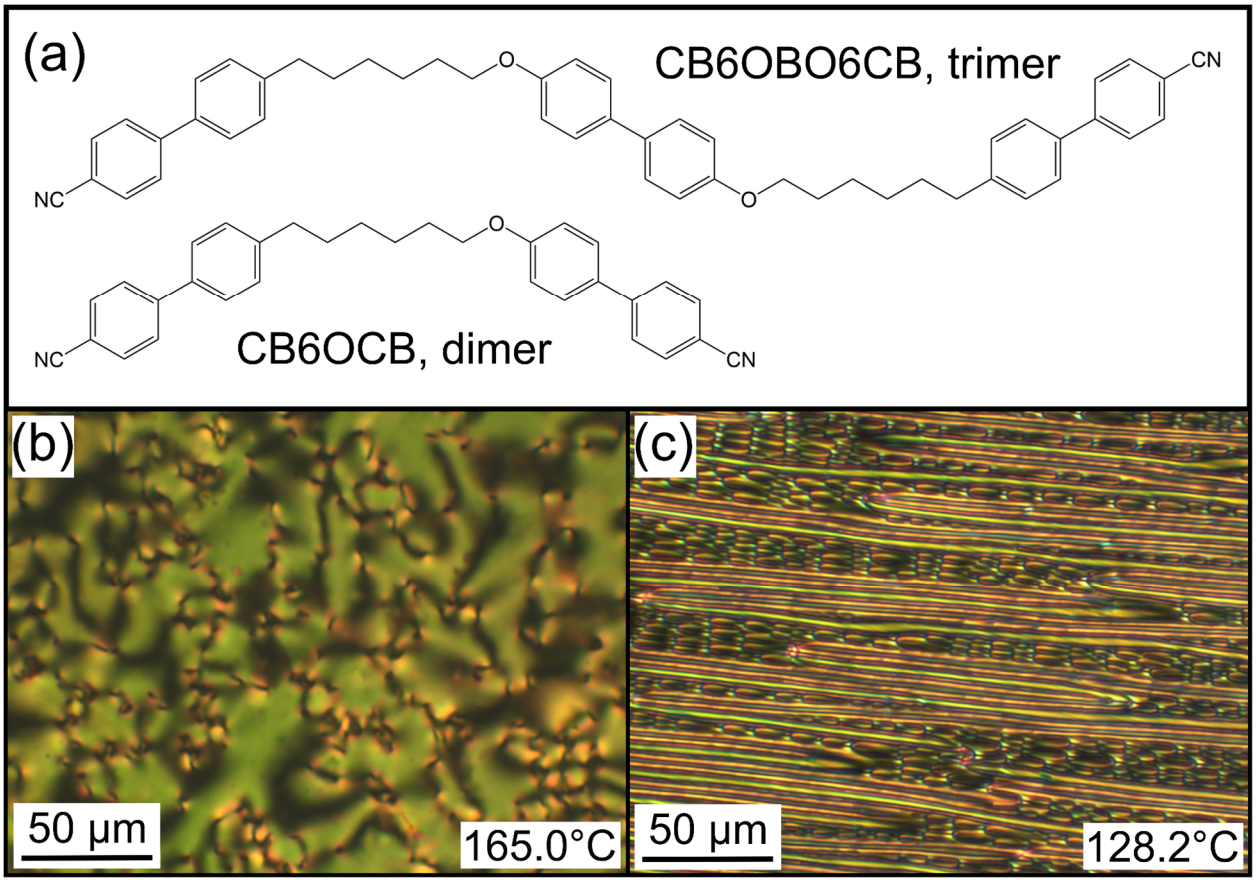

molecule	T_{Cr} (°C)	T_{TB-N} (°C)	T_{N-I} (°C)	ΔH_{Cr} (kJ mol^{-1})	ΔH_{TB-N} (kJ mol^{-1})	ΔH_{N-I} (kJ mol^{-1})	$\Delta S_{Cr}/R$	$\Delta S_{TB-N}/R$	$\Delta S_{N-I}/R$
CB6OCB	99	109	155	21.29	0.02	1.58	6.88	0.01	0.48
CB6OBO6CB	140	131*	169	64.51	1.33	1.81	18.78	0.40	0.49

Figure 4.2.1: Molecular structure of CB6OBO6CB and CB6OCB and phase characterization of CB6OBO6CB.
(a) Molecular structure drawings of CB6OBO6CB and CB6OCB, which we denote "trimer" and "dimer", respectively. Polarized light microscopy image of the trimer in the nematic phase (b) and the TB phase (c). The table includes measurements of thermal properties of these materials obtained by differential scanning calorimetry. These measurements demonstrate the existence of a monotropic phase below the uniaxial nematic phase in the trimer which we find to be the TB phase. The * symbol indicates a monotropic phase transition.

cell preparation of the trimer with CB7CB [48,59,70,85], a material well known to exhibit the TB phase. A typical uniaxial nematic texture forms on cooling from the isotropic phase in a unidirectionally-rubbed planar cell (Figure 4.2.1b). On further cooling, the nematic phase transitions into another phase which exhibits a blocky optical texture that then develops into well-defined stripes and focal conic defects (Figure 4.2.1c). These textures persist for ~20°C on further

cooling until the transition into the crystal phase. This behavior and the observed textures are fully consistent with the TB phase observed in LC dimers [48,78].

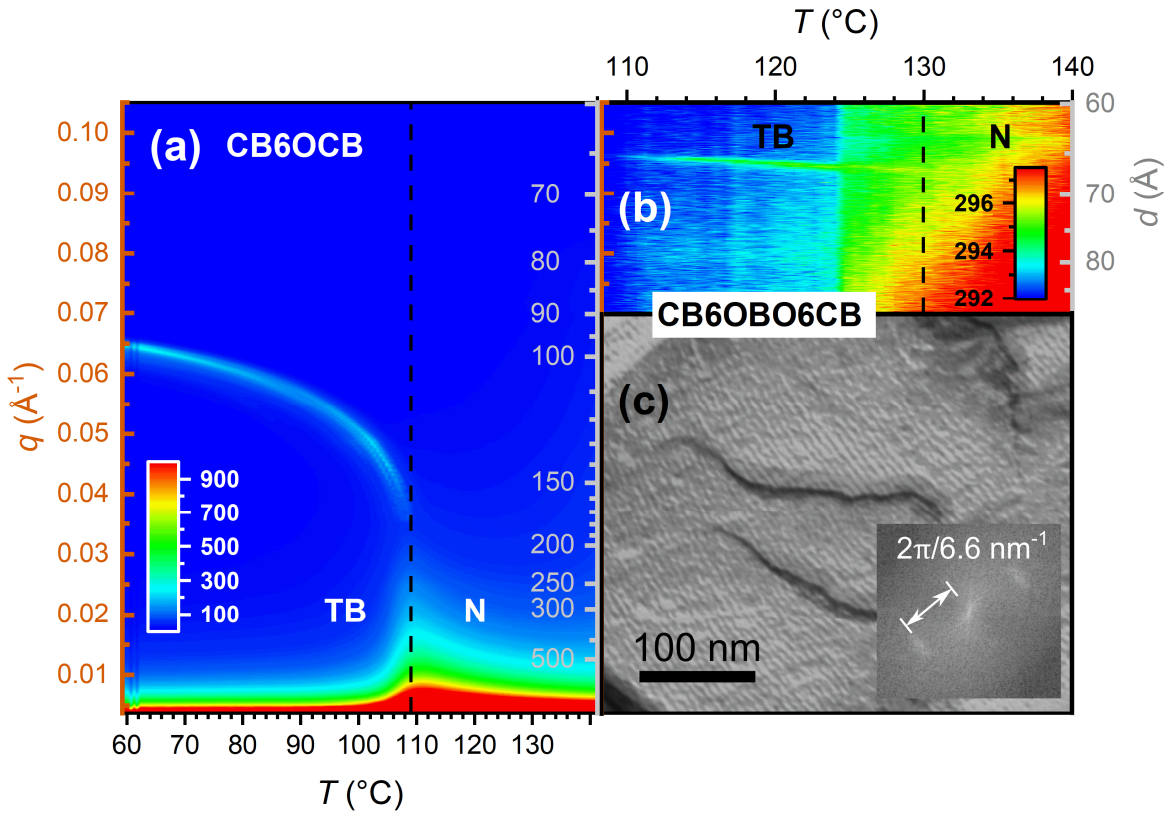

Figure 4.2.2: RSoXS of CB6OCB and CB6OBO6CB, and an FFTEM image of CB6OBO6CB. (a,b) The color plots are composed of line scans in q of azimuthally averaged 2D detector images taken as a function of temperature. The q and pitch d scales are the same across both plots. (a) CB6OCB exhibits usual temperature-dependent scattering behavior for conventional TB-forming dimer molecules. In the nematic phase, we observe no scattering features, as expected. On cooling to 108°C, a peak appears near $p_{di}(T = 108°C) \approx 170$ Å, corresponding to the TB helical pitch. On further cooling the helical pitch drops dramatically, then more slowly approaches $p_{di}(T = 60°C) \approx 100$ Å before crystallization. The exposure time was 3 seconds. (b) On cooling CB6OBO6CB from the nematic phase, a scattering feature appears near 130°C corresponding to a helical pitch of $p_{tri} = 67 – 66$ Å, remarkably short compared with that of CB6OCB and other known TB materials. The dashed line denoting the N – TB phase transition temperature was drawn where the TB phase scattering becomes clearly visible. The plot exhibits a slight discontinuity in the background scattering $T = 124°C$, which we believe to be due to thermal drift while we performed a beamline energy scan. The exposure time was 5 seconds. (c) Representative FFTEM image of CB6OBO6CB in the TB phase exhibiting sinusoidal topographical modulations at $p_{tri,FFTEM} = 6.6$ nm. In different regions of the trimer sample, we observe topographical modulations with a variety of periodicities, but the most frequently observed periodicity in the sample (when weighted by the area of occurrence) is 6.6 nm (see Figure 4.2.3).

The enthalpy of formation (ΔH) and the entropy change (ΔS) associated with the transitions are in the range of expected values for these types of transitions (Figure 4.2.1). It is noteworthy, however, that the entropy change associated with the N – TB transition is greater than would be expected based on the behavior of dimeric materials as well as the temperature width of the preceding nematic phase [113,152–154].

We subsequently performed RSoXS [70] on CB6OCB and CB6OBO6CB on cooling from the nematic phase. We converted the 2D RSoXS detector images into plots of $I(q)$ vs. q, the magnitude of the wave vector **q**, by azimuthally averaging the 2D diffractograms about $q = 0$. We then used the Nika x-ray data analysis and processing software to interpolate the 1D plots into a color map with q and the corresponding wavelength $d(q) = 2\pi/q$ plotted as a function of temperature, with the intensity in the 1D plots represented by the color scale in Figure 4.2.2a,b. On cooling from the nematic, CB6OCB develops a peak at $q(T = 108°C) = 0.0375$ Å^{-1}, corresponding to the TB helical pitch $d(q) = p_{di}(T = 108°C) \approx 170$ Å (Figure 4.2.2a). The helical pitch rapidly decreases, then begins to saturate near $p_{di}(T = 60°C) \approx 100$ Å before it crystallizes.

The determination of a TB pitch of ~90 Å for CB6OCB by FFTEM [109] roughly accords with our RSoXS measurement, given that FFTEM experiments tend to exhibit the value of the pitch extrapolated to low temperature in the TB phase [129]. CB6OBO6CB, on the other hand, exhibits a very different TB pitch behavior (Figure 4.2.2b). On cooling from the nematic phase, we begin to see unambiguous evidence of scattering from the TB helix at ~130°C. At 124°C, we held the temperature fixed and varied the beamline energy about the carbon K-edge resonance to check that the scattering feature was indeed resonant, confirming that the structure of this phase is modulated in molecular orientation and not related to electron density [70]. The scattering signal peaks at q_{tri}(high T) = 0.094 Å^{-1}, corresponding to a helical TB pitch of p_{tri}(high T) = 67 Å. On

further cooling, this peak shifts very gradually to q_{tri}(low T) = 0.096 Å^{-1}, corresponding to a helical pitch of p_{tri}(low T) = 66 Å. The lack of significant temperature dependence of the pitch on cooling over the ~20°C temperature range is striking, and in stark contrast to other RSoXS measurements performed on TB dimers and their mixtures [70,111,129,130]. This TB scattering feature fades away as the sample crystallizes near 110°C. We scanned all accessible RSoXS sample-detector configurations to check for other possible resonant scattering signals from q = 0.0012 – 0.10 Å^{-1} (d = ~60 – 5000 Å) but found none. The value of the pitch obtained from RSoXS is in good agreement with our FFTEM measurement of $p_{tri,FFTEM}$ = 66 Å (Figure 4.2.2c, Figure 4.2.3), where we analyzed a number of images to obtain a statistical distribution of the observed periodicities throughout the sample, as described in ref. [129].

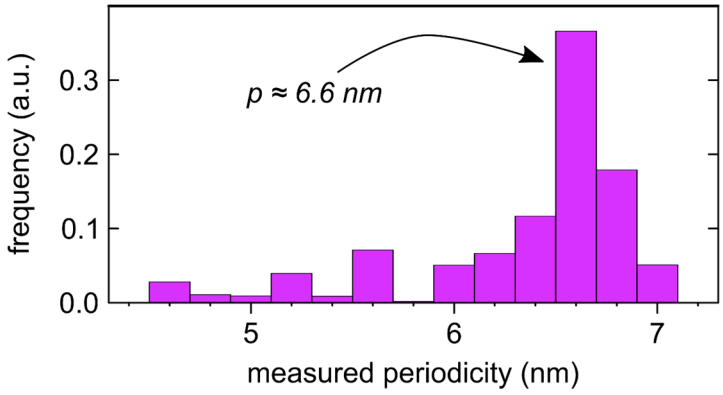

Figure 4.2.3: Histogram of the normalized frequency of observations of topographical modulations in an FFTEM experiment on CB6OBO6CB.
The measured periodicity is weighted by the domain area of observation. The histogram exhibits a peak at $p_{tri,FFTEM}$ = 6.6 nm, demonstrating that this is most likely to be the low-temperature helical pitch exhibited by the TB phase.

Using WAXS, we investigated the diffuse scattering from the trimer corresponding to correlations in mass density along and perpendicular to the TB helix axis. In the TB phase, the scattering feature along the helix axis is present near q_z = 0.48 Å^{-1} (Figure 4.2.4a). This corresponds to d_z = 13 Å, or an intercalation of the trimer over nearly 1/3 of the molecular length. This is in agreement with the significant intercalation reported in previous studies of TB and smectic phases

of LC linear oligomers [95,153,155]. The $q_\perp$ feature corresponds to an average ~5 Å lateral spacing between molecules of CB6OBO6CB.

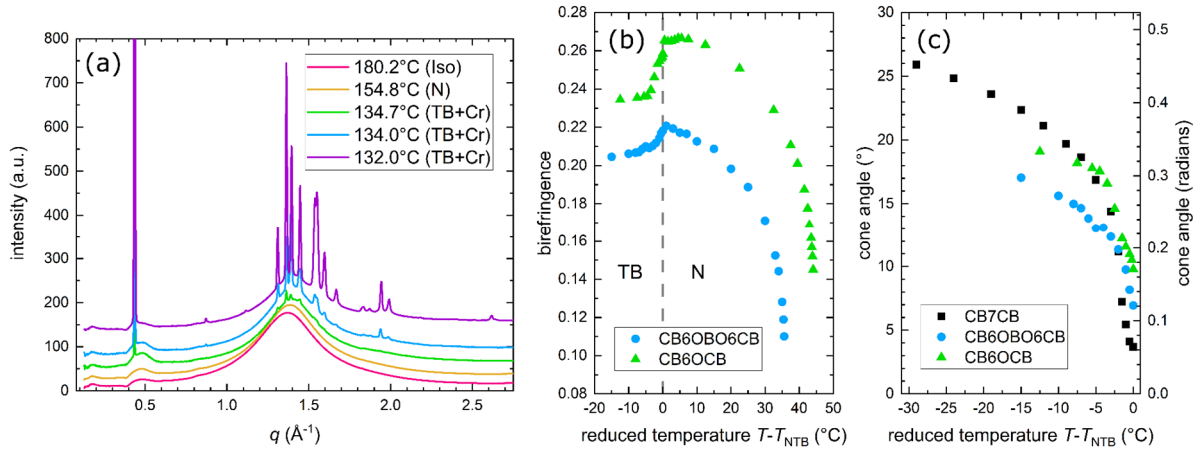

Figure 4.2.4: 1D-WAXS scans of CB6OBO6CB and birefringence and estimated TB cone angle of CB6OCB and CB6OBO6CB.
(a) In the isotropic phase, CB6OBO6CB exhibits diffuse features at $q_z = 0.48$ Å^{-1} and $q_\perp = 1.37$ Å^{-1}. The q_z peak sharpens slightly in the nematic phase, as expected. On further cooling, we capture the TB-Cr coexistence at 134.7°C, with the $q_{z,WAXS}$ feature sharpening up from the nematic phase, but not shifting significantly in q. This feature indicates the presence of a modest density modulation, or pseudo-layering, along the helical direction, with a period of $s_{tri} = 13$ Å. In this experiment, the sample crystallizes very soon after the formation of the monotropic TB phase, with the TB phase and the crystal phase coexisting in the lowest temperature scans. In the crystal phase, a sharp scattering peak appears near the q_z feature, indicating lamellar crystalline ordering. (b) We measured the birefringence of the dimer and trimer using a Berek optical compensator. We then used the procedure developed by Meyer *et al.* [125] to estimate the cone angle $\theta_{optical}$ (c) from the birefringence. For comparison, we include our TB cone angle measurement of CB7CB.

We carried out birefringence measurements of the dimer and trimer (shown in Figure 4.2.4b), then used the procedure developed by Meyer *et al.* [28] to calculate an optically-derived cone angle from the birefringence as a function of temperature (Figure 4.2.4c). The behavior of the optically-derived cone angle in the dimer and trimer is similar to that found for CB7CB. At high temperature in the TB phase, the dimer exhibits a cone angle of ~7°, while the trimer exhibits a cone angle of ~10°. The cone angle saturates near 20° and 17° for the dimer and trimer, respectively, which is somewhat smaller than the value found for CB7CB [129,131].

The striking differences in the nanoscale behavior of the TB phase in the dimer and trimer must be due to effects from the different number of rod-shaped monomer units in the molecules. A number of review studies have discussed the variations in physical and LC properties as a function of the number of monomer units in small LC oligomers [151,153,156–158], but beyond the work in the LC community, the literature on the properties of linear oligomer homologues is sparse. However, we presently have enough experimental detail to construct a model of the TB organization in each material and to address their differences.

The TB nanostructure is determined by a combination of molecular features, including the chemical make-up of the molecules and the relative dimensions of the monomer units, and structural features, including the TB pseudo-layer spacing and helix pitch.

The "pseudo-layer" spacing s in the TB phase is essentially the same feature as that found in aligned nematics, with scattering arcs in q_z elucidating the density modulation along the nematic director $\hat{z}$ [58]. We can determine s for the TB phase from the q_z feature in WAXS experiments for both the dimer [109] and trimer (Figure 4.2.4a), where $s = d(q_z) = 2\pi/q_z$. We find the pseudo-layer spacing for the dimer is s_{di} = 11.6 Å [109] and for the trimer is s_{tri} = 13 Å, as denoted in Figure 4.2.5a,b. That s_{di} and s_{tri} are nearly 1/2 and 1/3 of their respective molecules indicates uniform intercalation of the molecules over their respective s and implies that the TB pseudo-layers are spaced by the height of a single (tilted) alkyl-cyanobiphenyl or alkyl-biphenyl monomer unit making up the dimer or trimer. Interestingly, we find very little or no measurable temperature dependence of s in the nematic and TB phases of the trimer. Likewise, Paterson *et al.* observe no discernible change in the equivalent s_{di} feature in the dimer through the nematic and TB phases [109]. For this reason, in the following analysis we consider s to be constant through the temperature range of the TB phase.

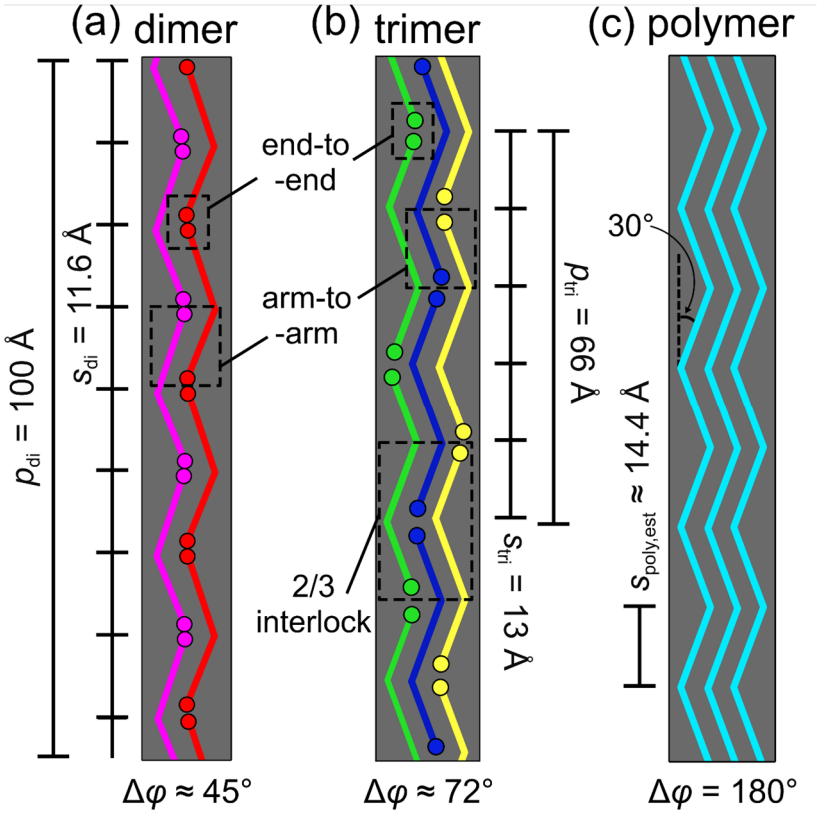

Figure 4.2.5: Stick representations of the (a) CB6OCB dimer, (b) CB6OBO6CB trimer, and (c) the analogous theoretical polymer with corresponding low temperature TB parameters.
The azimuthal precession $\Delta\varphi$ is set to 180° in each case for clarity. The molecules are uniformly intercalated, with the TB chains they form distinguishable and color-coded by the position of the chain-end interfaces. (a, b) The dimer and trimer systems both have end-to-end and arm-to-arm interactions, but only the trimer exhibits an additional 2/3 "interlocked" association (b) which tends to hinder molecular motion and flexibility in the TB helix. (c) The analogous polymer system forms an anticlinic (pseudo-)lamellar phase which is a special case of the TB phase with $\Delta\varphi = 180°$. The polymer molecules are constructed by attaching the ends of many rod-like units that make up the middle-monomer of the trimer (from the central carbon in one linker to the central carbon in the other). The pseudo-layer spacing $s_{poly,est}$ in the analogous polymer is estimated by tilting the middle, rod-like unit of the trimer (16.6 Å) to a 30° angle.

From the values of the pitch p and s, we can determine the azimuthal precession φ per s at low temperature to be $\Delta\varphi_{di} = 360°\times s_{di}/p_{di} = 360°\times$ (11.6Å/100Å) ≈ 42° and $\Delta\varphi_{tri} = 360°\times s_{tri}/p_{tri} =$ 360°×(13Å/66Å) ≈ 71°. For the sake of the geometric modelling that follows, we approximate by letting $\Delta\varphi_{di} \rightarrow 45°$ and $\Delta\varphi_{tri} \rightarrow 72°$. With this, we can construct the TB phase of the dimer as a series of octagons separated by the pseudo-layer spacing s_{di}, with the rod-like arms of the dimer lying along the diagonal of the rectangular faces of the octagonal prism formed by connecting the corners of the octagonal pseudo-layers with straight vertical lines, enforcing the azimuthal rotation

of $\Delta\varphi_{di}$ per s_{di} (Figure 4.2.6a). Similarly, the TB phase of the trimer is modelled as a series of pentagons separated by s_{tri}, with the rod-like monomer units lying on the diagonal of the faces of the pentagonal prism formed, enforcing the azimuthal rotation of $\Delta\varphi_{tri}$ per s_{tri} (Figure 4.2.6b).

We can obtain the TB cone angle θ_{TB} from the optical birefringence measurements of the materials in the nematic and TB phases. On cooling from the nematic phase to the TB phase, we observe a decrease in birefringence, which is due to a collective tilt $\theta_{optical}$ of the molecules from $\hat{z}$ and can be determined by the method of Meyer *et al.* [131]. This measured $\theta_{optical}$ is not, however, the TB cone angle θ_{TB}, as $\theta_{optical}$ measures the tilt of the molecular *plane* of the molecule away from $\hat{z}$, and θ_{TB} is defined by the angle between the helix axis $\hat{z}$ and the local director $\hat{n}$. θ_{TB} comes from a combination of the intrinsic bend angle of the molecule *and* the tilting of the molecules from $\hat{z}$. We can therefore determine θ_{TB} at low temperature using $\theta_{optical}$ and the experimentally determined geometric constrains enforced by the polygonal constructions of Figure 4.2.6a,b. By doing this, we find $\theta_{TB,di} = 21.2°$ ($\theta_{optical,di} \approx 20°$) and $\theta_{TB,tri} = 27.2°$ ($\theta_{optical,tri} \approx 17°$) at low temperature in the TB phase (see Figure 4.2.7).

By solving our geometric constructions of the TB phase, we may also determine the effective monomer length m_{eff} in the TB helix (the length of the diagonal of the rectangular face of the polygonal prisms in Figure 4.2.6a,b). This length may in general be different than the full length of the rod-like monomer unit m_{calc} making up the dimer and trimer, if there is overlap or separation between end groups, for instance. Solving from the geometric constrains in the TB model of the dimer (Figure 4.2.6a), we find $m_{di,eff} = 12.4$ Å. The length of one of the rod-like monomers making up the dimer, as measured in its extended all-*trans* conformation from the central carbon in the linker to the end nitrogen group, is calculated to be $m_{di,calc} = 15.8$ Å. Here, we consider only the extended all-*trans* conformer of the dimer as an approximation to the

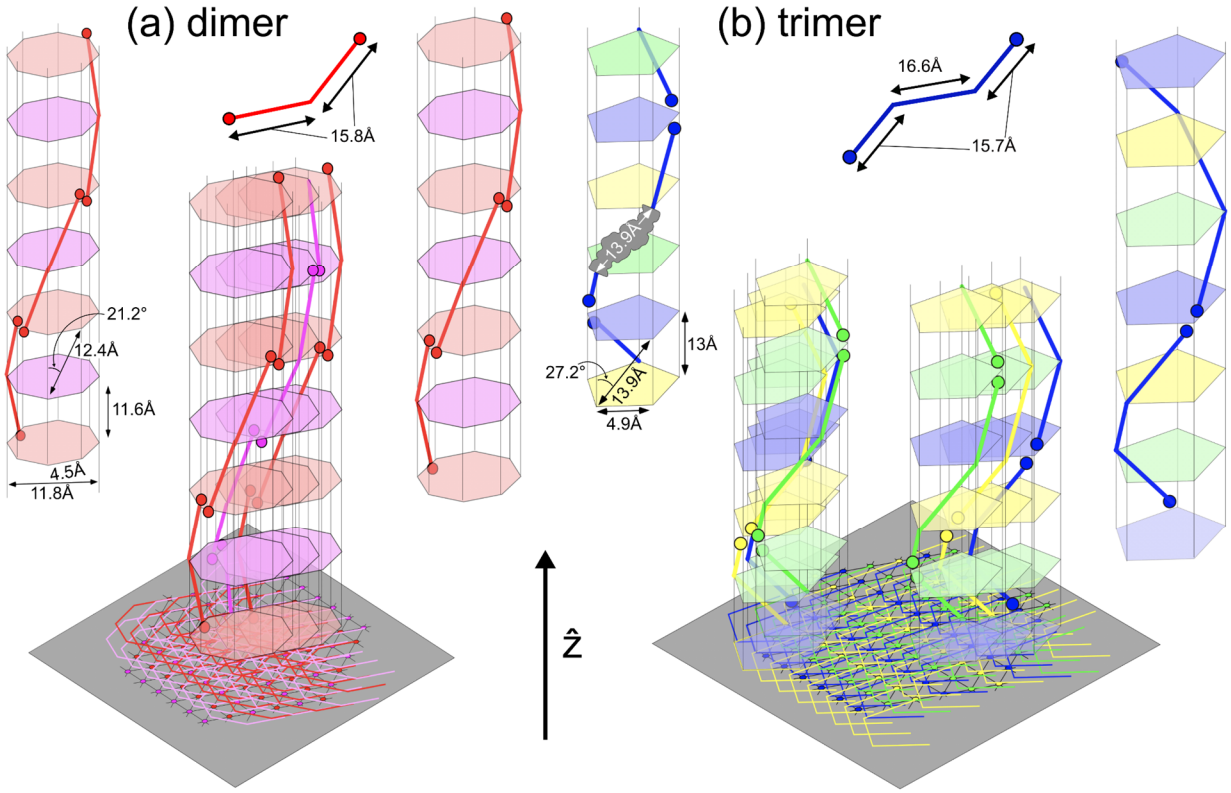

Figure 4.2.6: Geometric models of the CB6OCB dimer and CB6OBO6CB trimer in their respective TB phases.
(a) Geometric construction that governs the structure of the TB phase formed by the dimer at low temperature. The chains are divided into two subsets, with the ends of the red molecules in the chains meeting at the corner of a red octagon, and the ends of the purple molecules meeting at the corner of a purple octagon. The molecular ends in the dimer overlap by 15.8 – 12.4 Å = 3.4 Å, and the rod-like arms are tilted from the helix axis $\hat{z}$ along the diagonal of an outer rectangular face of the octagonal prism by the TB cone angle $\theta_{TB,di}$ = 21.2°. (b) A geometric construction governing the structure of the TB phase formed by the trimer at low temperature. The chains are divided into three subsets with the ends of the blue molecules in the chains meeting at a blue pentagon, and likewise for the green and yellow chains. The chemical make-up of a rod-like middle-monomer is depicted in grey overlaying a middle segment of the blue leftmost trimer chain. The molecular ends of the trimer overlap by 16.0 – 13.9 Å = 2.1 Å (16.0 Å being the averaged monomer length), which is significantly less than that found for the dimer. The rod-like units of the trimer are tilted along the diagonal of the outer face of the pentagonal prism by the cone angle $\theta_{TB,tri}$ = 27.2°. The polygonal prisms in (a) and (b) enforce the respective azimuthal precessions $\Delta\varphi$ per pseudo-layer s. Once the single chains are constructed, they may be rotated around the center line of the polygons to change their helical phase. In this 3D packing sketch, the phase is assumed to be the same for all helices, with the differently colored helices positioned randomly in their packing. We depict a possible 3D packing of the helical chains on a hexagonal lattice in (a) and (b) (grey planes), though the actual packing motif may be different.

conformational diversity expected in the TB phase, since the condensed and locally orientationally aligned TB phase tends to favor extended conformations over more kinked conformers. This indicates an overlapping of the end groups for the dimer of $m_{di,calc} - m_{di,eff}$ = 3.4 Å at low

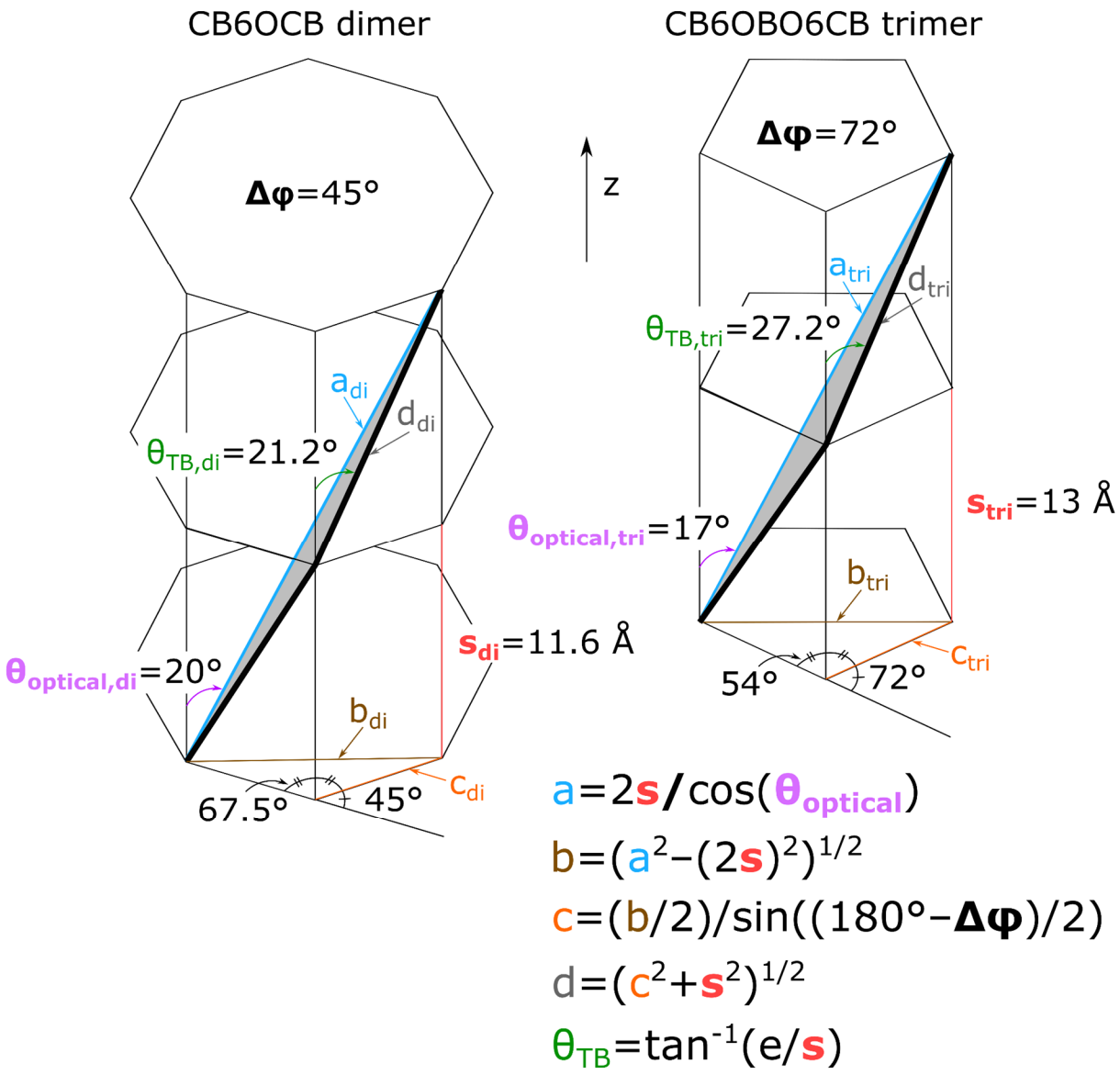

Figure 4.2.7: Determination of the real TB cone angle from measurements of the optical cone angle, pitch, and pseudo-layer spacing.
Derivation of the true TB cone angle θ_{TB} from the at low temperature experimentally obtained geometric parameters: $\theta_{optical}$, s, and $\Delta\varphi$ (in bold in the schematic). $\theta_{optical}$ measures the tilt of the *molecular plane* away from z, whereas θ_{TB} measures the tilt of the *local director* (the direction that a single monomer segment of the molecule points) away from z. These schematics are not to scale.

temperature in the TB phase, or a bit more than the atomic diameter of an end nitrogen. We expect that on heating, in addition to the cone angle decreasing, the ends of the dimers will tend to pull apart, leading to the flexibility in the helix structure and the dramatic pitch increase that we observe at high temperatures in the TB phase (Figure 4.2.2a).

Using a similar treatment for the trimer as for the dimer, we determine the effective monomer length in the TB phase of the trimer to be $m_{tri,eff}$ = 13.9 Å. Because the end- and middle-monomer groups of the trimer are not of equal lengths, we can determine the average monomer length using the Spartan calculation of the extended all-*trans* conformation of the trimer by averaging the lengths of the individual monomer segments. We do this because we only observe a single scattering peak from the pseudo-layer spacing, which implies that the end- and middle-monomer units that make up the trimer are uniformly distributed in space. Here again, we consider the extended all-*trans* conformer of the trimer in our model as an approximation, for the same reasons that we do for the dimer. The length of an end-monomer is measured from the central carbon in a carbon linker to its nearest nitrogen atom, and the length of a middle-monomer is measured from the central carbon of one alkyl linker to the central carbon of the other linker. From this, we find $m_{tri,calc}$ = (2×15.7Å+16.6Å)/3 = 16Å. And now, $m_{tri,calc} - m_{tri,eff}$ = 2.1 Å, indicating a smaller overlap of the molecular ends in the trimer than that found in the dimer. Indeed, the mismatch in the lengths of the end- and middle-monomers of the trimer will tend to pull the shorter end-monomers apart by association with the longer middle-monomers (Figure 4.2.5b). From the above discussion, we can conclude that the molecules in the TB phase of the dimer and the trimer exhibit mutual end group interactions which leads to an effective heliconical chain-like arrangement of the molecules, as depicted in Figure 4.2.6a,b.

Now we turn to the possible intermolecular interactions which occur in the TB phases of the dimer and trimer. In the dimer, there are two kinds of possible associations, given that the molecules are uniformly intercalated over half their length: (1) the ends of different dimers associate, and (2) the molecular arms of different dimers associate (Figure 4.2.5a). Both the end-to-end and the arm-to-arm associations are weak physical connections, as they are only held

together by some combination of van der Waals and electrostatic forces, thereby contributing to flexibility, elasticity, and fluctuations in the structure of the TB helix. This is especially evident at higher temperature in the TB phase, where the pitch varies significantly with temperature in the dimer as we observe.

The trimer system exhibits an additional molecular association which contributes to a more rigid TB helix structure, as evidenced in Figure 4.2.2b. The uniformly intercalated trimers form the TB helix with three distinct molecular associations: (1) the ends of different trimers associate, (2) the end molecular arms of different trimers associate, and (3) 2/3 of neighboring trimer molecules will overlap, or "interlock" together (Figure 4.2.5b). These 2/3 interlocks sterically hinder the motion of the interlocked molecules and their neighbors. This additional interaction is a result of more chemically-bonded monomers per unit length in the TB helix of the trimer than there are in the dimer. For the trimer, at each pseudo-layer interface (any pentagon in Figure 4.2.6b) there are two-thirds chemically bonded monomers (chemically bonded with an alkyl linker) and one-third terminally associated monomers (end-to-end physical association), whereas for the dimer, at each pseudo-layer interface (any octagon in Figure 4.2.6a) there are one-half chemically bonded monomers and one-half terminally associated monomer units. This effect tends to increase the rigidity of the TB helix thereby reducing (and essentially eliminating) the temperature-dependence of the helix pitch in the TB phase of the trimer.

From our experiments, a number of interesting trends in the structure of the TB phase of this oligomeric family emerge. For instance, the pseudo-layer spacing increases from the dimer to the trimer (s_{di} = 11.6 Å; s_{tri} = 13 Å). This trend indicates that s will increase in the higher oligomers, but is not likely to exceed the theoretical pseudo-layer spacing $s_{poly,est} \approx 14.4$ Å of the comparable polymer which is composed of the middle-monomer units of the trimer tilted at a comparable angle

(30°), as depicted in Figure 4.2.5c. This is because the comparable polymer, in the anticlinic (pseudo-) lamellar system, has (effectively) no molecular ends that may overlap, in contrast to the dimer and trimer which have a mixture of inner and terminal connections between rod-shaped elements which do overlap. In addition, the TB pitch tends to decrease from the dimer to the trimer (p_{di}(low T) ≈ 100 Å; p_{tri}(low T) ≈ 66 Å), implying that the pitch will tend to decrease in the higher oligomers in this family and approach a value not smaller than $p_{poly} = 2 \cdot s_{poly,est}$. The pitch will also become more temperature-independent with the increasing number of monomers in the oligomer as the amount of intermolecular locks increases. Additionally, the azimuthal precession $\Delta\varphi$ per s increases from the dimer to the trimer ($\Delta\varphi_{di} \approx 42°$; $\Delta\varphi_{tri} \approx 71°$ at low T). From this observation, we can expect that $\Delta\varphi$ will tend to increase in the longer oligomers of this family, and asymptotically approach a value perhaps not exceeding $\Delta\varphi_{poly} = 180°$, since the comparable polymer in an anticlinic (pseudo-)lamellar phase, has p_{poly} and s_{poly}, (and therefore $\Delta\varphi_{poly}$), fixed by the chemical structure. Our investigation of this dimer and trimer outlines the possible trends in their oligomeric family and for other linear main-chain oligomeric series with similar molecular constructions. It is important to stress, however, that the behavior of the TB nanostructure of different oligomer families may depend qualitatively on the chemical structure of those oligomers, as well as on the number of monomer segments, their relative dimensions, and preferred orientations. Clearly, it is of great interest to explore the features of the TB nanostructure more systematically as a function of these variables.

Finally, we evaluate the possible 3D packing motifs of the heliconical chains formed from the dimer and trimer. Consider the hexagonal lattice represented in the grey shaded planes in Figure 4.2.6a,b. Each site on this lattice has a heliconical chain passing through it, and the constructions in Figure 4.2.6a,b result if we assume that all the chains pass through the plane with the same

helical phase φ. The assumption that all the chains have the same phase is motivated by the x-ray diffraction crystal structures of Hori *et al.* [159] for their dimer material II-3, which exhibits a helical state in its crystal phase with an azimuthal rotation of $\Delta\varphi_{\text{II-3}} = 90°$ per layer, with a layer spacing of $s_{\text{II-3}} = 9.7$ Å, a tilt of the mesogenic cores of $\theta_{\text{II-3}} = 45°$ relative to the helix axis, and a pitch of $p_{\text{II-3}} = 38.7$ Å. The crystal structure of II-3 is similar to that sketched for the TB phase of the trimer in Figure 4.2.6b, but with II-3 having its helical chains on squares rather than on pentagons and tiling a square lattice to fill 3D space. In this crystal structure, the helical phase φ in a given plane normal to the helix axis is the same for all the chains, a geometrical consequence of the large monomer tilt of II-3 and the steric constraints of packing the rod-shaped units with a large tilt. The large inherent tilt of the rod-like monomer units in the dimer and trimer makes it likely that their helical chains are likewise precessing in phase with one another, as depicted in Figure 4.2.6a,b. Though we find that this evidence points to the organization depicted in Figure 4.2.6a,b, it is possible that the helical chains are instead randomly spatially arranged or arranged in more complex fashions, though we cannot speak to these organizational motifs in the present study.

Recently, Al-Janabi *et al*. published an investigation of the phase behavior of the trimer that we study here [120]. A comparison of our data for our trimer and theirs (which they call $B6_3$) show that their differential scanning calorimetry measurements, phase diagram, and non-resonant x-ray scattering features are nearly the same as ours. The only difference appears to be that they obtained different optical textures than expected for a TB phase. On this basis, and the lack of miscibility between their trimer and another material with a TB phase, they chose not to identify the lower temperature nematic phase as a TB phase. However, as we report, our RSoXS experiments demonstrate an orientation modulation at 66 Å only near the carbon K-edge

resonance, and not off the energy resonance. The TB phase is the only known LC phase in this range of length-scales that exhibits resonant scattering for the helix pitch and the absence of scattering in non-resonant conditions. The likelihood of having a splay-bend nematic or similar modulated nematic with a non-zero density modulation, but lacking a non-resonant scattering signal is too remote to consider and has already been discussed in detail in ref. [70]. In addition to this evidence, our polarized light microscopy images are decidedly typical of the TB phase, exhibiting the characteristic blocky and rope textures in a unidirectionally rubbed cell, textures that have been used by many research groups to identify the TB phase. And finally, a contact cell preparation with the trimer and the well-known TB-forming material CB7CB clearly demonstrates miscibility of these compounds in the nematic and TB phases. It is with this evidence that we confidently identify the lower-temperature nematic phase of CB6OBO6CB as the TB phase.

In summary, we synthesized and characterized the TB-forming LC trimer CB6OBO6CB and its analogous dimer CB6OCB. The trimer exhibits a monotropic TB phase with a temperature-independent heliconical pitch p_{tri} = 67 – 66 Å, the smallest yet reported in the literature. Our characterization of these materials suggests the importance of the number of chemically linked segments in a molecule for controlling the elasticity and fluctuations in the TB nanostructure. We constructed a geometric picture of the TB phase for the dimer and trimer which indicates that they are formed by a helical chain motif which is linked together by an association and overlapping of the molecular ends. The nanoscale properties of their TB phases differ significantly because the trimer exhibits an additional molecular association over 2/3 of its length which does not exist in the dimer. This work evokes the possibility for designing LCs which exhibit a specific, temperature-independent TB pitch for technological applications in which a fixed pitch over a

wide temperature range is preferred, such as nano-templating or chiral separation techniques. It also opens up a rich phase space of possible molecular designs motifs for the TB phase by not only varying the chemical make-ups and number of monomer units, but by also varying the relative physical dimensions and orientations of the monomers in the oligomer, likely yielding further, untold exciting material properties.

4.3. MIXTURES OF CB7CB WITH 5CB AND THE DUPLEX HELICAL CHAIN MODEL

Here, we characterize the structure of the ground state of the TB phase of the bent dimer CB7CB and its mixtures with 5CB over a wide range of concentrations and temperatures using a variety of experimental techniques and atomistic simulations. We show that the contour length along the molecular direction for a single turn of the helix is approximately equal to $2\pi R_{mol}$, where R_{mol} is the estimated radius of bend curvature of a single all-*trans* CB7CB molecule. This relation emerges from a model which relates the macroscopic characteristics of the helical structure to the bent molecular shape. This connection comes about through the presence in the fluid of self-assembled, oligomer-like correlations of interlocking molecules, arising from the nanosegregation of rigid and flexible molecular subcomponents, forming a brickwork tiling of pairs of molecular strands into a duplex helical chain [129].

An important theme in soft materials and LC science is to understand the interplay between molecular shape and macroscopic self-organization and create new motifs of ordering based on the exploration of different molecular shapes. A prime example of such a scenario is the discovery of the spontaneous formation of chiral ordering in fluids (Pasteur's experiment, in fluids), as evidenced by macroscopic chiral conglomerate domains in LCs of achiral bent molecules [51,160]. In these fluid lamellar smectic phases, the confinement of the molecules to layers forces their steric bends to be in a common, in-layer direction, giving long-ranged polar ordering, and the steric ordering of molecular tilt gives macroscopic chirality [49,50]. Diverse motifs of frustrated packing of achiral molecules in these materials lead to chiral isotropic

liquids [161], chiral, fluid, three-dimensional (3D) crystals [162], columnar phases [54,163], helical nanofilament phases [53], and chiral sponge phases [52].

The most recent, and perhaps most exotic, manifestation of spontaneous chirality in a fluid of achiral molecules is the TB phase of CB7CB (Figure 3.2.3), which fills 3D space with a long-range ordered 1D heliconical precession of pure molecular orientation. A remarkable feature of the TB phase is its very short pitch, on the order of four molecular lengths in CB7CB. In typical nematic LC phases, even strongly chiral ones, neighboring molecules differ in orientation by only a few degrees at most. Known LC phases with larger orientational jumps have positional ordering into 1D lamellar, 2D columnar, or 3D crystalline phases. How the TB phase remains a fully 3D liquid in the presence of such strong coherent internal orientational ordering is a key open question.

In order to explore this issue, here we carry out resonant soft x-ray scattering (RSoXS) and birefringence experiments, measuring the helix pitch and cone angle in a series of CB7CB mixtures with the nematic LC 5CB, and determining the ground state helix structures of their TB phases. The resulting TB helix geometries point to the association of molecules into duplex molecular chains driven by steric self-assembly. This indicates a remarkable new mode of soft matter organization, oligomerization that is driven principally by steric self-assembly and a remarkable inherent geometric relationship between the macroscopic helix and the bend curvature of the CB7CB molecule B_{mol}: (**i**) In the TB phase, twist and bend deformations of the orientation field of the molecular long axis (the director field) are much smaller than B_{mol}. The structure is principally a twist of biaxial molecular ordering about the long axes, the pitch of which is comparable to $2\pi/B_{mol}$, quantitatively relatable to the molecular bend curvature, in spite of the near absence of macroscopic director bend; (**ii**) The contour length along the molecular long axis direction for a single turn of the helix is the same for all concentrations and temperatures, implying transient

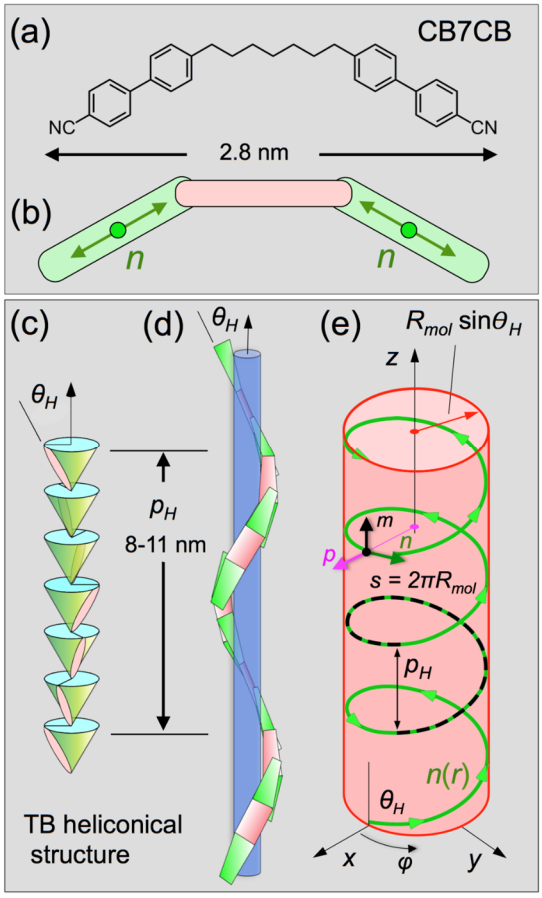

Figure 4.3.1: CB7CB and drawing of the TB phase. (a) Chemical structure of CB7CB. (b) Bent-rod representation of CB7CB, showing its two contributions to the director field, the unit vector n. Schematic of the chiral smectic C phase and (c) the TB phase, showing the precession of the director orientation on a cone of angle θ_H, taken for here to be the tilt of a principal axis of the dielectric tensor. (d) Helical winding of the director in the TB phase. At each level, the indicated orientations fill the x-y plane. (e) Geometry of the helical path of the contour line that locally follows the orientation of $n(r)$. The distance along the contour is $s(\varphi)$. A physical constraint of the TB structure in CB7CB, first reported in this paper, is that the cylinder radius varies with cone angle θ_H as sin θ_H, such that the length of the contour $s(2\pi)$ for one pitch of the helix (dashed black line) is independent of θ_H and always given by $s(2\pi) = 2\pi R_{mol}$, where R_{mol} is the bend radius of curvature of an extended CB7CB molecule.

association of molecules into oligomer-like chains; (**iii**) The oligomers are linear molecular chains of one helicity that combine to form a duplex helical, brickwork-like, tiled chain of the opposite handedness; (**iv**) The duplex chains behave in turn as helical steric objects which pack to form the 3D phase, thereby hierarchically self-assembling into the heliconical structure [136,164]. This model reveals a mystery of the microscopic drive of such ordering not captured by continuum elastic theories, which is driven by the reduced bend modulus.

In the conventional nematic (N) LC phase, the ground state is a three-dimensional (3D) fluid of uniform density , with an orientation field of molecular rods in which the local average molecular long axis orientation, the director field, $\boldsymbol{n}(\boldsymbol{r})$, is the same everywhere [17]. The TB phase is also a 3D fluid of uniform density but composed of bent molecules which self-assemble into a chiral, heliconical ground state, with a helical precession of $\boldsymbol{n}(z)$ in azimuthal orientation $\varphi(z)$ on a

cone of angle θ_H; the helix (H) is coaxial with an axis $\boldsymbol{z}$ and has a pitch of ~10-nanometer scale [59,70,85]. This chiral structure forms by a symmetry-breaking transition from the uniaxial nematic, even though the molecules are structurally achiral. The resulting heliconical director field has bend and twist elastic deformations, B_H and T_H respectively, of $\boldsymbol{n}(z)$ that are nonzero and of uniform magnitude everywhere in space (Figure 4.3.1, [75]). Resonant soft x-ray scattering (RSoXS), by virtue of its sensitivity to molecular orientation, has enabled observation of scattering from this TB helix in the bent molecular dimer CB7CB, where the magnitude of the wavevector of the diffraction peak, $|\boldsymbol{q}| = q_H$, is a direct measure of the pitch of the TB helix, $p_H = 2\pi/q_H$ [70,111]. The combination of q_H data with measurements of the average heliconical cone angle θ_H suffices to determine the essential mean geometry of the TB helix, including the magnitude of the director bend B_H. This analysis reveals a remarkable relation between the director bend and the TB cone angle which is universal both as a function of temperature and mixture concentration of 5CB. As we decrease the temperature from the nematic to the TB phase, the pitch becomes shorter and the cone angle increases. However, they do so in such a way that $q_H\cos\theta$ is fixed, a remarkable behavior.

The phase behavior of binary mixtures of CB7CB and 5CB was characterized as a function of weight percent 5CB, x, in the range $12.5 < x < 95$ using differential scanning calorimetry, generating the phase diagram of Figure 4.3.2. The N – TB phase transition was probed using polarized light microscopy (PLM) of the various mixtures in untreated and planar cells for x up to 62.5 (Figure 4.3.3). In the mixtures with $x \leq 25$, the TB phase exhibits the typical stripe texture on cooling, which was shown to be due to a spontaneous undulation with displacement along z of the planes of constant azimuthal orientation φ [89], caused by dilative stress on the helical structure due to the shrinking of p_H on cooling [70]. For $x \geq 37.5$, we found that the stripes form briefly on cooling with the texture flickering rapidly, finally relaxing into a state of uniform birefringence, indicating that the addition of 5CB tends to fluidize the TB phase and enhance

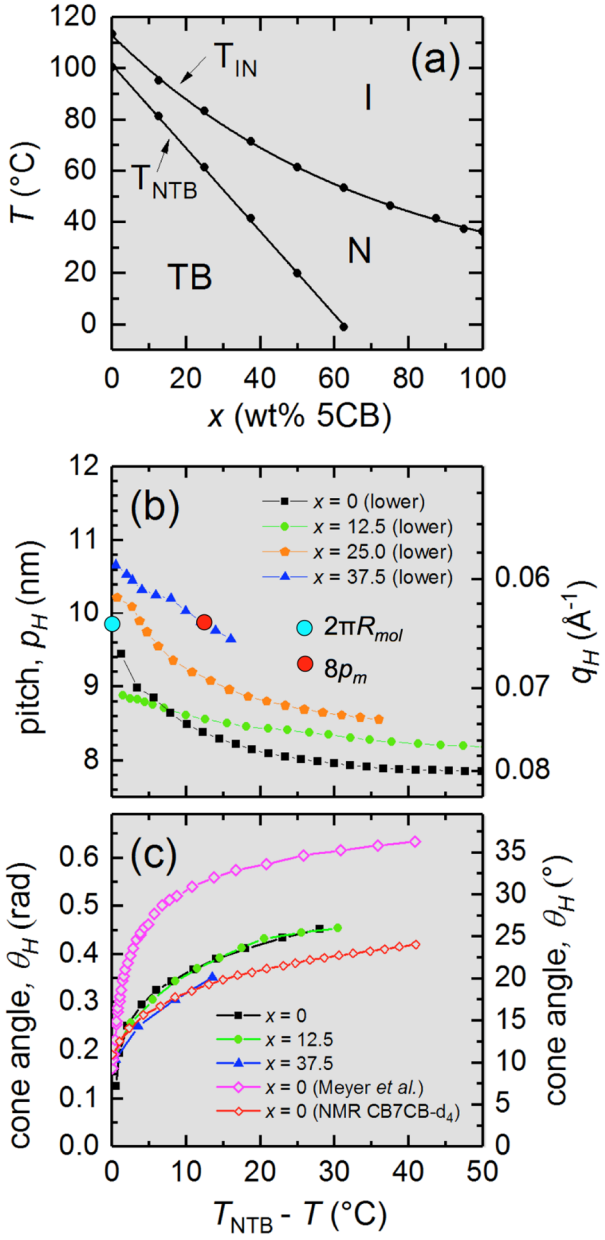

Figure 4.3.2: Experimental characterization of the binary phase diagram (a), TB pitch (b), and estimated cone angle (c) of CB7CB and its mixtures with 5CB.
(a) Phase diagram of the CB7CB/5CB mixtures vs. weight %, x, and temperature, T, exhibiting isotropic (I), nematic (N), and TB (TB) phases. (b,c) Helix pitch, p_H , obtained by resonant soft x-ray scattering (RSoXS), and optical cone angle, θ_H, determined from birefringence measurements, of the heliconical structure in the TB phase vs. x and $T_{NTB} - T$, where T_{NTB} is the N – TB phase transition temperature. Birefringence [131] and NMR [133] data from literature sources are also included. In CB7CB, the helix pitch near the transition is found to be $p_H \approx 2\pi R_{mol}$ (blue dot in (b)) where R_{mol} is the bend radius of curvature of an extended CB7CB molecule. Diffuse, non-resonant x-ray scattering indicates periodic segmentation along the helix of spacing $p_m \approx 1.25$ nm. The pitch near the transition has eight such segments (red dot in (b)).

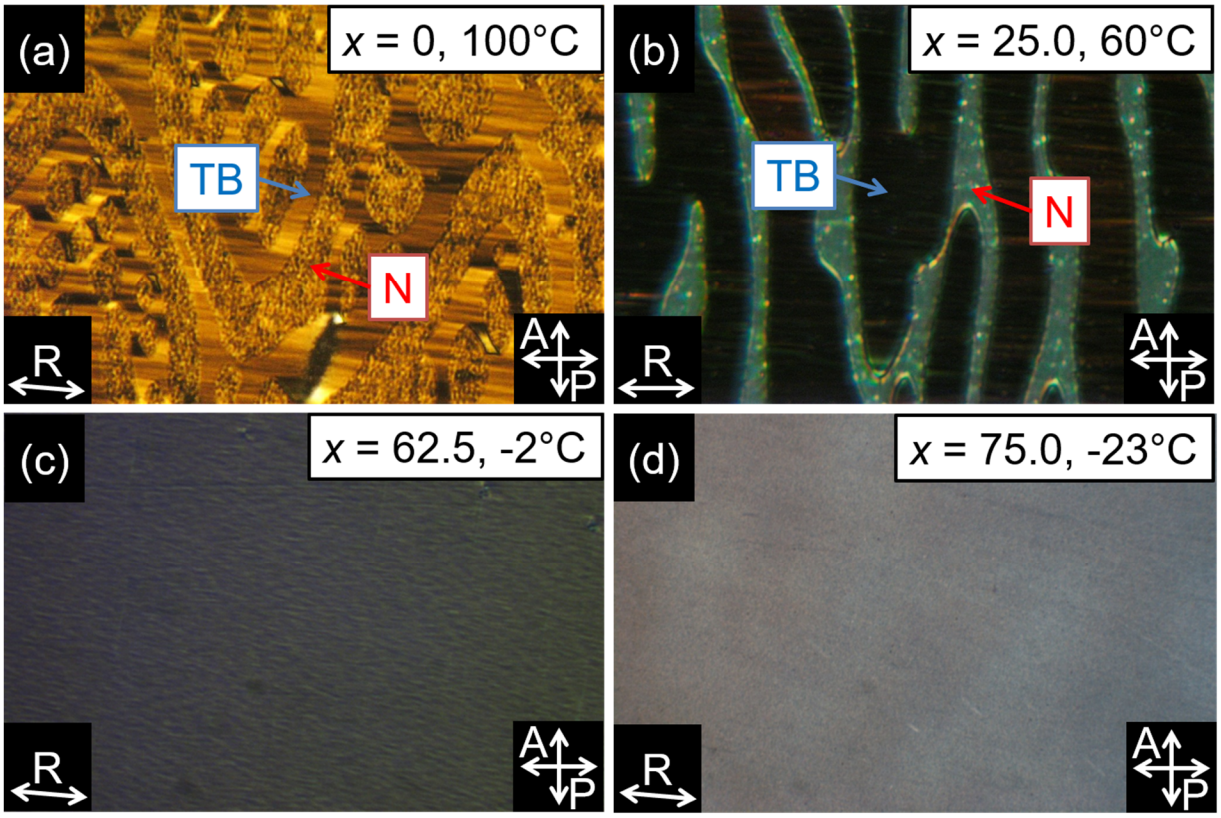

Figure 4.3.3: Optical textures of neat CB7CB and 5CB/CB7CB mixtures.
The mixtures are in unidirectionally rubbed cells with rubbing direction R. They are imaged just below the N – TB transition temperature. In (a) $x = 0$ and (b) $x = 25.0$, we see N – TB phase coexistence when the samples are cooled slowly from the nematic, confirming the first order nature of the N – TB phase transition in these samples. As we increase the 5CB concentration, the temperature ranges over which we observe phase coexistence becomes narrower. In the (c) $x = 50.0$ and (d) $x = 62.5$ mixtures, a very weak stripe texture appears when cooled several degrees below the N – TB transition, with no observable phase coexistence.

fluctuations so that it can anneal into an undulation-free director field configuration [87]. This demonstrates the utility of making mixtures of 5CB with CB7CB to obtain a uniform and undulation-free, well-aligned TB phase. The isotropic (I) to nematic (N) transition temperature of the mixtures, $T_{IN,}$ decreases monotonically as x increases, while the N–TB phase transition temperature, $T_{TB,}$ decreases nearly linearly with the addition of 5CB until it becomes undetectable for $x > 62.5$. These behaviors are similar to those in mixtures of CB9CB/5CB [99] and CB7CB/7OCB [165].

Resonant soft x-ray scattering (RSoXS) was used to provide a direct *in situ* measurement of the bulk heliconical nematic structure in the mixtures [70], exhibiting diffraction arcs from periodicities in the 8–11 nm range in the TB phase. Extensive freeze-fracture TEM study, shows the helix pitch p_H, the distance along z for a 2π circuit of the helix, to also be in the 8–11 nm range [59]. This, and the discussion below, leads us to assign the RSoXS diffraction to be from the fundamental periodicity of the helix, *i.e.*, with the $q_H = 2\pi/p_H$. In the mixtures, the diffraction arcs are smooth and have relatively narrow width in wavevector q at low temperature, as in CB7CB [70], indicating that the pitch is homogenous throughout the sample. As the temperature is raised, the scattering tends evolve in q into a distribution of individual arcs of differing q_H, including some with linewidths comparable to 0.0002 $Å^{-1}$, the wavevector resolution of the diffractometer [70]. This behavior suggests the development of domains in the sample having a distribution of values of average heliconical pitch. Studies in detail in neat CB7CB [70] showed that the same lower limit of the pitch in the distributions was obtained repeatably but that the upper limit varied erratically from scan to scan in T, indicating that the TB helix pitch is much softer in response to stretching than to compression, and that the stretching is due to nonuniform stress distributions that develop in the macroscopic textures of the helix axis. For this reason, p_H is taken to be that from the lowest-q half-height value of each of the distributions. The resulting p_H data are plotted vs. $T_{TB} - T$ in Figure 4.3.3b. If the temperature of the TB phase of the $x = 0$ and 12.5 mixtures is increased toward T_{TB}, a coexistence range of T is entered in which some of the TB domains melt. This causes the p_H distribution to narrow at the highest temperatures in the TB phase, the upper limits approaching the lower. However, the $x = 25$ and 37.5 mixtures do not exhibit this behavior: the pitch range remains large near the transition, indicating that the

coexistence range is narrower at higher 5CB concentrations, which is also what we observe by PLM.

The optical cone angle of the TB helix, θ_H, was determined for the mixtures from measurements of the birefringence, Δn, of the N and TB phases, as detailed in [129,131]. Values of θ_H obtained from birefringence [131] and NMR experiments [133] are also available for neat CB7CB. The θ_H data are plotted vs. $T_{TB} - T$ in Figure 4.3.3c. The data show that Δn increases continuously with decreasing T in the N phase, and then near the N–TB transition abruptly begins to decrease. We take this change to indicate the onset of the collective heliconical ordering in the TB phase. The N phase birefringence is somewhat smaller than that of pure 5CB, which we take to indicate the degree of tilt of the cyanobiphenyl groups in CB7CB away from the average orientation in the N phase, which is substantial: ~ 30°. The heliconical ordering then further reduces Δn in the TB phase.

If the TB phase heliconical ground state axis is taken to be along z, then $\boldsymbol{n}(\boldsymbol{r})$, may be written as $\hat{\boldsymbol{n}}(z) = (\hat{\boldsymbol{x}}\sin\theta_H\cos\varphi + \hat{\boldsymbol{y}}\sin\theta_H\sin\varphi + \hat{\boldsymbol{z}}\cos\theta_H)$, where $\varphi(z)$ is the azimuthal angle, given by $\varphi(z) = q_H z = (2\pi/p_H)z$, as sketched in Figure 4.3.1c-f. The heliconical structure can be represented as rotation on a cone as in Figure 4.3.1c or by the green director contour lines in Figure 4.3.1e and f, representing the path (contour line) along which the incremental displacement is always along $\boldsymbol{n}(z)$. The local nematic order tensor is biaxial, with principal axes given by the director ($\boldsymbol{n}$), polarization ($\boldsymbol{p}$), and auxiliary ($\boldsymbol{m}$) unit vectors. We begin by considering the bend deformation of $\boldsymbol{n}$, given generally by the director rotation vector $\boldsymbol{B}_n(\boldsymbol{r}) = \boldsymbol{n}(\boldsymbol{r}) \times [\partial\boldsymbol{n}(\boldsymbol{r})/\partial s]$, where s is the displacement along the contour. Since by definition of the pitch we have $q_H \equiv \mathrm{d}\varphi/\mathrm{d}z$, and from the geometry of the helix in Figure 4.3.1f, $\cos\theta_H = \mathrm{d}z/\mathrm{d}s$, we find $\mathrm{d}\varphi/\mathrm{d}s = q_H\cos\theta_H$. According to Figure 4.3.1f, then, the magnitude of the bend of $\boldsymbol{n}(z)$ in the helix is $B_H = B_n(\theta_H) = (q_H\cos\theta_H)\sin\theta_H$.

B_H values calculated using this result are plotted in Figure 4.3.4 vs. $\sin\theta_H$ for the q_H and θ_H data of Figure 4.3.2. The B_H values fall quite closely onto a straight line passing through the (B_H, $\sin\theta_H$) origin, indicating that changing T or 5CB concentration x just moves points along the line, a quite surprising result that enables an immediate prediction: if $B_H(\sin\theta_H)$ is indeed linear in $\sin\theta_H$, then we must have $q_H(\theta_H)\cos\theta_H = S$, the (constant) slope of "the line". At high temperatures in the TB phase where θ_H is approaching zero, $\cos\theta_H \approx 1$ and therefore $q_H = S$. Thus, for data on the line, the slope of the line should give the limiting helix pitch near the N – TB transition as $p_{Hlim} = 2\pi/S$. Fitting the B_H data in Figure 4.3.4 to a line through the origin yields $S = 0.64$ nm^{-1} and therefore $p_{Hlim} = 9.8$ nm. This value is plotted as the yellow dot in Figure 4.3.4 and is indeed close to the measured pitches at high T in the TB phase, deviating from the maximum pitches of the different mixtures by less than 10%, characteristic of the deviation of the $B_H(\theta_H)$ data from the fitted line, which has p_H increasing weakly with increasing 5CB concentration.

The observation that $q_H\cos\theta_H$ is nearly constant leads immediately to the question of how to interpret this fitted value of S. That $B_H = S\sin\theta_H$ means that $S = B(90^o)$, the maximum achievable value of bend of $\boldsymbol{n}(z)$, obtained when θ is extrapolated to 90º. However, in the helix we also have director twist, $T_H(\theta_H) = q_H\cos^2\theta_H$, which, if $q_H\cos\theta_H = S$, is given by $T_H(\theta_H) = S\sin\theta_H\tan\theta_H$ for the magnitude of the twist deformation, meaning that the twist elastic energy density $U_T = K_T T_H^2/2$

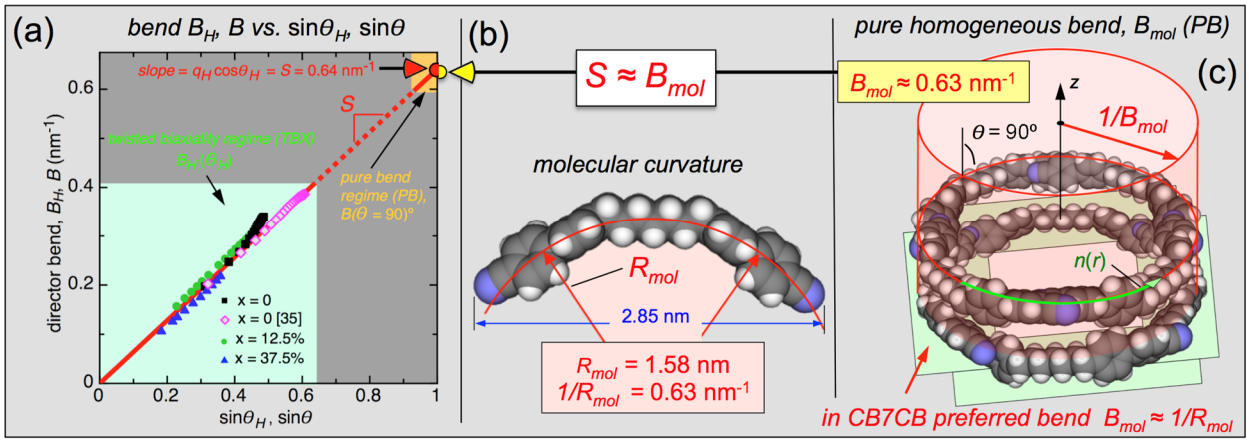

Figure 4.3.4: The link between molecular bend and director bend in the TB phase.
(a) Director bend deformation magnitude $B_H(\theta_H) = (q_H\cos\theta_H)sin\theta_H$ calculated from the q_H and θ_H data of Fig. 2. The $\sin\theta_H$ axis is given in units of sin. The measured bend values lie closely to a straight line through the origin, indicating that $q_H\cos\theta_H = S = 0.64$ nm^{-1}. Changing x or T just moves the points along "the line". (b) The $B_H(\theta_H)$ data of (a) can be related to the molecular shape of CB7CB by noticing that S is nearly equal to its inverse molecular radius of (bend) curvature $1/R_{mol}$ obtained by fitting atomic centers to a circle. This suggests that the extrapolation to $\theta = 90°$ describes the state of maximum intrinsic bend, obtained by putting the molecules into the state of pure homogeneous bend (PB) as in (c), in a brickwork packing motif, while energetically pinning them to a cylinder of variable radius on which they can seek their intrinsic bend curvature B_{mol}. For CB7CB, which has a bent shape that fits neatly onto a circle, $B_{mol} \approx 1/R_{mol}$ and the pitch measurements of (a) are described by $B_H = B_{mol}sin\theta_H$. This relation elegantly connects macroscopic helix characteristics at small θ_H, where the TB structure is dominated by biaxial twist and has little bend, to the bent molecular shape.

grows strongly with increasing θ_H, effectively setting an upper limit of $\theta_{Hmax} \lesssim 35°$ on the achievable range of θ_H, and making the limit $\theta_H \to 90°$ nonphysical for the TB helix.

Pure Bend (PB) Regime – We propose alternatively that the extrapolation of $B(\theta)$ to $\theta = 90°$ represents a completely different physical situation, the one exhibiting the maximum preferred bend of $\boldsymbol{n}(z)$. This requires a geometry: (**i**) in which there is only director bend (pure bend (PB)), (**ii**) in which this bend has its preferred value everywhere (constant magnitude of director bend), and (**iii**) in which $\theta = 90°$, that is $\boldsymbol{n} \perp z$. These conditions are uniquely realized in the geometry of Figure 4.3.4c, in the system of CB7CB molecules in which their atoms are attracted to a cylindrical surface of variable radius, packed, and equilibrated. At low temperature, this condition maximizes the number density, a condition explored by packing DFT-based (DFT/B3LYP/6-31G**) space-filling models of rigid all-trans CB7CB. Maximum density in a geometry of pure bend is achieved

when the molecules are arranged with $\boldsymbol{B}(\boldsymbol{r})$ and $\boldsymbol{n}(\boldsymbol{r})$ parallel to the *x*-*y* plane ($\theta = 90^{o}$), on a cylinder of preferred radius, $1/B_{mol}$. Since the shape of an extended CB7CB molecule matches a circle reasonably well, the preferred PB radius can be estimated from the construction shown in Figure 4.3.4b, which minimizes mean square atomic distance from a circle by varying the circle radius R_{mol}. That is to say, for CB7CB we take the preferred bend B_{mol} in Figure 4.3.4c to be the inverse of R_{mol} from Figure 4.3.4b. The resulting effective molecular radius of curvature of CB7CB is found to be $R_{mol} = 1.58$ nm. This corresponds to a molecular bend of $B = 1/R_{mol} = 0.63$ nm^{-1}, which is remarkably close to the slope $S = 0.64$ nm^{-1}, independently derived in Figure 4.3.4a from the θ_H, p_H data. These data are plotted in Figure 4.3.4a, with S as the red half dot and B_{mol} as the yellow half dot at $\theta = 90^{o}$, where $B(\theta)$ extrapolates to S.

We thus find, remarkably, that the B_H vs. $\sin\theta_H$ trajectory of the data in Figure 4.3.4 apparently could have been predicted from the molecular quantity R_{mol}, even at small θ_H where there is little director bend left in the structure, and, furthermore, that the limiting pitch at the N – TB transition can be given in terms of the molecular quantities as $p_{Hlim} = 2\pi/S = 2\pi/B_{mol} = 2\pi R_{mol}$ = 9.8 nm. That is, if the TB system B_H vs. $\sin\theta_H$ trajectory has slope B_{mol}, meaning that $q_H \cos\theta_H = B_{mol}$, then the helix pitch at $\theta_H = 0^{o}$ is just the circumference of the circle in Figure 4.3.4b and c, describing the molecular radius of bend curvature, R_{mol}. This circumference accommodates about four CB7CB molecules of all-*trans* length (~2.6 nm) with a slight overlap of the CN groups (Figure 4.3.4c).

Thus, if the rationale for the TB phenomenon is based on effects of molecular bend, then this observation suggests that the $q_H(\theta_H)$ data respond to changes of temperature and concentration by moving on the trajectory $B_H \approx S\sin\theta_H$, which is in turn being controlled through S by molecular bend by way of R_{mol}, even at small θ_H. This result is also surprising because, for TB phases and

especially near the N – TB transition where θ_H tends to be the smallest, there is little director bend left in the structure, the bend magnitude $B_H(\theta_H)$ getting quite small, as shown in Figure 4.3.4. Nevertheless, if the data are on the line, bend is still proportional to B_{mol}. Thus, the data of Figure 4.3.4 indicate that the structural preference for the TB ordering to give a well-defined q_H is definitely not a preference for constant bend. Several studies analyzing the elasticity of the TB helix pitch have recently found the director curvature bend energy to be orders of magnitude too weak to account for the TB pitch compressional elastic constant, C, measured as θ_H becomes small, and were led to propose local lamellar smectic positional correlations as an alternate source of rigidity [93,147]. Figure 4.3.4 shows, however, since the data are nearly on "the line", that the helix pitch appears to be controlled by molecular bend, even in the absence of director bend at small θ_H.

Polygon Chain Model – These considerations lead next to the question of the geometrical meaning of the line and, in particular, the relationship $d\varphi/ds = q_H \cos\theta_H = B_{mol}$. Thus, on the line, for different values of θ_H, q_H is such that $s(\Delta\varphi = 2\pi)$, the net distance traveled along the director contour path for a 2π increase in φ (one complete turn of the helix, shown as the black dashed line in Figure 4.3.1e), is independent of θ_H, and furthermore given by $s(\Delta\varphi = 2\pi) = 2\pi/B_{mol} = 2\pi R_{mol}$ for all θ_H, including the PB regime $\theta = 90^\circ$ (the path through $\Delta\varphi = 2\pi$ around the circle of circumference $2\pi R_{mol}$). The equality $s(\Delta\varphi = 2\pi) = 2\pi R_{mol}$ does not appear to be a symmetry of the system, because the TB ground state at small θ_H is entirely different from that of the PB at $\theta = 90^\circ$. However, this is clearly the condition that connects the two regimes.

We can shed light on this condition by developing a geometrical model, the rectangle-triangle (RT) polygon chain, sketched in Figure 4.3.5, that, by design, exhibits $s(\Delta\varphi = 2\pi) = 2\pi R_{mol}$ over the entire range of θ_H. This model is an assembly of rectangular and triangular plates,

connected into a periodic chain where the lines representing shared edges of rectangles and triangles are bendable hinges. The rectangles are attached to, and constrained to be locally parallel to, a flexible rod in the form of a helical spring representing the contour line of the director (green lines, Figure 4.3.1e,f and Figure 4.3.5b), on a cylinder of tunable radius $R = R_{mol}\sin\theta_H$. The corresponding tunable pitch $p_H = 2\pi R_{mol}/\cos\theta_H$ guarantees that such a chain of length $s(\Delta\varphi = 2\pi) = 2\pi R_{mol}$, in this case this length of its eight rectangles, $8L$, always makes exactly one turn of the helix. The rod is inextensible, enforcing by construction the condition that $s(\Delta\varphi = 2\pi) = 2\pi R_{mol}$. In the basic structural unit of the chain, consisting of two rectangles and a 45º isosceles triangle, a 45º bend in the director is enforced by the triangular hinge when the triangle and rectangles are all in the same plane, the condition at $\theta = 90º$ where the whole construction lies parallel to the *x*-*y* plane (Figure 4.3.5b). This directly models the molecular organization of the PB limit in the cylindrical shell packing of Figure 4.3.4c.

The hinge angle $\beta_o = 45º = 360º/8$ was chosen because, as discussed below, a diffuse feature in the non-resonant x-ray scattering indicates that that there are ~8 molecular half-lengths in the TB pitch at small θ_H. Since the data are on "the line" there must correspondingly be in the pure

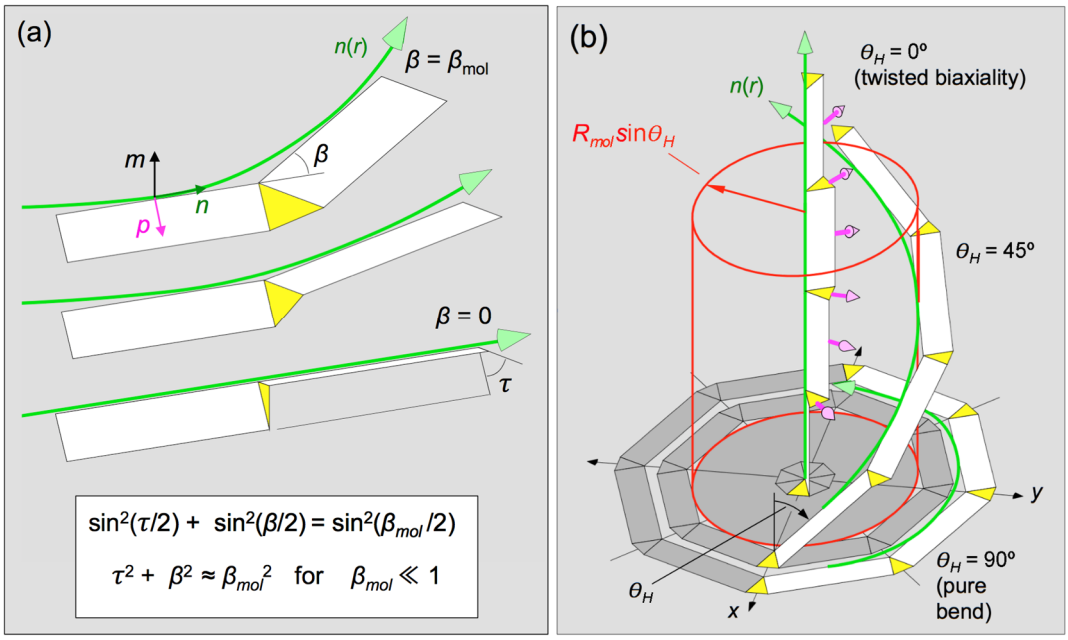

Figure 4.3.5: Polygon chain which models an elastic band that freely interconverts between director bend and biaxial twist.
This chain quantitatively embodies the geometry of the TB heliconical state as manifest in the relationship $B(\theta_H) = (1/R_{mol})\sin\theta_H$ from the plot in Figure 4.3.4a, and motivates our picture of the TB phase as an assembly of sterically stabilized, oligomeric chains. (a) In this geometry, the rigid triangular and rectangular plates form a chain by sharing common edges which are flexible hinges, enabling the chain to twist if its bend is reduced as sketched and described geometrically by the relationship indicated in the inset. (b) The polygon chain is attached to a helical rod that is flexible but of fixed length $2\pi R_{mol}$, and which can be made to change its pitch by sliding its upper end along z. Here, only a half-period of the helix is drawn. The red cylinder changes radius as $\sin\theta_H$ to keep the rod length constant. In its flattened state ($\theta_H = 90°$), the chain models directly the PB regime in Figure 4.3.4c, in this case with eight segments and eight 45° bends. If θ_H is reduced then this structure rigorously maintains the conditions $q_H(\theta_H)\cos\theta_H = 1/R_{mol}$, and $B(\theta_H) = (1/R_{mol})\sin\theta_H$, *i.e.*, it moves on "the line", like the data in Figure 4.3.4a. In the fully stretched out state ($\theta_H = 0°$), the twisted biaxiality (TBX) regime, the director bend is replaced by twist of the biaxial vector $\boldsymbol{p}$ (magenta arrows), with a pitch $p_H = 2\pi R_{mol}$ mediated in eight twist steps of 45° each, as suggested by non-resonant x-ray scattering data.

bend regime ~8 segments around the $2\pi R_{mol}$ circumference, and indeed, as shown in Figure 4.3.6a, the PB regime is well modeled by the arrangement of four 45° bent rod molecules. We propose that each ring in this structure is stabilized by neighboring rings, in an arrangement where adjacent rings have a difference in azimuthal orientation of 45°, such that the flexible molecular centers in one ring are over the regions of fluctuating end-to-end molecular contacts in the neighboring ring, an entropically favored association. This makes a construction like a cylindrical brickwork chimney, discussed later. With this choice, eight rectangle long edges must make a complete turn,

so the rectangle length, L, is chosen such that $8L \sim 2\pi R_{mol}$. The corresponding magnitude of director bend is then $B = (\pi/4)/L = (2\pi)/8L = 1/R_{mol} = B_{mol}$.

The helix can be tuned by pulling the ends of the rod so that they become separated along a line parallel to $\hat{\boldsymbol{z}}$, the separation being the pitch p_H, as indicated by the black arrow in Figure 4.3.1e, which decreases θ_H and makes the rod less bent everywhere along its length. The bend angle β of the local elements thus decreases from the maximum of $\beta_o = 45°$ causing them to buckle, the triangle swinging out of the plane of the rectangles to affect less bend, and in the process inducing a local relative twist τ of the rectangle planes, which are free to rotate about the rod axis, as sketched in Figure 4.3.5a. With this geometry, if the tilt of $\hat{\boldsymbol{n}}(z)$ relative to $\hat{\boldsymbol{z}}$ is θ_H, then the angle between the triangle and rectangle planes will be $-\theta_H$, the condition which keeps the triangle planes always parallel to the x-y plane. If the separation of the rod ends is increased and p_H approaches the rod length $2\pi R_{mol}$, then $\theta_H \to 0$, $B_H \to 0$ as $B_H = \sin\theta_H/R_{mol}$, and the rod becomes nearly straight, with the local geometry in Figure 4.3.5a. The triangle plane is now normal to the rod, and its initial induced bend in the rod of $\Delta\varphi = 45°$ is now completely converted to an induced local relative twist about the director of the rectangle plane normals through $\Delta\varphi = 45°$ at each hinge, as in Figure 4.3.5b. The bend angle, β, twist angle τ, and β_{mol} are geometrically related as shown in Figure 4.3.5a.

The rectangles also represent the principal axes of the local biaxial nematic ordering tensor of the director field (director $\hat{\boldsymbol{n}}$, flexoelectric polarization direction $\hat{\boldsymbol{p}}$, auxiliary unit vector $\hat{\boldsymbol{m}}$), as shown in Figure 4.3.5a. Thus, as θ_H increases, the overall structure of a single pitch is converted from the $\theta_H \sim 90°$ state: a series of eight steps of 45° rotation of director bend and of local biaxiality about its $\hat{\boldsymbol{m}}$ axis on the circumference of the circle of radius R_{mol}; to the $\theta_H \sim 0°$ state: a series of eight steps of 45° twist rotation of the local biaxiality about its $\hat{\boldsymbol{n}}$ axis, on a path along $\hat{\boldsymbol{z}}$ of length

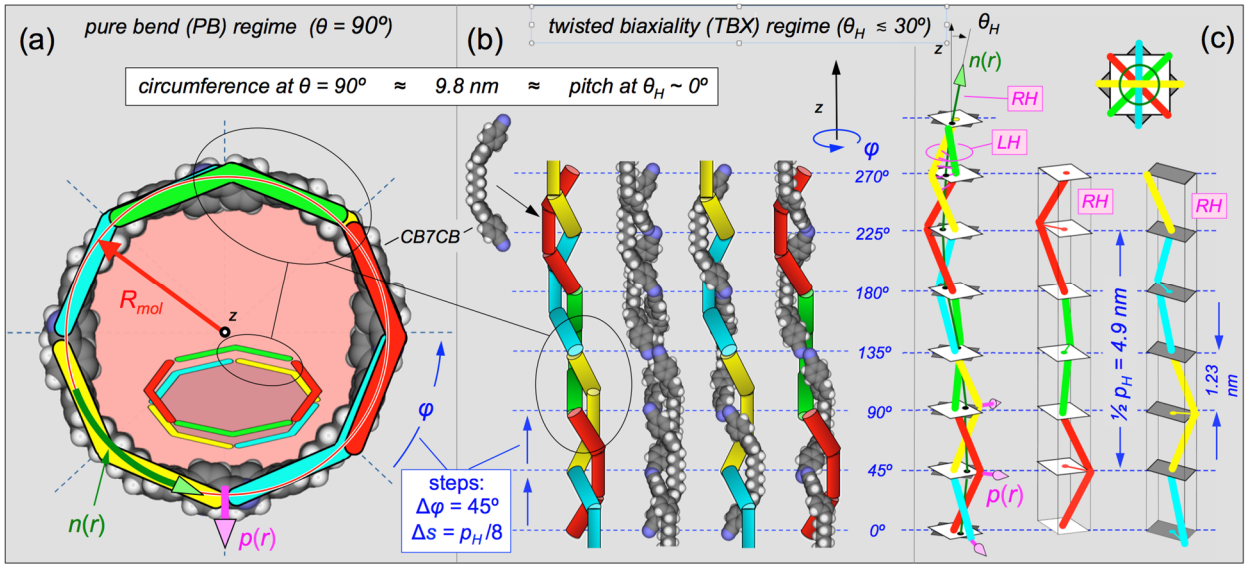

Figure 4.3.6: Realization of the polygon chain model for discrete molecules, modeling CB7CB by bent rods.
Oligomeric chains are formed in both the PB and TBX regimes by the brickwork tiling of half molecules, with a repeat distance indicated by the blue dashed lines, corresponding to the short-range periodicity observed in diffuse, non-resonant x-ray scattering (Figure 4.3.7). Each segment contains a pair of half-molecules. This tiling is stabilized by the entropic association of molecular ends and CB7CB's flexible center. The constraint of the bend data and the polygon chain model is that the helix pitch p_H at small θ_H in the TBX regime is the circumference of the circle in the PB regime. Since p_H at small θ_H is 8 segments in length, the change in φ per segment is taken to be 45° in both the PB and TBX regimes. (a) PB regime showing the brickwork tiling of molecules as in Figure 4.3.5c: two chains of 45° bent molecules (red-green, yellow-cyan) forming eight segments of half-molecule pairs, with angular bend jumps of $\Delta\varphi = 45°$ between each pair, and a $\Delta\varphi = 45°$ phase difference in the orientation of the two chains. The small inset shows an oblique view of the packing structure. (b,c) Oligomeric chain structure showing bent-rod and molecular models of the brickwork tiling in the TBX regime: two chains of 45° bent molecules (red-green, yellow-cyan) forming eight segments of half-molecule pairs, with angular biaxial twist jumps of $\Delta\varphi = 45°$ between each pair, and a $\Delta\varphi = 45°$ phase difference in the orientation of the two chains. The two right-handed (RH) chains associate to form a left-handed (LH) duplexed helix. (c) For uniaxial half-molecules, the optical polarizability of a given segment can be obtained geometrically. The optical cone angle is $\theta_H \sim 10°$ for the structure drawn, the case where the molecular planes are untilted.

$2\pi R_{mol}$. This scenario precisely maintains $q_H \cos\theta_H = B_H$ throughout the range of q_H, i.e., puts B_H vs. $\sin\theta_H$ on "the line". We denote these ranges of large and small θ_H respectively as the pure bend (PB) regime ($\theta_H \sim 90°$) and the twisted biaxiality (TBX) regime. The RT model shows directly that the structural stability of the local elements through the transition from pure bend to twisted biaxiality is what is required to maintain the compressional elasticity of the pitch under the condition that $B_H \to 0$ and director curvature elasticity drops out. The TB phases observed so far

typically have $\theta_H \lesssim 30°$, so they are much closer to the twisted biaxiality limit than the pure bend. Thus, in "TB" the twist should be taken to mean twist of the biaxiality. The $\theta_H \sim 0°$ regime represents the state of the helix dominated by twisted biaxiality but having no macroscopic optical tilt. Such a state is achievable as will be shown below. In the CB7CB mixtures the TB phase appears to come in with a small but finite θ_H, consistent with the optical, x-ray and DSC evidence for a first order N – TB transition.

The RT model can be made for any angle β_{mol}. If β_{mol} is small, then $\tau^2 + \beta^2 \cong \beta_{mol}^2$, with β and τ becoming the orthogonal projections of a vector of magnitude β_{mol}, constrained to move on a circle (Figure 4.3.5a). In the limit that $\beta_{mol} \rightarrow 0$ with L/β_{mol} constant and assuming that the hinge bends remain highly flexible, the RT chain becomes a like a sheet of paper bent into the accordion fold of a fan, with high bending rigidity in the radial direction, and low bending rigidity in the circumferential direction. Upon pulling the bend out, such a sheet will exhibit little elastic resistance against conversion from continuous bend to continuous twist. In the continuum limit $B_H^2 + T_{BX}^2 = B_{mol}^2 = B_H^2 = \beta_{mol}^2 / L^2$, the result also derived in Figure 4.3.1f from the projective geometry of the helix. The exchange of bend and twist is controlled by B_{mol} even in the limit of zero bend ($T_{BX} \cong B_{mol} - B_H^2/2B_{mol}$).

Steric Oligomerization of Bent Molecular Dimers – In the RT model, the constraint that $q_H \cos\theta_H = B_{mol}$, independent of θ_H, is built into the model by the fixed length of its chain of polygons, a condition that would seem most applicable to a system of locally-bent flexible oligomer or polymer chains. In the dimer TB phases considered here, there are no chemical links between molecules, so it is necessary to understand, in the context of independent bent molecules, how such a similar polymer-like condition could come about in both the PB and TBX regimes, how the PB

and TBX regimes are linked, and, therefore, how biaxial twist in absence of bend comes to be controlled by B_{mol}.

We propose that molecular bend and steric packing constraints of the condensed TB phase combine to stabilize oligomeric chains of molecules, and that the brickwork packing motif, introduced in Figure 4.3.4c and detailed in Figure 4.3.6a, is the common structural feature that stabilizes the chains and connects the PB and TBX regimes. The brickwork packing of a pair of adjacent chains can be visualized as a string of segments, each containing a pair of oppositely directed molecular halves linked by interfaces, each containing the center of a molecule in one chain and the tails of two in the other. This motif has also been found in molecular dimer LC structures [159]. This assembly is stabilized by the well-known tendency for rigid and flexible molecular subgroups to nano-phase segregate [166], with the flexible molecular centers most readily accommodating the fluctuations in relative position of neighboring molecular ends or tails. We refer to a duplex helix chain formed in this way as a duplex helical tiled chain (DHT chain, DHTC). The intraduplex tiled linking is responsible for the apparent fixed contour length, $s(\Delta\varphi = 2\pi) = 2\pi/B_{mol}$ along $\hat{\boldsymbol{n}}(\boldsymbol{r})$ and manifested in the construction of Figure 4.3.5.

This proposal is supported by the observation of a diffuse non-resonant x-ray scattering feature in the N and TB phases of pure CB7CB, having a peak on the q_z-axis, at $q_m \approx 5.05$ nm^{-1} [15]. A similar peak is found in the N and/or TB phases of a variety of other bent molecular dimers, with q_m in the range 4 nm^{-1} < q_m < 5 nm^{-1} [48,78,84,92,99,103,107,111]. This indicates a periodic electron density modulation and therefore molecular positional ordering along the helix with a fundamental periodicity of $d_m \cong 1.25$ nm, consistent with the presence of short ranged periodic positional correlation of similarly structured molecular segments along $\hat{\boldsymbol{z}}$. This finding supports the brickwork association proposal since this value of d_m is close to half of the molecular length

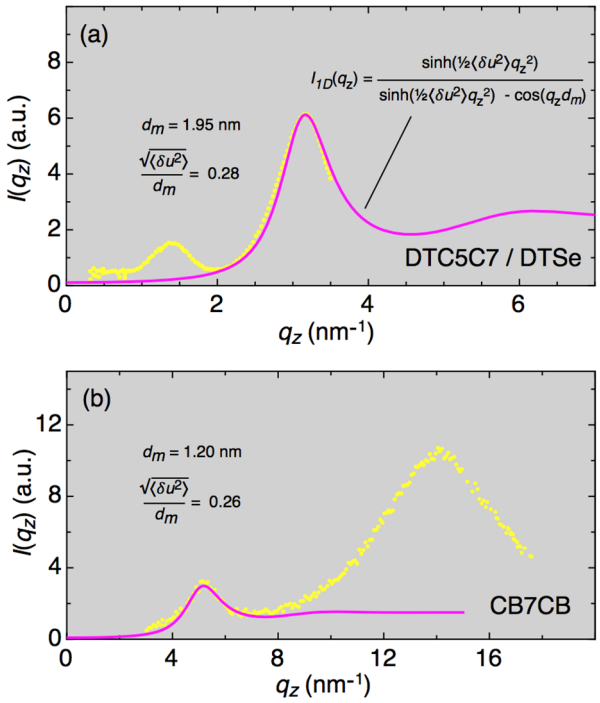

Figure 4.3.7: Non-resonant x-ray scattering of bent molecular dimers in the TB phase in two materials where scans are published. We model the periodic segment structure as a one-dimensional chain of identical particles (segments) connected by harmonic springs. The corresponding structure factor, $I_{1D}(q_z)$ [167,168], is fitted to the published scans from (a) DTC5C7 [111] and (b) CB7CB [48]. $I_{1D}(q_z)$ depends on three parameters: a multiplicative amplitude; $\langle\delta u^2\rangle$, the mean-square relative displacement of nearest neighbor particles; d_m, the average interparticle spacing. The fits show that this simple chain 1D model can describe the segment periodicity peak well, with relative RMS displacement of the neighboring segments by ~25% of their length, a reasonable value for such an assembly. DTC5C7/DTSe shows a subharmonic peak, indicating a weak tendency for full molecular length ordering, that sharpens into a smectic layer reflection at low T. The broad peak in the CB7CB scan is that from the side-by-side molecular packing that shows up in this powder average.

M =1.4 nm of extended CB7CB, which is that required for the segment length in a brickwork tiling. In fact, comparison of d_m with extended molecular length for the bent molecular dimer systems for which d_m data is available, noted above, shows that the condition $d_m/M \sim 1/2$ appears to be a general trend. In CB7CB, since d_m is comparable to $p_H/8 = 1.22$ nm, it is close to the brickwork segment length in the PB regime on the R_{mol} circle (Figure 4.3.6a), an observation that can be taken as evidence for there being similar segments at small θ_H.

Another common feature of the fitted chain segment scattering $I(q_z,q_\perp)$ [167,168] in the materials in Figure 4.3.7, is that the width of the diffuse peak in the direction normal to the helix axis z, $\delta q_\perp$, is significantly larger than δq_z, its extent along the helix. In some cases this appears to be due to mosaic broadening due to alignment defects, but in the TB phase in the DTC5C7/DTSe mixtures [111], for example, the narrow angular width in $\boldsymbol{q}$ of the resonant q_H peaks shows that the sample is well aligned, and therefore that the broadening of $I(q_z,q_\perp)$ in the $q_\perp$ direction is intrinsic. The corresponding correlation lengths $\xi_\perp$ and ξ_z have the inverse relationship, implying that the

correlation volumes giving the diffuse non-resonant scattering are extended along $\hat{z}$, *i.e.*, a chain-like periodicity along $\hat{z}$ rather than layer-like correlations.

Duplex Helical Tiled Chain (DHTC) Structure of the TB Phase – The challenge then is to develop a model of the TB helix with small θ_H in which it is made up of at least pairs of molecular chains in a brickwork tiling with subsections along $\hat{z}$ of pairs of antiparallel half-molecules, in which, for CB7CB the structural twist between segments is 45°. To this end, we considered the organization of single stick and space-filling molecular models consistent with the above requirements. The PB regime is readily modeled by the packing of all-*trans* space-filling models of CB7CB and, as in Figure 4.3.6, by either two- or three- segment bent stick models having 45° or 30° bends, respectively. In the PB limit, brickwork tiling of either stick model gives a bend of 45° per segment and four molecules per ring (Figure 4.3.6a), so that the change in azimuthal orientation $\Delta\varphi$ is 45° per segment.

The required structures are shown in various representations in Figure 4.3.6b,c and Figure 4.3.8. The basic structural associations are of three molecules like that of the green, cyan, and yellow groups inside the black elliptical rings in Figure 4.3.6a,b, wherein terminal groups of the cyan and yellow tuck into the volume of hard-to-fill space vacated by the bending of the green, and can associate with the flexible central aliphatic linkers. This scenario is repeated for the next segment along $\hat{z}$, among a group rotated through 45° relative to the initial one and having the cyan molecule in the center, and so on for all z. The stick models in Figure 4.3.6b,c and Figure 4.3.8 show that this structure is duplex helixed, made up of two identical, right-handed helical chains of molecules, each transforming into the other by a translation of a single segment length followed by a 45° rotation in azimuthal angle. The paired assembly of two chains is stabilized in both the PB and TBX cases by a combination of a constraint, in the former to be on the cylinder or in the

latter to be in a tube created by neighboring chains, and by the pressure exerted by the neighboring molecules. In the pairing of the single-strand chains, the overlaps stabilize the structure and the interlocking bends promote the filling of space. In the bent stick representation of Figure 4.3.6c, the half molecular rods can be taken to represent the optical anisotropy of the halves of the molecule. Taking this half-molecule polarizability to be uniaxial, the effective optical anisotropy of a segment of the duplex helix can be obtained using the construction in Figure 4.3.6c. Here, the white square at each level is marked with a black dot that marks the midpoint between the intersections of the two chains with the square. The dark green line connects the midpoints from square to square. Thus, in a given segment the green line construction will give the orientation of the local principal axis of the average dielectric tensor having the largest refractive index, which we take to be the local director. Thus, the green line represents the trajectory of the optical $\hat{\boldsymbol{n}}(\boldsymbol{r})$, which is also a right-handed helix. This construction shows that, in a given segment of the DHT chain, the tilts of the half-molecular optic axes away from $\hat{z}$, in this case by ~ 22°, tend to cancel one another, leaving a much smaller effective optical heliconical cone angle, in this case $\theta_H \sim 11°$. The magenta labels in Figure 4.3.6c indicate the handedness of the various helices, with the single

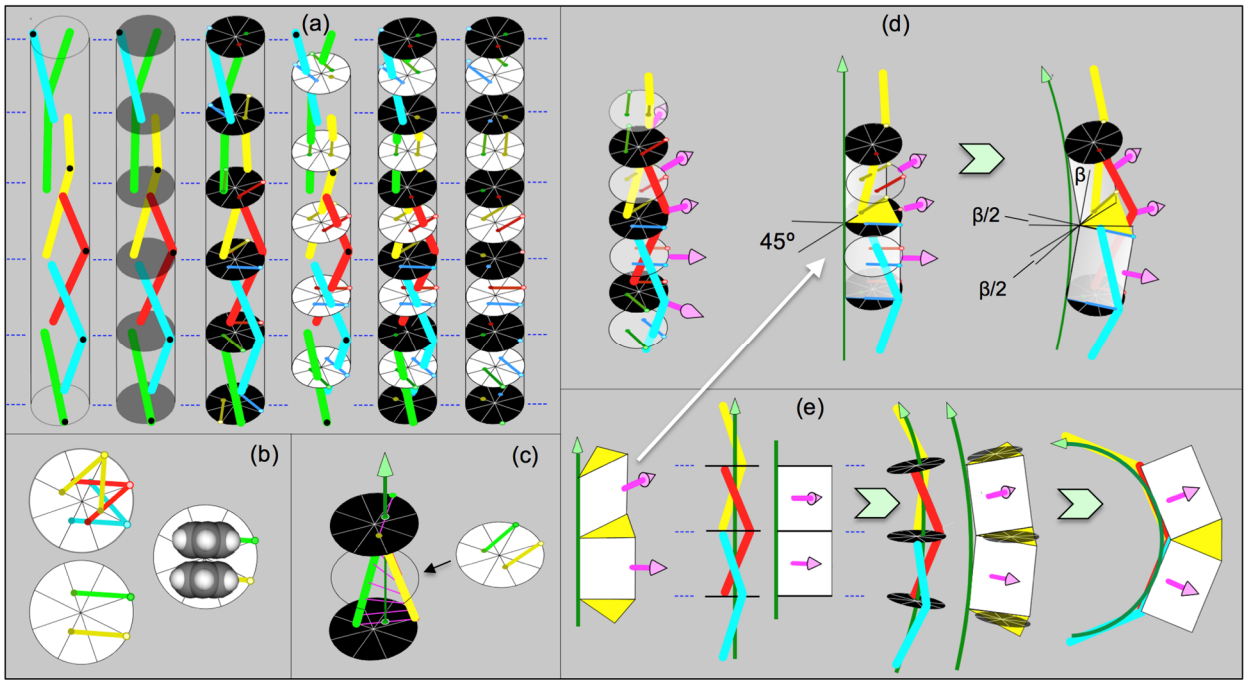

Figure 4.3.8: Representation of the TBX regime oligomeric chain structure for $\theta_H \sim 0°$.
(a) White circles show the projections onto the x-y plane of half-molecules in each segment, and the black circles the projections of half-molecules on to the interfaces between segments. (b) The planes of the 45° bent molecules are tilted from z by an angle (~10°) such that the half-molecule projections on the x-y plane are separated by $\Delta\varphi = 45°$, matching the reorientation in successive segments (cyan, red, yellow). This results in parallel chain projections within the segments (yellow, green). This drawing is proportioned with respect to the diameter of the chains according to the molecular volume of 0.76 nm^3. The segments are 1.23 nm along z and 0.88 nm in diameter, that of the black and white circles. The phenyl ring profiles are to the same scale. (c) When biaxial optical polarizabilities with parallel projection are added, they give an untilted biaxial average ($\theta_H \sim 0°$). (d,e) Mating of the polygon chain model with the brickwork oligomeric chain. The projections of the half-molecules onto an interface form a 45° angle that matches that of the yellow triangles in Figure 4.3.5. If the oligomeric chain is bent, its black disc, representing the interface between two segments, tilts but remains parallel to the yellow triangle. Thus, in the oligomeric chain, even at small θ_H, the condition $q_H \cos\theta_H = 1/R_{mol}$ is enforced, keeping B_H in Figure 4.3.5a on "the line".

chains and the director helix being right-handed (RH). Interestingly, the duplex helix is left handed (LH).

For clarity, the molecules in Figure 4.3.6 are arranged with more symmetry than they will exhibit in a real TB material. Generally the planes of the bent molecules in the helices of Figure 4.3.6b,c will be tilted away from $\hat{z}$, through an angle ψ as shown in Figure 4.3.8 for both signs of tilt from $\hat{z}$. The might go to zero at some particular temperature, like the unwinding of the helix in a chiral nematic at a particular temperature.

Figure 4.3.8 presents the fully formed DHTC structure in the pure TBX limit for which the optical director tilt $\theta_H = 0°$. In this structure, the projection of the halves of a given tilted molecule onto the x-y plane has an opening angle between them of 45° (Figure 4.3.8c), the same as the rotation $\Delta\varphi = 45°$ per segment. This condition requires a tilt of the molecular plane from $\hat{z}$ of 9.9°. In this case, the two molecular halves in a given segment have parallel projections onto the x-y plane (Figure 4.3.8a,c). Since they also have equal and opposite tilts there must be a principal axis along $\hat{z}$ of their average biaxial contribution to the dielectric tensor (Figure 4.3.8d). Starting from this structure, a heliconical director field of finite θ_H can be generated by changing the molecular tilt or by helical deformation the DHT chain. Introducing director bend into the DHT chain reduces biaxial twist, following the geometric projection scenario of Figure 4.3.4f and of the RT model in Figure 4.3.5. This comes about as illustrated in Figure 4.3.8d,e, showing that, on the boundary between the two duplex chain segments containing the halves of the red molecule (denoted by a black circle), the projections of the halves of its cyan and yellow molecular neighbors make a 45° angle to one another. As indicated in Figure 4.3.8d, this corresponds to twist $\tau = 45°$ for $\beta = 0$ at a yellow triangle in Figure 4.3.5a. In the presence of director (heavy green line) bend, β, the rotation of these neighbors relative to the red molecule is of opposite sign ($+\beta/2$, $-\beta/2$) and applied on the projections, as on the edges of the yellow triangle, causing the black disc plane, with application of bend, to rotate about $\boldsymbol{p}$, remaining, as in Figure 4.3.8b, coplanar with the yellow triangle as it reorients (Figure 4.3.5a). Elastic deformation of the DHT chain then satisfies the RT model constraints which put $B_H(\theta_H)$ on "the line" in Figure 4.3.4a: $q_H \cos\theta_H = B_{mol}$, $B_H = B_{mol}\sin\theta_H$, $T_{BX} = B_{mol}\cos\theta_H$, and $B_H^2 + T_{BX}^2 = B_{mol}^2$. For B_H small, then, the reduction in biaxial twist is controlled by B_{mol}, with $T_{BX} \approx B_{mol}\,(1 - B_H^2/2B_{mol})$. In the limit of large bend twist is eliminated and the structure evolves toward the PB limit (Figure 4.3.8e).

Three-Dimensional Heliconical State – The bulk TB phase is a 3D, space-filling packing of duplex helical tiled chains (DTHCs). The overall orientational ordering with uniaxial positive birefringence means that the DHT chains are generally oriented parallel to one another, making the TB a hierarchical nematic superstructure of anisotropic self-assembled oligomeric chains. In the packing of cylindrical objects that are helically modulated, the helical contours on adjacent facing cylinders cross each other (like the stripes on a pair of parallel barber poles of the same handedness if put into contact). This geometry tends to suppress melding of the chains and to maintain the cylinders as distinct entities in the packing. Each DHT chain then is effectively confined to an on-average cylindrical hole in the fluid by its neighboring chains which exert an effective pressure like that coming from osmotic pressure in a depletion interaction. This picture is supported by the experimental finding that the $B_H(\theta_H)$ data of all the mixtures lie on the same line in Figure 4.3.4a, indicating that they behave as if they all have the same B_{mol} (at $x = 37.5$ we might have expected a significant dilution effect leading to a smaller B_{mol}). The constancy of B_{mol} suggests that in the structures determining the pitch, the DHT chains in the case of in the TBX, are comprised dominantly of the bent dimers, and that the 5CB is a filler in between. The 5CB dilution lowers the phase stability and reduces θ_H, but this all occurs with $q_H \cos\theta_H = B_{mol}$, implying chains under the same constraint: $\mathrm{d}\varphi/\mathrm{d}s = B_{mol}$.

Next, we consider the steric packing of the DHT chains that makes up the bulk phase. The fact that the RSoXS from the bulk TB exhibits diffraction spots from oriented domains that are 3D smectic-like, that is, having resolution-limited width in δq_z, indicates that the long range ordered pseudo-layer scattering objects are arrays of lamellar sheets extended in the in-plane direction [70,111]. This means that in the bulk TBX packing, the phase φ of the twist in a DHT chain must become coherent with that of its neighbors, a condition that has been observed in

nematic phases made by packings of chiral particles internally structured as a steric repulsive helical line, realized, for example in suspensions of helical flagellae [164], and in the extensive simulations of steric helices of Kolli *et al*. [136]. The existence of the DHT chains opens up the possibility of a number of other possible arrangements of these objects such that, for instance, it is feasible to observe a transverse twisting of these DTH chains akin to a TGB* phase in some range of parameters. Another example relevant to the TB phase is the helical nanofilament phase found in neat bent-core systems [53,69] in which chiral filamentous bundles of a few smectic layers achieve macroscopic phase coherence of their twist solely by interacting through their periodic biaxiality.

The Kolli simulations [136] appear to be particularly applicable to describe the interaction of, and the potential of long-range phase ordering for, the DHT chains for finite θ_H in the TBX regime. Comparison of the Kolli particles with the steric shape of the DHT chains of CB7CB shows particles with helical radius $r/D \approx 0.2$ and pitch $p \approx L \approx 10D$ match the CB7CB DHT chains quite well. The Kolli *et al*. phase diagram for $r/D = 0.2$ shows that particles having $r/D = 0.2$ systematically give I, N, TB and smectic phases, with the TB range decreasing as the pitch becomes comparable to and longer than the particle contour length. Thus, the single pitch duplex CB7CB chains should be able to order into a 3D TB phase if sufficiently long and rigid. The TB range is limited with increasing volume fraction by the appearance of smectic ordering, corresponding to the positional ordering of the particles into smectic layers of thickness comparable to their length. In the case of living polymer chains, like what we propose for CB7CB, the effective particles will be transient and polydisperse, the latter condition well known to strongly suppress smectic ordering [169], an effect which may expand the TB range.

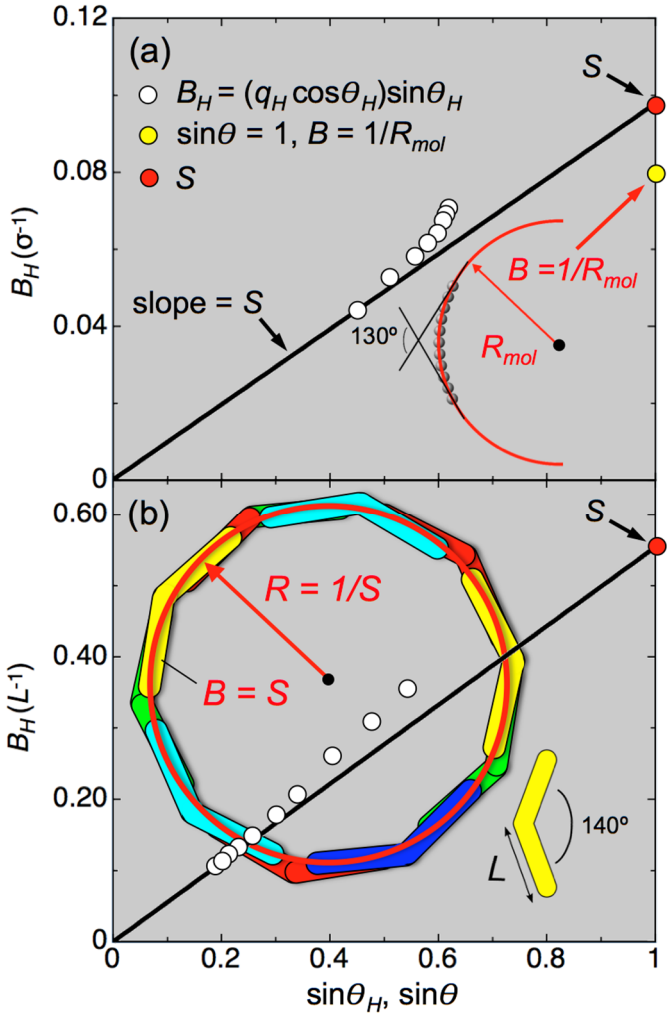

Figure 4.3.9: Variation of $B(\theta_H)$ vs. $\sin\theta_H$, for two statistical mechanical model systems of interacting bent particles. The black lines are drawn to match the measured bend at the smallest θ_H. (a) Monte Carlo simulation of TB ordering of steric particles made by rigidly chaining 11 hard spheres in the form of circular arcs [135]. The length scale is the sphere diameter, σ. The molecular curvature construction of Figure 4.3.4 is also sketched, giving a molecular bend $B_m = 1/R_{mol} = (2\pi \cdot 50)/(360 \cdot 11) = 0.079/\sigma$, plotted as the yellow dot at $\theta = 90°$. B_m is comparable to the slope of the line, as was found for CB7CB in Figure 4.3.5. (b) Generalized Maier-Saupe mean-field theory of the TB ordering of bent rods in which the rod halves were considered as independent interaction centers [122]. Also sketched is the PB construction of Figure 4.3.5c, where R is simply set to $R = 1/S$, i.e., the bend B in the circular construction is set to S, the bend on "the line" extrapolated to $\theta = 90°$. It seems remarkable that a mean-field model can capture this geometry.

For $p \approx L$ and $r/D = 0.2$ the Kolli *et al*. helical particles [136] behave as if they are smooth, like those of Barry *et al*. [164], which have helical glide symmetry. In these cases, if the steric helical interaction is reduced, for example, by reducing r/D or making p/L large, the system will revert to a simple nematic or smectic phase. However, the DHTCs are not smooth, but are periodically structured, with a local biaxial shape, so the role of variations of the steric shape along the DHT chain must also be considered. Figure 4.3.5b, Figure 4.3.6c, and Figure 4.3.8 all exhibit aspects of the biaxiality of the DHT chains. Figure 4.3.5b for the $\theta_H = 0°$ case and Figure 4.3.6c show that the projection of the segments onto the drawing plane varies in effective shape along the chain, with a period equal to half of that of the

helix. Generally, each segment is biaxial, with a steric cross-section in the x-y plane that has the symmetry of an ellipse. This elliptical shape rotates in azimuthal angle φ along the chain (biaxial twist), as in a twisted ribbon of zero net local curvature, with a period of $p_H/2$, equal to four segment lengths as is clear in Figure 4.3.5b. In the TBX limit, this is the only periodicity of the DHTC. In a dense packing of the DHTCs, steric variations in shape, especially periodic ones, will lead to the development of correlations between chain positions along $\hat{z}$. This will be an especially strong effect if the oligomerization has substantially reduced the translational entropy for displacement along $\hat{z}$. In the helical nanofilament case [52,69], where the structural periodicity is the helix half-pitch and filament steric profile almost circular such that the neighboring filaments only weakly sense each other's grooves, the filaments have a strong tendency to order with their biaxial twist in phase. In the DHTC case, sufficiently large ellipticity and packing density will lead to a 3D structure in which adjacent duplexes will align out of phase to facilitate packing. Twisted ribbons, for example pack best when shifted by a quarter of their pitch.

RSoXS as a Probe of the Duplex Helical Tiled Chain Model – Given that we now have a fairly detailed structural model, we reconsider RSoXS as a probe of the heliconical structure of the TB phase. Interestingly, the first applications of resonant scattering to LCs was to probe the heliconical molecular orientational ordering in chiral tilted smectic phases, wherein the molecules are confined to layers, sorting out layer-by-layer sequences of azimuthal orientations of tilted molecules [170,171]. In this context, the general theory of resonant scattering was applied to the smectic case [172]. This formalism has recently been applied in a comprehensive analysis of RSoXS scattering from the TB phase by Salamończyk *et al.* [130].

RSoXS at the carbon K edge (incident wavelength, $\lambda = 4.4$ nm) gives a range of scattering vectors $q < 2\pi/2.2$ nm, probing length scales through the nanometer range down to ~ 2 nm:

molecular, but not atomic, size. In this *q* range, molecular subcomponents such as the biphenyls in CB7CB act nearly as composite entities in the scattering process, being describable by second-rank molecular polarizability tensor scattering cross-sections, as in deGennes' formulation of light scattering by fluctuations in director orientation [17]. In analogy with light microscopy, RSoXS could even be used to visualize patterns of birefringence of LC phases and textures with x-ray resolution using depolarized transmission.

Salamończyk *et al.* have pointed out that in the scattering from columns of helical precessing tilted rods, averaging together pairs of columns shifted relatively in phase by a half period of their biaxial polarizability renders the net polarizability the same in every quarter period and the second harmonic disappears. In the few experiments where the second harmonic might have been seen, it has not found [70,111,130], indicating that such averaging may be taking place in the TB phase. In the case of the DHTCs, shifting a pair of chains by two segments and averaging will eliminate the second harmonic. However, achieving this in arrays of DHTCs may be problematical, since frustration effects come into play on the closest-packed 2D hexagonal lattices.

Asymmetric Elasticity of the TB Helix – A relevant feature of the lamellar-like helical ordering of the TB phase is its strange asymmetry in the response of the TB helix pitch to compressive or dilative stress [70]. In typical fluid lamellar LCs, such as the smectics A and C, stresses tending to change the layer thickness encountered in typical textures. For example planar-aligned cells or focal conic powders in capillaries exhibit little observable variation in layer spacing in x-ray scattering experiments, except near phase transitions where the compressional elastic constant can become small. In the TBX regime of CB7CB, the layer spacing exhibits a well-defined minimum trajectory vs. temperature, but it can be significantly increased in irregular fashion from this minimum value by dilative stresses appearing in textures in 1 μm thick samples

between flat plates. The DHT chains can be expected to respond in an asymmetric way to stress along $\hat{z}$, with the end-to-end packing of the molecules in the chains resisting compression, but the steric association of the overall structure being rather soft against stretching, providing a natural explanation for this behavior.

Model Systems of Bent Rigid Molecules – We sought to explore the role of molecular bend in other TB systems. The only others of which we are aware and for which data sets of p_H vs. θ_H are available are the mean-field theoretical model for bent rods of Greco *et al.* [135], and the Monte Carlo simulation of Greco *et al.* of hard spheres assembled to make steric circular arcs [122]. These models are of particular interest because they treat collective TB behavior for bent objects that are rigid. Figure 4.3.9a and b show plots of B_H vs. $\sin\theta_H$ calculated from $p_H(\theta_H)$ for the arcs and bent rods respectively. The black line in each plot is drawn through the origin and $B_H(\theta_H)$ for the smallest θ_H. The general behavior of $B_H(\sin\theta_H)$ is similar to that of the CB7CB mixtures in Figure 4.3.4a, but with a tendency to increase relative to the black line with increasing $\sin\theta_H$, which is also seen weakly in neat CB7CB (Figure 4.3.4a).

In the case of the circular arcs, we carried out the R_{mol} construction of Figure 4.3.4b, with the result shown in Figure 4.3.9a. We found that $R_{mol} = 12.6$ in units of the sphere diameter, σ. The corresponding $B_{mol} = 1/R_{mol} = 0.08/\sigma$ is comparable to the $B = 0.1/\sigma$ extrapolation of the black line, indicating a relation between the PB and TBX limits similar to that in the CB7CB mixtures. This makes the hard arcs a very interesting system for exploration of the DHTC structure.

Turning to the bent rod case, Figure 4.3.9b shows that $B_H(\theta_H)$ obeys $B_H = S\sin q_H$ rather well for $\theta_H < 15°$, with a slope $S = 0.56/L$, where L is the length of one of the arms in the bent rods. In Figure 4.3.9b we have used the small-angle value of S to extrapolate to $\theta_H = 90°$ in order to determine the radius of the cylinder $R = 1/S$ in the PB regime. The resulting construction using

the shape of the simulated bent rods, shows a quite reasonable PB limit. This is an exciting result because this model approaches understanding the TBX regime from a mean-field statistical mechanical approach that is entirely different from the geometrical model building that we have employed. That it captures the essence of the geometry of "the line" offers an opportunity to understand in detail the evolution of the local geometry to keep the system on the line in absence of change in molecular conformation.

Both of these models employ rigid molecules and yet seem to exhibit the same essential geometrical behavior as the CB7CB system, which was rationalized on the basis of nanophase segregation of flexible (the central alkyl linker and the tail ends) and rigid molecular subcomponents (cores): the molecular ends find entropic freedom by associating with the flexible cores. We propose that in systems of rigid bent hard particles the analogous association is between the particle ends and the free volume available in the pocket of difficult-to-fill space created by molecular bend.

In summary, the heliconical structure of the CB7CB mixtures exhibits a remarkable dependence on concentration and temperature in which director bend and biaxial twist exchange under a strict geometrical constraint that equates the magnitude of director bend at one extreme of cone angle to the magnitude of biaxial twist at the other extreme (moving on "the line"). This constancy is related to the ability of the TB phase to maintain inherent bend and a fixed contour length along the director that are both elastically stabilized, behavior most directly understood on the basis of the longitudinal connection (transient oligomerization) of molecules. This, and the x-ray observation of half-molecular length periodicity along the TB helix, leads to the model of the self-assembly of half molecule-long segments into duplex helical tiled chains of molecules as the

basic structural element of the TB phase. The geometrical constraint then shows up as $\Delta\varphi = 45°$ director bend jumps from segment to segment in the PB ring limit, and 45° biaxial twist jumps in the TBX limit. There is no symmetry requirement for this equality. The structural organization of the DHT chains should accommodate a range of possible $\Delta\varphi$'s per pseudo-layer spacing. For example it appears that DTC5C7/DTSe [111] and AZO7 [90], with ratios of $p_H/p_m \sim 6$ in the TBX regime, are $\Delta\varphi \sim 60°$/jump, and there seems to be no structural impediment to 90° per jump [159]. Since these $\Delta\varphi \sim 60°$ materials are unlikely to have comparably large bend jumps in the PB regime, they will not move on "the line". Thus, how general the CB7CB behavior is among the TB materials remains to be seen. However, in any case, the CB7CB scenario appears to offer a useful benchmark for relating the molecular structure and macroscopic behavior in TB phases. If the data are not on "the line" as for the simulated systems in Figure 4.3.9, the deviations can be explored by comparison with CB7CB ideal elastic behavior. For systems exhibiting the CB7CB scenario, there remains the question of relating the slope S of the B_H vs. $\sin\theta_H$ curve to the molecular shape. CB7CB also turns out to be extremely simple in this regard (maybe not just a coincidence). In the case of CB7CB, the extended molecule is shaped like a nearly circular arc, so the B_{mol} is readily determined from the molecular shape and S matches this bend very well. In general, however, it will not be so easy to assess molecular bend. For example, flexibility in molecules with longer aliphatic linkers will likely make B_{mol} smaller than estimates based on extended molecular shape. This leads to the question of how to design calculational or simulation schemes of the pure bend regime that can quantitatively predict the TB structure by determining B_{mol} in order to get S.

4.4. THE CBNCB SERIES: STRUCTURE-PROPERTY IN A HOMOLOGOUS SERIES THAT FORMS THE TB PHASE

We synthesized a series of homologues of CB7CB with alkyl linker number n = 5 to 17 odd to investigate the effects of linker length on the properties of the TB phase. We identified the TB phase in this CB*n*CB series and investigate them primarily with resonant and non-resonant x-ray scattering techniques. We find that increasing n tends to increase the thermodynamic stability of the nematic phase, while that of the TB phase diminishes. The CB*n*CBs with larger n also have dramatically longer helix pitch and enhanced structural fluctuations of the helix near the TB – N transition. We make a low-temperature extrapolation of the measured helix pitch as a function of temperature for each member of the series to extract the ground state pitch – the TB pitch observed when fluctuations are frozen out. We find that this ground state helix pitch scales nearly linearly with linker number. Our study not only demonstrates the nanoscale effects of lengthening the chemical linker in the CB*n*CB series, but also highlights the surprising importance of fluctuations in the behavior of the TB phase.

Since the identification of the TB phase, the academic focus has moved to understanding the mechanics of the phase along with its associated structure-property relationships. In investigating structure-property relationships, we vary the structure of a self-assembly building block and observe the effects on the subsequent bulk assembly. In LCs, the building block is typically a small organic molecule ~3 – 5 nm in size composed of one or several rigid and flexible chemical groups. By increasing the length of the flexible tail with respect to the rigid head, for instance, the *n*CB series goes from exhibiting the nematic phase to forming smectics when $n > 7$,

for example [173]. Many LC materials have been investigated in this way; it has been used to yield LCs with specifically tuned phase behaviors, in the *m*O.*n* series [174], for instance. Investigating a homologous series can elucidate the structure-property relationships in an LC system in a systematic way.

Though the TB phase was identified several years ago in bent, flexible dimer LCs [48,78], the mechanisms of its formation are still not well understood. The bent structure of the molecule appears to be necessary for the formation of the TB phase, with a number of simulations supporting this claim [59,76,122], though it is still unclear why. Several groups have investigated the macroscopic properties of various bent flexible molecules which have different bend angles [107,109] and with different lengths of the flexible alkyl-based linker (effectively changing the bend angle) [106,113,114]. But none have yet investigated the *nanostructure* of the TB phase in homologues of molecules in which the linker length is systematically varied.

In this study, we synthesize a collection of cyanobiphenyl dimers linked by a flexible alkyl linker of odd lengths n = 5 to 17, all of which form the TB phase. We characterized the thermal, optical, and nanoscale properties of each member using several characterization techniques and investigate the trends that emerge. We find that each homologue exhibits a similar trend in helix pitch as a function of temperature, with the linker number n correlating with longer pitches in general. The TB pitch extrapolated to low temperature increases approximately linearly with increasing n, while the helix pitch at high temperature increases superlinearly and appears to exhibit enhanced TB fluctuations.

The phase sequence of the homologous series is shown in Figure 4.4.1. The corresponding differential scanning calorimetry (DSC) scans are shown in Figure 4.4.2 and selected polarized light microscopy (PLM) textures in Figure 4.4.3. We find a large temperature range in the TB phase at $n = 7$ and 9. For CB7CB, the TB phase does not crystallize down to room temperature on cooling at usual cooling rates (1 – 10°C/min), and only crystallizes after several hours to several days near room temperature. For the rest of the compounds, crystallization occurs near the temperature noted on the phase diagram, although one can generally supercool the TB phase below the crystallization temperature. CB5CB is the only monotropic member of the series, with its crystal phase melting at ~130°C.

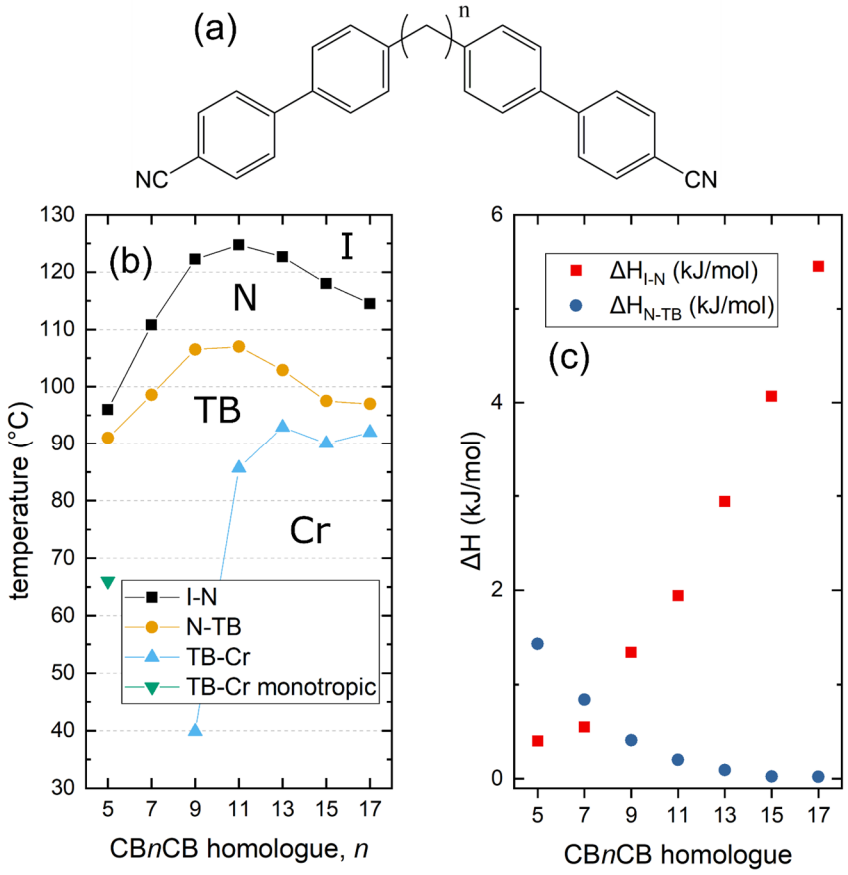

Figure 4.4.1: Molecular structure of the CB*n*CB molecules and thermodynamic behavior for *n* = 5 to 17.
(a) The odd CB*n*CB molecules are bent and the alkyl group linking the cyanobiphenyl arms contain *n* alkyl units. (b) Phase diagram of the odd CB*n*CBs as determined by differential scanning calorimetry at scanning rate 5°C/min. CB5CB exhibits a monotropic TB – Cr phase, while CB7CB did not crystallize during the DSC experiment. (c) Latent heat of transition (ΔH) in the odd CB*n*CBs. For reference, the latent heat in the I – N transition of 5CB (pentylcyanobiphenyl, similar to an arm of CB7CB) is ΔH = 23 kJ/mol.

An analysis of the phase diagram of this series (Figure 4.4.1b) can offer some insight into the molecular dynamics of the system. On increasing n from n = 5 up to n = 11, the nematic temperature range broadens, and remains almost constant for the remaining members $n \geq 11$. This provides evidence for a decoupling of the arms of the dimers which is complete for $n \geq 11$, favoring uniform alignment of the nematic over TB organization, which is evidently favoured by the more bent homologues, where n is smaller. For n = 7, the TB phase is stable over the largest temperature range, all the way down to room temperature. On increasing n, the TB range decreases dramatically, and the crystallization temperature increases. This again indicates a decreased thermodynamic stability of the TB phase with increasing n and, therefore, less bent molecules. These trends are also borne out by the observed latent heats of transition for the I – N transition, increasing with n, and for , decreasing to zero with n. (Figure 4.4.1b).

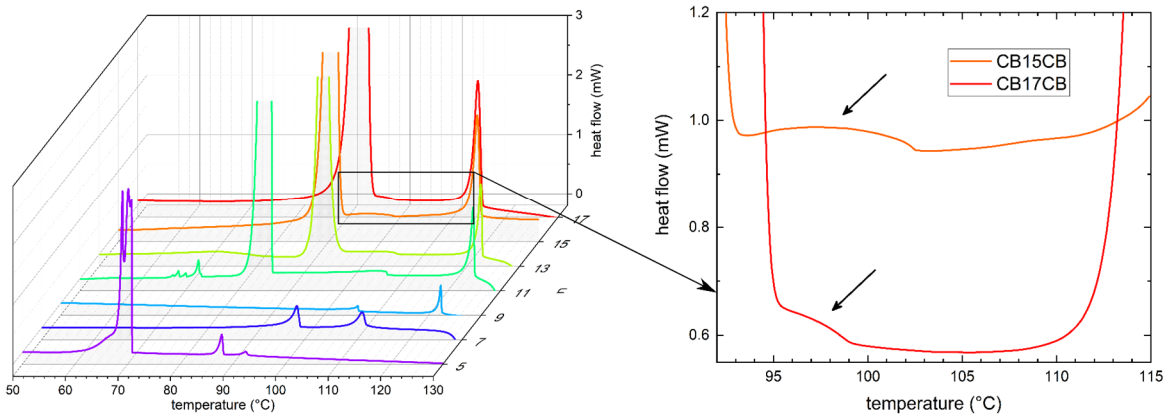

Figure 4.4.2: Differential scanning calorimetry scans of the CB*n*CB series from *n* = 5 to 17.

We performed RSoXS on the n = 7 to 17 odd homologues and obtained 2D detector images on heating for n = 7, and on cooling for n = 9 to 17 (Figure 4.4.4a). We converted the 2D detector images into 1D plots by azimuthally averaging the intensity about the beam center at $\mathbf{q}$ = 0. We then represented the temperature series of these plots as a color map of the intensity as a function of q and T. Every compound in the CBnCB series exhibits a characteristic TB pitch behavior: at

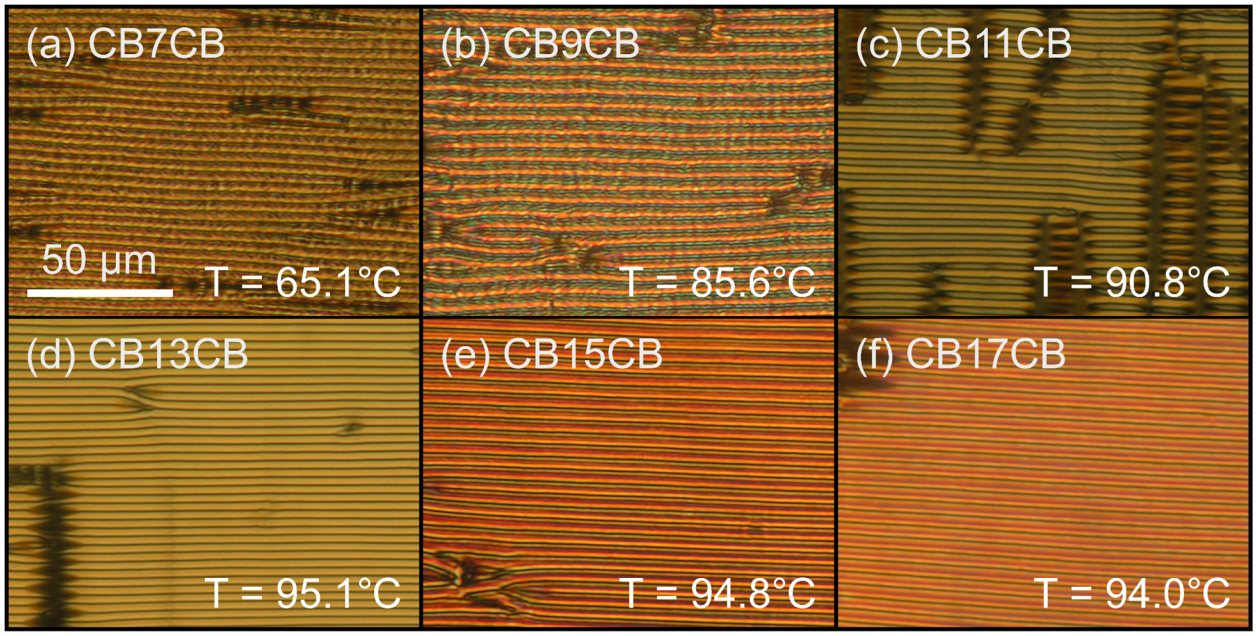

Figure 4.4.3: PLM of the CB*n*CB series in the TB phase.
Characteristic stripe texture in the members of the CB*n*CB series, n = 7 to 17 odd, in horizontally rubbed cells, with polarizers oriented vertically and horizontally along the edges of the images.

high temperature in the nematic phase, there is no resonant scattering. On cooling towards the N – TB transition, diffuse scattering at small q increases, indicating increased fluctuations in the nematic phase (as described in section 4.5). We denote this the "nematic fluctuations peak". The nematic fluctuations peak appears near the temperature at which the scattering from the TB helix occurs. We therefore declare the phase transition to occur at the temperature where the nematic fluctuations peak is maximal. Just below the N – TB transition, we observe scattering from the TB helix. On cooling in the TB phase, the scattering features shift dramatically in q at first, with this trend gradually slowing at lower temperatures. In the CB*n*CBs with $n \geq 11$, the TB phase transitions into a crystal phase, causing the scattering from the TB phase to disappear once again.

For n = 15 and 17, the helix pitch unwinds appreciably as the crystal phase grows in. The range of helix pitches displayed by the members of this series is p = 80 – 400 Å.

One trend that is immediately obvious is that the TB pitch increases with increasing n. The pitch also tends to decrease more dramatically on cooling in the homologues with greater n. In addition, the CBnCBs with $n \geq 13$ exhibit scattering which bridges with the nematic fluctuations peak. This behavior suggests an increasingly 2nd order nature in the phase transition with increasing

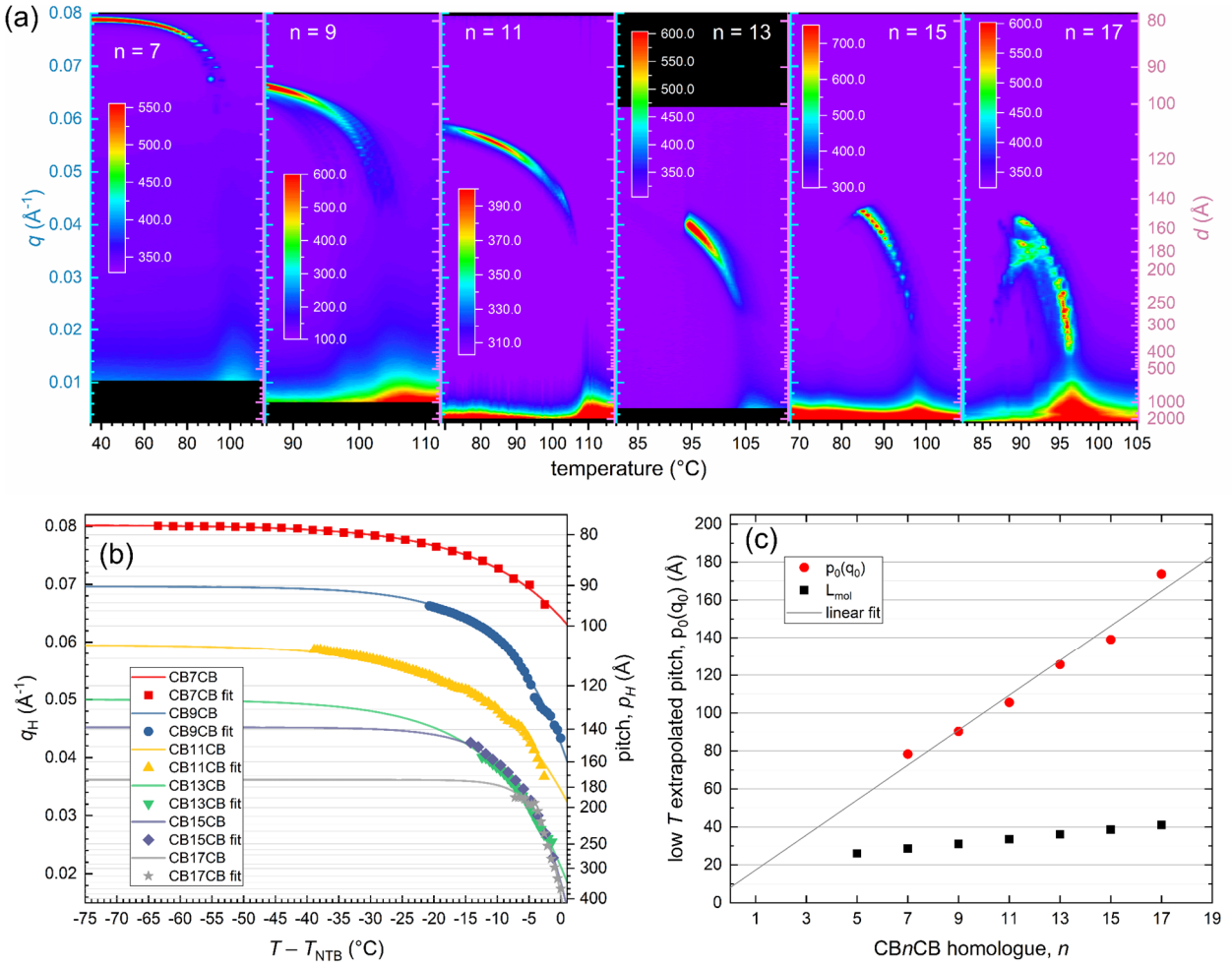

Figure 4.4.4: RSoXS experiments and analysis of the odd members of the CB*n*CB series.
(a) The plots were constructed by azimuthally averaging 2D detector images taken as a function of temperature. The scattered intensity is represented in the color scales. Regions where there are no data are black. The data for n = 7 were obtained on heating, while those for n = 9 to 17 were obtained on cooling. The q and d scales are the same in all plots. (b) The most prominent peak positions are plotted, and the temperature dependence fit with an exponential, yielding a constant offset in q which measures the TB pitch extrapolated to low temperature. (c) The low-temperature TB pitch (red) and molecular length vs. n. The low-temperature pitch increases essentially linearly with n.

n, with the corresponding nematic phase exhibiting TB fluctuations which nearly smoothly go from $p \rightarrow \infty$ to $p \rightarrow p_{TB}$(high *T*).

The color maps of the scattering from the CB*n*CB series in Figure 4.4.4a provide an average sense of the scattering from this series but does not highlight the stochastic nature of the scattering from the TB pitch at high temperatures. At high temperature in the TB phase, the entire CB*n*CB series exhibits scattering from many domains which may broaden or sharpen or disappear from the beam center over the course of only a few seconds at a given temperature. This behavior is best observed by viewing movies of detector images on cooling, which, unfortunately, cannot be reproduced here. These impressive changes appear to be manifestations of fluctuations of the TB helix. The TB fluctuations are most impressive for $n = 17$, with the nematic fluctuations peak connected in scattered intensity with the TB pitch fluctuations at times. This indicates a nearly 2nd order transition, or the proximity of a tricritical point near $n = 17$.

When we observe these compounds in unidirectionally aligned cells under the PLM, on cooling through the N – TB transition we observe the expected blocky texture, but the large blocky domains flicker and migrate perpendicular to the rubbing direction and sometimes form into primitive stripe textures. After a few seconds for *n* smaller, and possibly a few minutes for *n* larger, the texture converts back into the usual blocky texture. This behavior becomes more significant as we observe the homologues with increasing *n*. We believe this flickering and the texture transformations may be an optical manifestation of the TB helix fluctuations that we observe in RSoXS (Figure 4.4.4a). These fluctuations and 2nd order transition behaviors are an exciting avenue of exploration – a 2nd order TB transition has never been confirmed or observed in detail in RSoXS, for instance. The experimental demonstration of a 2nd order TB transition and

quantitative investigation of these fluctuations would be intriguing, especially for condensed matter theorists who study phase transitions.

We performed FFTEM on CB5CB since these measurements yield a very good measure of the low temperature pitch of the TB phase [129], while RSoXS measurements were too difficult to obtain for this material. The pitch as measured by FFTEM was $p \approx 7$ nm, in agreement with the general trend that the homologues with shorter linkers yield a shorter TB pitch.

We plot the positions of the most prominent peaks together for each material (Figure 4.4.4b). We then fit them arbitrarily to an exponential function, which provides a good fit and an extrapolation of the pitch at low temperature, as expected from measurements of $n = 7$ and 9 and as depicted in ref. [122] . The extrapolated low-temperature TB pitch is plotted in Figure 4.4.4c and is linear in n. This indicates that each members of the series approaches the same low temperature TB ground state.

We performed conventional wide-angle x-ray scattering (WAXS) on the homologues $n =$ 7 to 13 to check that the TB phase lacks lamellar ordering (as expected for the TB phase) and to determine the position of the diffuse scattering features for the purposes of developing a quantitative model of the TB nanostructure. Indeed, none of the compounds we measured exhibited lamellar ordering.

We plot the position of the diffuse WAXS feature along the TB helix corresponding to a pseudo-layer spacing s, and plot it against the half molecular length $L_{mol}/2$ in Figure 4.4.5a. $L_{mol}/2$ increases linearly with n, whereas s increases superlinearly, with the two functions crossing over near $n = 12$. We model this crossover behavior in Figure 4.4.5b. In CB7CB, the molecular ends of neighboring molecules overlap, with the central carbon of a third laterally-neighboring associating

with this overlap, creating a triple association. In CB17CB, however, the arms of the molecule separate significantly, such that there is only a pairwise association of molecular arms.

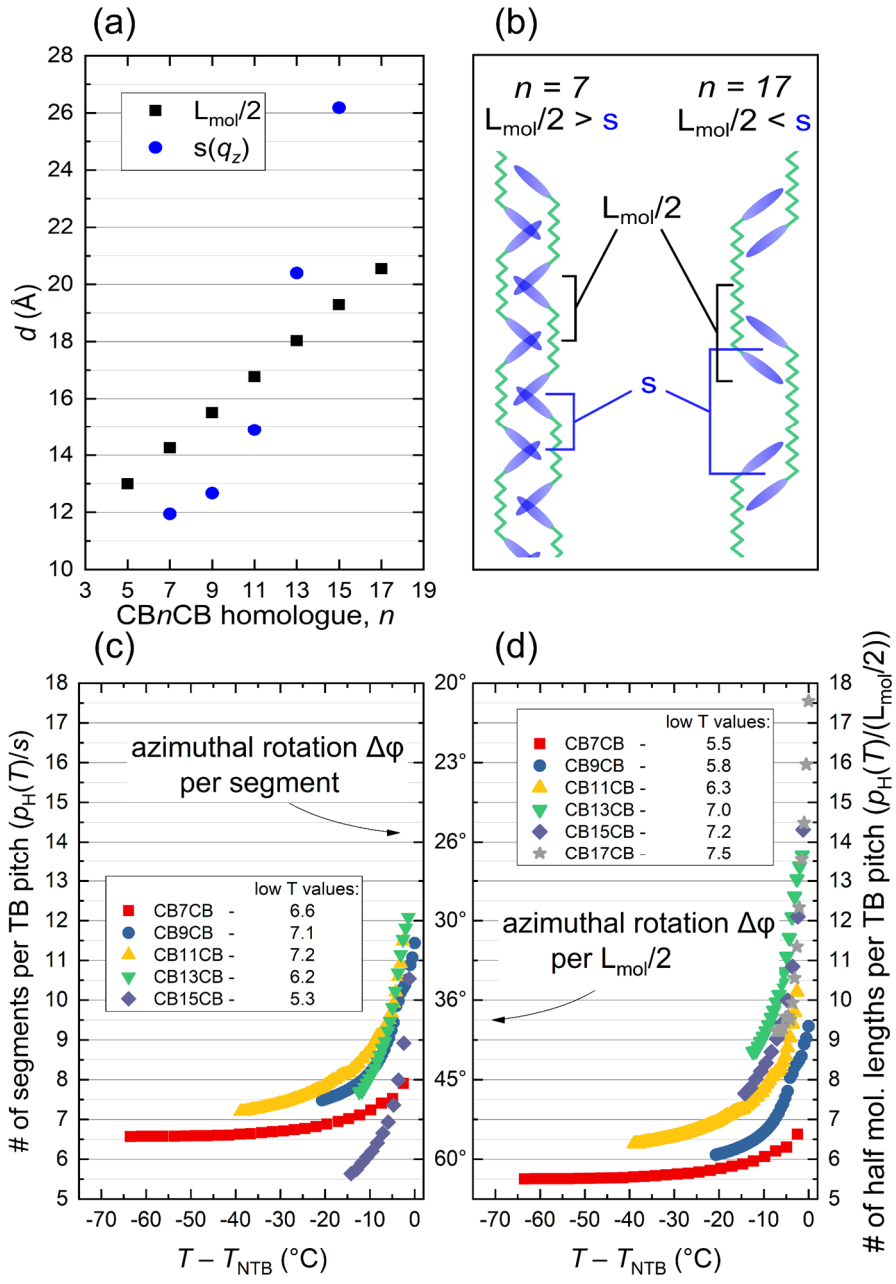

Figure 4.4.5: Segment length and L_{mol} in the CB*n*CB series.
(a) A real-space plot of segment length s and the half molecular length $L_{mol}/2$. (b) Model of the behavior in (a) to show how the segment length increases beyond the half molecular length. The number of (c) segments and (d) half molecular lengths per TB pitch p_H as a function of temperature, with the axis for azimuthal rotation $\Delta\varphi$ per unit in the middle.

We can then plot the TB pitch p_H/s and $p_H/(L_{mol}/2)$, and obtain the azimuthal rotation $\Delta\varphi$ per s (Figure 4.4.5c) and $\Delta\varphi$ per $L_{mol}/2$ (Figure 4.4.5d). These plots demonstrate that the TB phase of these molecules is composed of many pseudo-layers at high temperature, with the number reducing dramatically on cooling. Inversely, the azimuthal rotation $\Delta\varphi$ increases dramatically. This indicates that the TB helix is dynamically changing on cooling.

We performed birefringence measurements on the entire CB*n*CB series and plotted the data in Figure 4.4.6a. We then used the procedure developed by Meyer *et al*. in ref. [131] to extract an estimate of the TB cone angle as a function of temperature, shown in Figure 4.4.6b. Evidently, the cone angle is not very sensitive to *n*.

We have systematically investigated the homologous CB*n*CB series for n = 5 to 17 odd and studied its phase behavior and TB characteristics as we varied *n*. We found that increasing *n* tends to stabilize the nematic phase thermodynamically, with the TB phase becoming less stable and more prone to crystallization. The TB pitch extrapolated to low temperature increases linearly with *n* while the high temperature pitch increases superlinearly and exhibits increasingly enhanced fluctuations, evidence for an approaching tricritical point. Thus, we have a sense for how varying *n* affects the TB phase. This work can help direct the chemical synthesis of TB molecules with a desired increased TB pitch by simply increasing the spacer length, though at the expense of the TB temperature range. We also show that RSOXS can be used to observe tricriticality and 2nd order phase transitions in TB systems.

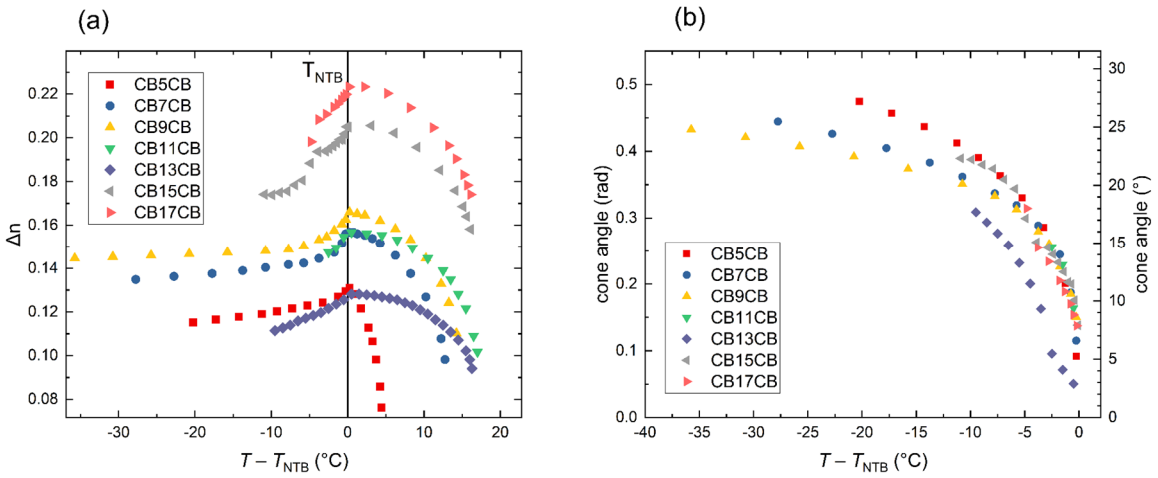

Figure 4.4.6: Birefringence and estimated TB cone angle in the CB*n*CB series.
(a) The birefringence generally increases with increasing *n*, with the notable exceptions of *n* = 11 and 13. (b) The estimated cone angle (not the true cone angle) for each member of the series does not appear to vary significantly with *n*.

4.5. NEMATIC ORIENTATION FLUCTUATIONS NEAR THE TB PHASE

Orientation fluctuations are ubiquitous features of soft materials, operative on length scales ranging from nanometers in the rotational dynamics of single molecules, to the macroscopic deformation of local orientational order in LCs, polymers, and biomaterials. Here we propose the application and unique capabilities of depolarized resonant soft x-ray scattering (RSoXS) as a specific probe of molecular orientation fluctuations at the nanoscale. This technique is demonstrated by measurement of the spectrum of the thermally generated collective (director) fluctuations in the local average molecular orientation of a nematic LC using carbon K-edge resonant scattering. The scattering reveals the elastic behavior of the nematic near the transition to the TB phase and demonstrates the existence of short-range, transient heliconical assemblies of molecules in the nematic. We develop a model for resonant x-ray scattering near the nematic – TB transition in the vein of similar treatments by de Gennes of light scattering at the nematic – SmA transition and find excellent agreement with our results.

LCs are a prototypical soft matter system composed of anisotropic molecules which collectively organize and orient in numerous ways such that they exhibit unique properties. In the nematic LC phase, this includes optical anisotropy arising from long-ranged orientational ordering. Additionally, the elastic and hydrodynamic properties of nematics give rise to such optical behavior as turbidity. Many of the elastic and hydrodynamic properties can be investigated using quasielastic light scattering experiments [175], which probe the dynamical properties of soft materials and afford such information as elastic constants and correlation lengths.

Chatelain performed the first comprehensive light scattering experiments on LCs when he irradiated the LC azoxyanisole in the nematic phase with linearly polarized light and observed a strong anisotropic scattering response [176]. Later, de Gennes showed that light scattering in the nematic was due to fluctuations in the dielectric tensor caused by orientation fluctuations of the local director at finite temperature [177]. The derivation of the fluctuation modes in the nematic phase could then be used to extract the elastic constants and correlation lengths of the material as a function of temperature. Subsequently, the Orsay group showed that one could also extract the Leslie coefficients of viscosity using light scattering experiments [178,179]. As the understanding of thermal fluctuations in materials became important for the study of renormalization group theory, light scattering experiments became widely used to investigate the nature of various phase transitions and critical behavior [180].

Probing fluctuations in molecules and nanoscale structures requires the nanoscopic sensitivity afforded by x-ray light. However, conventional x-ray scattering techniques are only sensitive to electron density modulations in samples and not to molecular orientational fluctuations. Examples of modes of molecular reorientation in LCs that do not produce electron density modulation are the helical precession of the molecular tilt direction in the chiral smectic C phase, or the alternation of molecular tilts in anticlinic and clock smectic phases [181]. In these cases, resonant x-ray scattering is an effective probe of the ordering [182], as the coupling between linearly polarized x-rays and the asymmetric electron cloud of the sample results in a tensorial atomic scattering cross-section for energies near the absorption edge [172], with the scattering contrast dependent on the orientation of the molecule with respect to the polarization direction of the x-ray beam. Recently, RSoXS at the carbon K-edge has been applied to investigate polymer

blends [183], block copolymers [66,184], organic bulk heterojunction solar cells [67] and polymeric transistors [68], helical nanofilaments [69], and the twist-bend phase [70].

In RSoXS, when constituent particles are much smaller than their fluctuations, their scattering averages into an optical birefringence-like behavior [172] which makes this technique an effective choice for investigating meso- and nano-scale fluctuations in LCs. In this study, we use RSoXS to characterize the nematic fluctuations of a TB-forming material while varying the temperature across the N (nematic) – TB phase transition. We develop a phenomenological model which describes and reproduces the behavior of these fluctuations. With this, we may extract the relationships between the nematic elastic constants and other unknown parameters.

The TB-forming LC material MDA-15-1369 (MDA, for conciseness) is a proprietary LC mixture from Merck Corporation which exhibits a room temperature TB phase and has the following phase diagram down to room temperature: Iso (62°C) N (26°C) TB. PLM experiments demonstrate that it exhibits a conventional nematic phase at high temperature which aligns well in a commercial, unidirectionally rubbed cell. On cooling into the TB phase, the nematic director fluctuations freeze out and characteristic TB stripes develop along the rubbing direction (Figure 4.5.1a). There appears to be some coexistence of the N and TB phases, even at room temperature, with a wide temperature range phase coexistence expected for LC mixtures such as MDA.

When quenched at room temperature in the TB phase, freeze-fracture transmission electron microscopy (FFTEM) measurements reveal nanometer-scale sinusoidal modulations of the

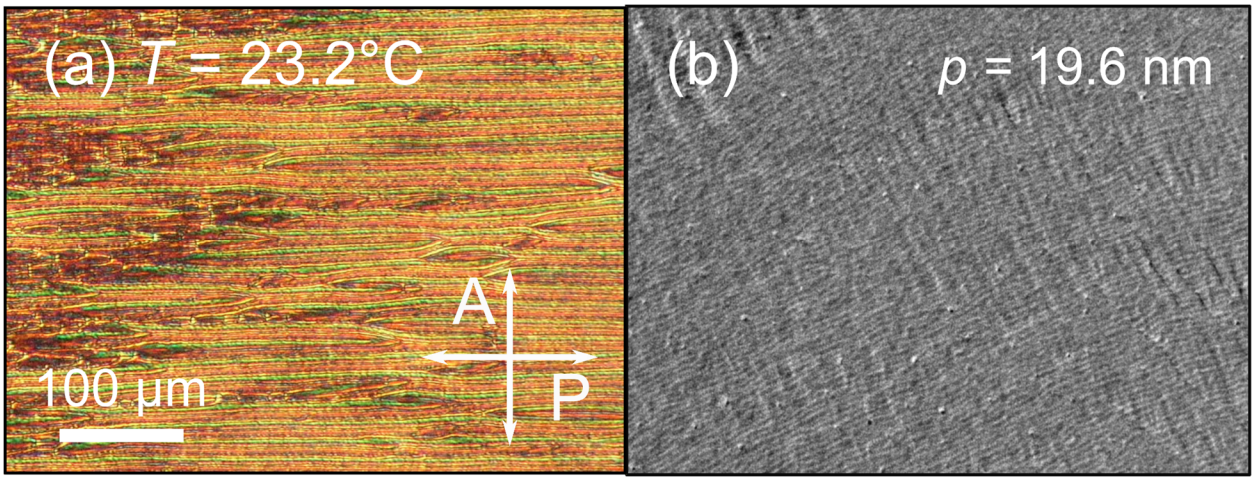

Figure 4.5.1: PLM and FFTEM characterization of MDA.
(a) PLM image of MDA in a horizontally rubbed cell, exhibiting characteristic TB stripe textures. (b) FFTEM image of MDA showing sinusoidal topographical modulations of periodicity p = 19.6 nm.

fracture surface characteristic of the TB phase [59] (Figure 4.5.1b). The most frequently observed pitch was ~20 nm, with the range of observed pitches being ~15 – 25 nm.

RSoXS has already been shown to be an excellent tool for studying the TB helix while varying temperature *in situ* [70]. We used RSoXS to investigate the nematic fluctuations of a TB-forming material because the bend elasticity becomes very small near the N – TB phase transition [84], making bend fluctuations large and giving a measurable, temperature-dependent scattering signal.

At high temperature in the nematic phase, MDA exhibits the expected elliptical small-angle scattering pattern shown in Figure 4.5.2a,b, demonstrating the different magnitudes of twist-bend and splay-bend fluctuations [177]. On cooling, the intensity at small q increases dramatically, with the scattering in the $q_\perp$ direction decreasing dramatically and making a waist in the elliptical profile (Figure 4.5.2c,d). Near room temperature, we obtained a region in the MDA sample which exhibited N – TB coexistence (Figure 4.5.2e,f). A scattering arc at $|q| \approx 0.025$ Å^{-1} comes from the TB helix ($p_{TB} \approx 25$ nm), and a diffuse, dumb-bell-shaped scattering feature corresponds to nematic

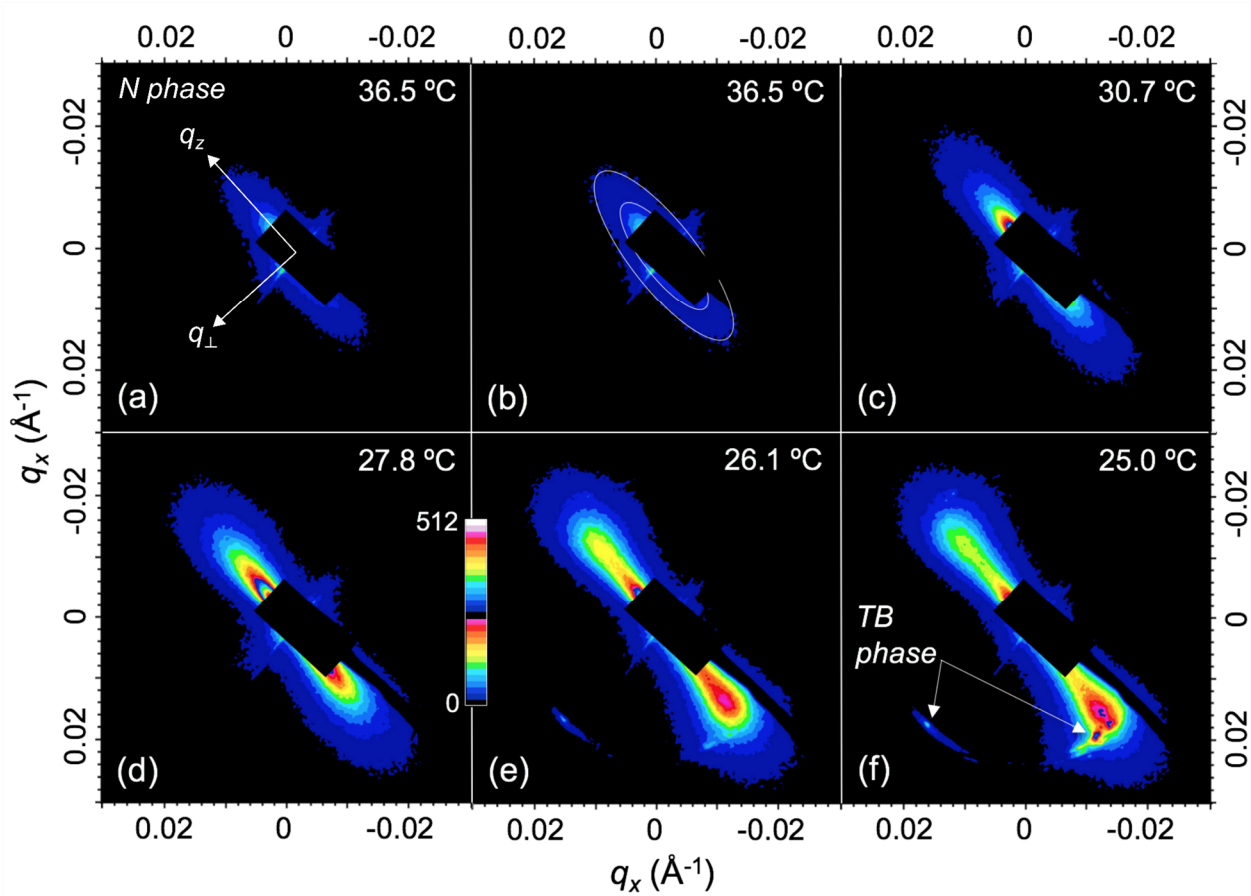

Figure 4.5.2: Smoothed RSoXS images of MDA on cooling.
At the high temperatures (a,b), the scattering pattern is elliptical, as we expect from a conventional nematic phase. As we cool further and approach the TB phase (c), the bend elastic constant becomes very small, causing large fluctuations of the nematic director, evident in the increasing size of the elliptical scattering at small q. (d) The small-angle region develops a dumb-bell shape, indicating the departure from conventional nematic director fluctuations and the influence of the TB nature. Near room temperature (e,f), the nematic fluctuations coming from the dumb-bell shaped scattering transitions into TB domains as a distinct peak appearing at the edge and perpendicular to the dumb-bell.

orientation fluctuations of the splay-bend mode. Because the bend elastic constant is small with respect to the other elastic constants for TB-forming materials [84], the most pronounced fluctuations in the scattering correspond to the bend. For our sample-detector geometry, the bend fluctuations appear as scattering along the q_z axis [177], or the helix axis (along the length of the dumb-bell), so that the scattering peak near the lower portion of the dumb-bell corresponds to the TB domain forming from the nematic domain which is producing the orientational fluctuations.

When we take a radial line scan along q_z from the beam center toward the lower portion of the dumb-bell-shaped scattering, we obtain the colored points in Figure 4.5.3a. We normalize this scattering by that expected from the orientation fluctuations (intensity $\propto q_z^2$), isolating the contribution of the growth of the TB helix in the scattering (Figure 4.5.3b). The fits to these curves are provided by a simple theoretical model that we developed to explain this behavior, the description of which follows.

Using the methodology of de Gennes, we outline a model for the orientation fluctuations near the N – TB phase transition by modifying the Frank elastic free energy for a nematic to include terms which describe the TB phase. The director field $\hat{\boldsymbol{n}}$ of the TB phase is given by

$$\hat{\boldsymbol{n}} = \hat{\boldsymbol{x}} n_\perp \cos \boldsymbol{q} \cdot \boldsymbol{r} + \hat{\boldsymbol{y}} n_\perp \sin \boldsymbol{q} \cdot \boldsymbol{r} + \hat{\boldsymbol{z}} n_\parallel, \tag{1}$$

where $\hat{\boldsymbol{z}}$ is along the helix direction, $\hat{\boldsymbol{x}}$ and $\hat{\boldsymbol{y}}$ are perpendicular to $\hat{\boldsymbol{z}}$, $n_\perp$ is the component of the director perpendicular to the helix axis, and $n_\parallel$ is parallel. The free energy density for the nematic phase of a TB-forming material includes the Frank elastic free energy density of a nematic and additional terms which take into account the polarization of the molecules and the flexoelectric coupling [137]. We account for the energetic preference for a finite wavevector, orientationally modulated state that leads to the spontaneous chiral symmetry breaking of the TB by introducing

a dispersion minimum in polarization elasticity at finite q_0. The free energy f_0 of this system is then given by

$$f_0 = \frac{1}{2}K_S\boldsymbol{S}^2 + \frac{1}{2}K_T\boldsymbol{T}^2 + \frac{1}{2}K_B\boldsymbol{B}^2 + \frac{1}{2}[A + B({q_z}^2 - {q_0}^2)^2)]p(q)^2 - C\boldsymbol{B}\cdot p(q), \qquad (2)$$

where K_i are the splay, twist, and bend elastic constants respectively, $\boldsymbol{S} = \nabla\cdot\hat{\boldsymbol{n}}$, $\boldsymbol{T} = \hat{\boldsymbol{n}}\cdot(\nabla\times\hat{\boldsymbol{n}})$, $\boldsymbol{B} = \nabla\times(\nabla\times\hat{\boldsymbol{n}})$, p is the polarization, and A, B, and C are coefficients to be determined experimentally.

In our scattering geometry, we are primarily probing the bend fluctuations of the director. Introducing fluctuations in the order parameter and focusing on the bend contributions to the free energy, to lowest nontrivial order we find

$$f_{fluc} = f - f_0 = \frac{1}{2}\{K_B{q_z}^2\delta{n_{qz}}^2 + [A + B({q_z}^2 - {q_0}^2)^2]|p(q)|^2\} - Cp(iq_z\delta n). \qquad (3)$$

Minimizing the free energy of the fluctuations with respect to p yields

$$p_{min} = \frac{C(iq_z\delta n)}{A\big(1 + H(q_z)\big)} \qquad (4)$$

where

$$H(q_z) = \xi^4({q_z}^2 - {q_0}^2)^2 = (B/A)({q_z}^2 - {q_0}^2)^2 \qquad (5)$$

Now we analyze the Fourier modes of the fluctuations after the manner of de Gennes [177]. Solving for the thermal average of the mean-squared fluctuations and using the equipartition theorem, we find

$$\langle{\delta n_{qz}}^2\rangle = \frac{k_BT}{K_B{q_z}^2}\left(\frac{1 + H(q_z)}{K_{Beff}/K_B + H(q_z)}\right) \qquad (6)$$

where

$$(K_{Beff}/K_B) = 1 - \frac{C^2(T)}{\mathrm{A}} \qquad (7)$$

This model, which has three free parameters: A, B, and C, is used to fit the line shape of the nematic fluctuations in the RSoXS. Figure 4.5.3a shows fits to the data of q_z from Figure 4.5.2. The fits exhibit the expected $1/{q_z}^2$ scattering along with the development of the scattering peak from the TB helix. When we plot $\langle \delta {n_{qz}}^2 \rangle * {q_z}^2/A$, we can see the contribution to the scattering from the TB helix growth alone (Figure 4.5.3b). This demonstrates that a relatively simple mean field treatment can explain the complex behavior that we observe at the N – TB phase transition.

Here, we demonstrated the efficacy of using RSoXS to examine nematic orientational fluctuations. We developed a phenomenological model which fits the profile of the diffuse scattering from these fluctuations, permitting us to extract various material parameters from a TB-forming LC, including the ratios between elastic constants, the orientation correlation length, and the flexoelectric coefficient. This methodology will be useful for investigating the orientation fluctuations of any soft material with orientational ordering, such as anisotropic colloids and fluid DNA fibers.

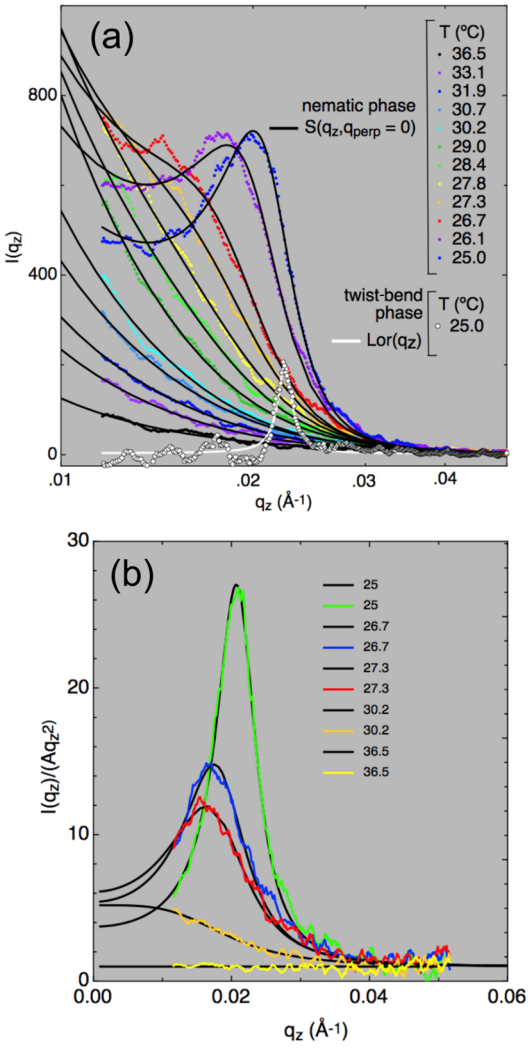

Figure 4.5.3: Fits of the nematic fluctuations features in the RSoXS data to our continuum elastic model.
(a) Line profiles taken from the beam center along the length of the upper portion (q_z) of the dumb bell at different temperatures and fits to their profiles obtained from the theoretical model. (b) Contribution of the TB helix development to the scattering, attained by factoring out the contributions from the nematic fluctuations in (a) by $1/{q_z}^2$.

4.6. THE BLUE AND TB PHASES OF MIXTURES OF CB7CB WITH THE ROD-LIKE CHIRAL DOPANT CB15

We studied the phase behavior of binary mixtures of the TB-forming LC CB7CB with the rod-like chiral dopant CB15. In mixtures with low concentrations of CB15, we observe cholesteric and TB phases on cooling from the isotropic. At higher concentrations of CB15, a unique LC phase with many characteristics of a classical blue phase appears below the isotropic phase, which we dub BP*. This phase persists over a ~15 – 30 K temperature range, with the range tunable with the concentration of CB15. Freeze-fracture transmission electron microscopy (FFTEM) images in the TB phase demonstrate periodic modulations in the surface topography, a signature of the TB nematic phase. Resonant soft x-ray scattering (RSoXS) experiments are used to measure the temperature dependence of the pitch in the TB phase. No resonant scattering is observed in the temperature range of the BP* phase.

Since the TB phase was first theoretically postulated [74–76] and subsequently identified in experiments [48,59,70,85], it has garnered much attention from the LC community. In the conventional nematic phase, anisotropic molecules are positionally disordered but have long-ranged orientational ordering. The TB phase is a nematic variant consisting of flexible organic molecules which, because of their molecular shape, favor a nematic director field with macroscopic bend. This stabilizes twist and bend nematic deformations, giving the structure of the TB phase, a positionally disordered fluid with molecules helically precessing about a helix axis **z** such that their orientations are fixed on the surface of a cone with cone angle θ and with a helical pitch p generally only a few times the length of the molecule [59,70,85]. This helical director

configuration is borne out of spontaneous reflection symmetry breaking from the nematic phase, leading to conglomerate domains in a sample consisting entirely of achiral molecules.

The ability to induce a twist with only one handedness in the TB phase is essential for its application in such chiral technologies as asymmetric chiral synthesis and chiral separations [185–188]. TB materials could even be utilized as chiral transport media for nanoscale objects which are sensitive to a fluid nanochiral environment. There have been attempts to induce enantiomeric excess in sample of the TB phase by introducing a chiral dopant [94,189] or by synthesizing a chiral molecule that forms the TB phase [93], though more conclusive evidence is necessary for such claims of homochirality. Understanding the factors that contribute to controlling the handedness of the TB phase may very well lead to a deeper understanding of the nature of the phase itself.

A common way to obtain chiral LC phases is to mix an achiral LC with a suitable chiral dopant. When doping an achiral nematic phase with a small amount of chiral dopant, one generally obtains a cholesteric (section 1.1.2). In some cases, adding more chiral dopant can stabilize one or more of a number of blue phases, consisting of so-called double-twist cylinders in which the nematic director field twists in two dimensions about a single axis (section 1.1.3). These double-twist cylinders then self-assemble and form a 3D lattice of cylinders and an accompanying lattice of defects with a lattice parameter on the order of several hundred nanometers. Bragg scattering from this lattice generally yields blue and green colors which are visible to the naked eye, leading to the name ‘blue phase’. The blue phases typically only persist over a temperature range of <1°C [26]. However, in mixtures of bent, flexible molecules with chiral dopants, the blue phases can be stabilized over many tens of degrees Celcius [190]. Several techniques for stabilizing the blue phases have been developed, including stabilizing the defect structure of the blue phases with

photo cross-linked polymers [191] and nanoparticles [192,193]. The addition of an achiral, rigid bent-core mesogen has been shown to induce the blue phases in a cholesteric LC mixture [194]. This was attributed to a possible softening of the saddle-splay elasticity which tends to favor the formation of the blue phases. Several studies claim to have observed a blue phase in chiral TB systems [93] and in mixtures of achiral, TB-forming molecules with a chiral dopant [94]. A theoretical and computational simulation suggests that bent flexible molecules themselves could form novel blue phases with polar order [195]. This seems plausible given that the TB phase exhibits local twist akin to a double-twist cylinder.

We were motivated to study mixtures of CB7CB and the chiral LC dopant CB15 (molecular structures shown in Figure 4.6.1) in the hopes of inducing a homochiral TB sample – with a single sign of helical twist. We chose to use CB15 as a chiral dopant because of its structural similarity to a molecular arm of CB7CB, promising excellent miscibility of the components. This chiral induction could manifest as a lack of conglomerate domains or a significant change in the TB helix pitch with respect to a similar mixture of CB7CB with the achiral rod-like LC 5CB [128], measurable with various probes of nanoscale structure. In our experiments, we find no clear evidence of such chiral induction. This indicates either some degree of nanoscale immiscibility and nanophase segregation in the TB structures, or simply a lack of strong enough chiral induction. However, we do observe an LC phase with properties characteristic of the blue phases, though it is also distinct from them in several ways. This may point to some novel structural motifs which originate from the unique nature of the TB phase. In addition, when the concentration of the chiral dopant is large enough, the BP* phase exhibits a very wide temperature range – up to 30°C in the mixtures that we studied.

We determined the mesophases of the *x*% CB15/CB7CB mixtures (where *x* is the weight percent of CB15 mixed into CB7CB) using a combination of PLM and differential scanning calorimetry. The binary phase diagram in temperature and concentration is shown in Figure 4.6.1. All the mixtures studied herein were miscible at all studied temperatures and concentrations, with no evidence of macroscopic phase separation. Neat CB7CB exhibits an isotropic (Iso) – nematic (N) transition at 111°C, followed by an N – TB transition at 99°C. In a mixture of 1% CB15 in CB7CB, the isotropic phase is followed by a cholesteric phase. On the transition from the cholesteric phase to the TB, we observe an unwinding of the cholesteric helix, likely due to the divergence of the twist elastic constant at the transition to the TB phase, in analogy to a N* – SmA transition. In addition, the cholesteric must unwind to accommodate the subsequent alignment of the TB helix axis along the rubbing direction, which appears to be a strong preference.

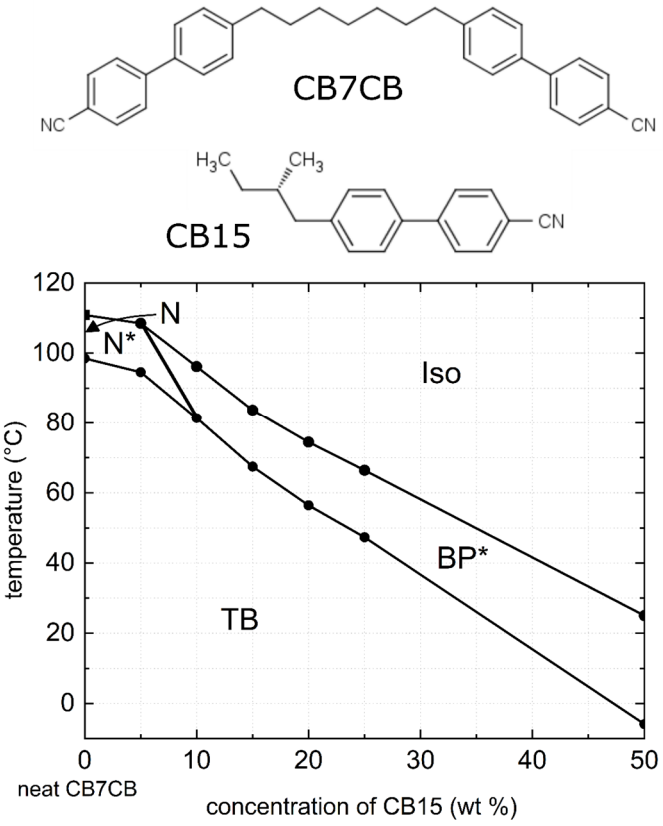

Figure 4.6.1: Molecular structures of CB7CB and CB15 and a binary phase diagram of their mixtures. Neat CB7CB exhibits an Iso – N transition and an N – TB transition on cooling from high temperature. At low CB15 concentrations, the mixture exhibits a cholesteric phase rather than a nematic, as we expect when doping an achiral nematic phase with a chiral dopant. On further cooling, this is then followed by a usual TB phase. At higher CB15 concentrations (>10%), the high temperature LC phase becomes the BP* phase, which is optically isotropic and optically active. At lower temperatures, the BP* transitions the TB phase.

On cooling a 25% CB15 mixture from the isotropic phase, we observe an LC phase which is reminiscent of a classical blue phase (Figure 4.6.2a), characterized by optical isotropy (no detectable birefringence) and strong optical rotation of light, implicating the presence of a chiral superstructure. The addition of a strong chiral dopant to a cholesteric phase increases the twisting power and can cause it to evolve into a blue phase [34]. However, the texture of the phase in our mixtures is composed of small, grainy, blue and green domains of size $\lesssim$1 μm. These domains do not grow any larger, even at the very slow cooling rate of 0.01 °C/min, in contrast to the classical blue phases I and II in which slow cooling often yields large (~100 μm), faceted crystallites [15]. This phase is also unlike the classical blue phase III (otherwise known as the blue fog phase), which exhibits only a dim, diffuse blue color due to diffuse Bragg scattering [15]. After comparing this optical texture to that of other known blue phases, including the more exotic smectic blue phases [36,196,197], we conclude that this blue phase is unique. This phase may be a variation of the classical blue phases I or II with some unusual, self-limiting domain growth or it may represent an entirely different molecular organization based on a TB or polarization-modulated motif [195].

At concentrations of CB15 below <15%, the textures of the TB phase of the mixtures observe in PLM appear nearly identical to those exhibited by neat CB7CB. At higher concentrations of CB15, the TB phase takes on a notably distinctive character and texture. In a 25% CB15/CB7CB mixture, for example, the TB phase forms directly out of the BP* phase as a collection of elongated domains many tens of microns wide and ~100 μm long in a unidirectionally rubbed cell (Figure 4.6.2b). These domains align with their long axes oriented at large angles with respect to the rubbing direction. In some cases, this angle is 63 – 68° clockwise with respect to the rubbing, and in other domains this angle is 163 – 168°. The behavior appears to be a kind of surface electroclinic effect, with domains of different handedness tilting at different angles with

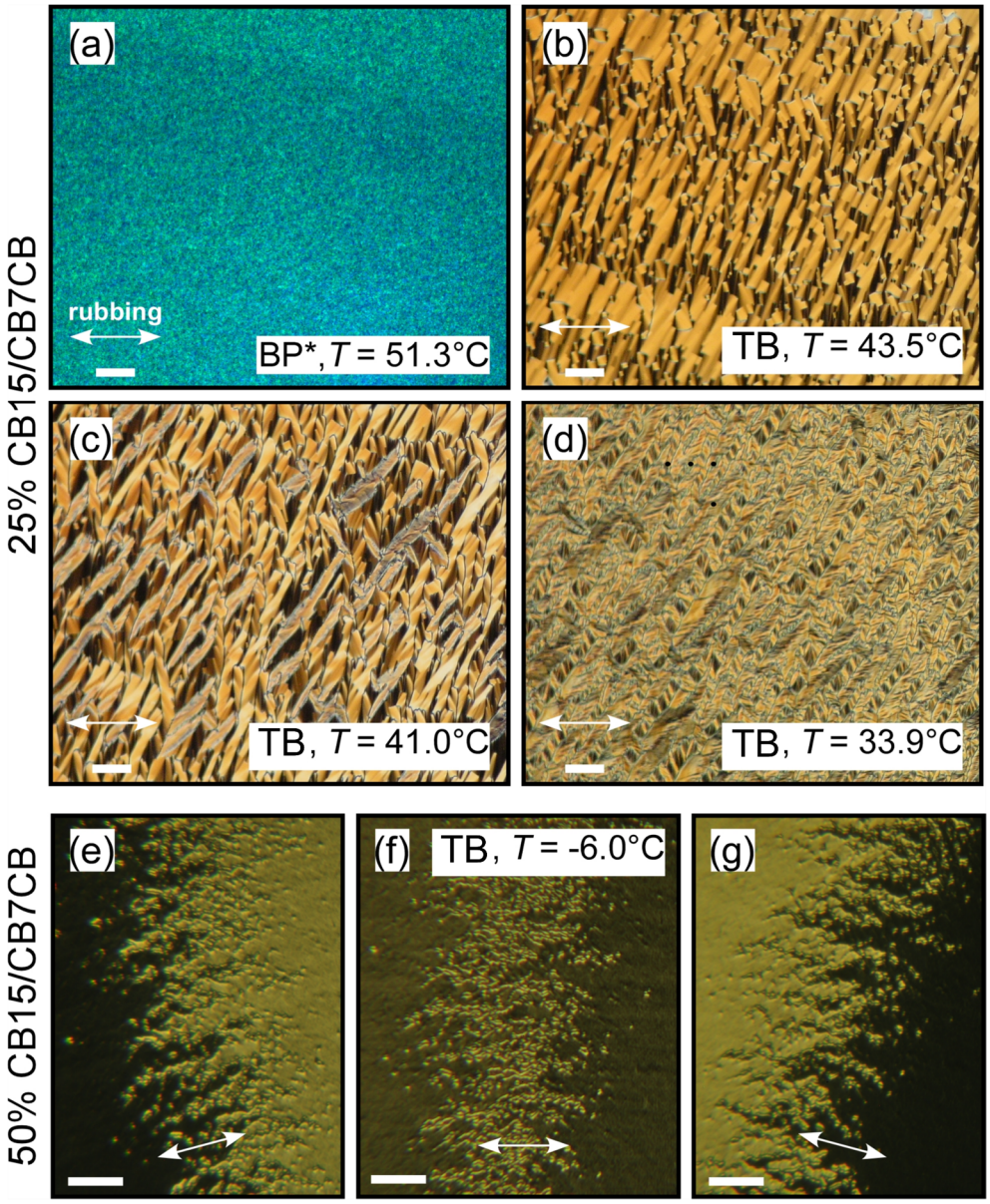

Figure 4.6.2: Polarized light microscopy images of 25% and 50% CB15/CB7CB mixtures. (a) Texture of the 25% CB15/CB7CB mixture in the BP* phase. This phase is optically isotropic and optically active like conventional blue phases. The texture consists of ≲1 μm blue and green grainy domains, with the blue-green color visible even to the naked eye. (b) On cooling into the TB phase, TB domains form out of the BP* texture, tending to align at an angle with respect to the horizontal alignment direction. (c) Several degrees further below the transition, the TB phase becomes significantly more textured and the alignment directions of the long domains shift, the mature texture setting in at low temperature (d). (f) The TB phase of the 50% CB15/CB7CB mixture appears very nematic-like, with weak director fluctuations visible and apparently uniform birefringence. On rotating the sample counterclockwise (e) and clockwise (g) by 15°, however, large (>100 μm) domains separated by a grainy boundary alternate from bright to dark, indicating that the macroscopically uniaxial domains are aligned at an angle with respect to the rubbing, but with opposite sign. This implies a segregation based on structural differences within the domains, the most likely of which is the handedness of the TB domains. The scale bars in (a-d) are 50 μm, and the scale bars in (e-g) are 100 μm. Crossed polarizers are oriented vertically and horizontally in these images. I enhanced the contrast in (a) to emphasize the distinct coloration in each grainy domain.

respect to the rubbing direction [198,199]. The alignment of achiral LCs on a chiral surface has produced substantial orientation angles [200], but the alignment of an LC with a chiral superstructure at an angle with respect to an achiral linear orientational bias has not been thoroughly investigated, having only been observed in neat CB7CB [131] to our knowledge, though not to the degree that we observe it here. The asymmetry in the rotation angles of the TB domains is a mystery. However, we find this behavior to be evidence of a lack of, or at least incomplete, chiral induction by the CB15 in the TB helical superstructure.

On further cooling into the TB phase, new elongated domains form over the previous ones (Figure 4.6.2c). These domains have a much 'rougher' texture, and they are oriented at somewhat smaller angles with respect to the previous domains (45 – 60° clockwise and anticlockwise from the rubbing direction). We attribute this new texture not to a new phase, but a visual manifestation of the CB7CB undulation instability that occurs when the TB pitch decreases cooling [87,89]. Our DSC and other experimental measurements indicate no evidence for an additional phase transition in this temperature range. Near room temperature, the mature texture fills the cell (Figure 4.6.2d).

On heating the 25% CB15/CB7CB mixture from room temperature at 0.5°C/min, it transitions directly into a cholesteric phase at 50°C, with selective reflection colors and oily streaks in a planar-aligned cell. On further heating, the mixture transitions to the BP* phase at ~70°C, followed by the isotropic phase several degrees C higher. Interestingly, on cooling while in the cholesteric phase at the higher end of its temperature range, the BP* phase can form and persist in two-phase coexistence with the cholesteric until the usual BP* – TB transition temperature.

We performed optical spectroscopy on the mixtures in order to determine their spectra and investigate the nature of the BP* phase. The normalized reflection optical spectra of a 25% CB15/CB7CB mixture at several different temperatures are shown in Figure 4.6.3. The reflectance

is calculated from the transmitted intensity normalized to 1.0 as measured well into the isotropic phase of the mixture. On cooling into the BP* phase, we observe a shoulder in the reflectance at small wavelengths which broadens on further cooling. This feature has the effect of producing a blue-green color in the cell. The classical blue phases exhibit relatively sharp optical Bragg scattering peaks corresponding to their lattice structure and reflection color(s) [39,40]. However, this shoulder never forms a Bragg scattering peak. On transition to the TB phase, the reflectance increases dramatically at large wavelengths. The spectra imply that we are not observing a classical blue phase with well-defined Bragg scattering peaks but a blue phase variant or possibly a distinct LC phase.

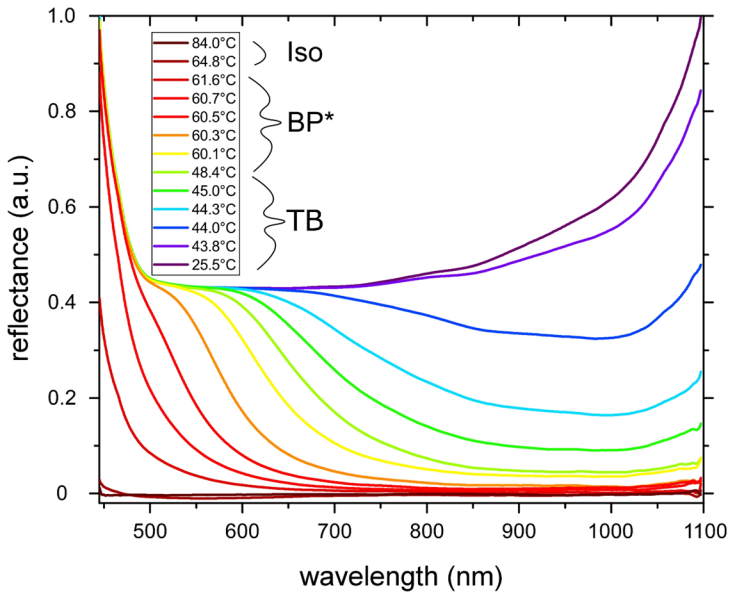

Figure 4.6.3: Reflection mode optical spectroscopy of a 25% CB15/CB7CB mixture
We filled the mixture into an untreated glass cell of thickness 23 µm, placed it into the optical path of the spectrometer. The reflectance is calculated from the transmitted intensity normalized to 1.0 as measured in the isotropic phase of the mixture at 84.0°C. On cooling, a shoulder develops at smaller wavelength and becomes broader on further cooling into the BP* phase. On further cooling to 48.4°C, the reflectance at higher wavelength increases dramatically, while the reflectance at lower wavelength does not change. These plots were smoothed by adjacent averaging over 100 points to remove noise from the data.

In order to study the nanostructure of the TB phase, we performed FFTEM and RSoXS measurements on a 25% CB15/CB7CB mixture. FFTEM images of samples quenched at several different temperatures in the TB phase exhibited sinusoidal topographic modulations in the fracture surface typical of the TB phase of CB7CB [59,85] (Figure 4.6.5a). We use a statistical method to analyze the observed periodicities in the FFTEM images [128] (see section 4.9.2). We show a histogram

distribution of the measured periodicities for 25% CB15/CB7CB in Figure 4.6.4b. Quenching 1°C below the BP* – TB transition temperature, we see a somewhat broad, skewed peak in the distribution with the maximum value at ~8.4 nm. Quenching 6°C below the BP* – TB transition temperature, we find a very broad distribution of periodicities from ~7 – 13 nm with no clear peaks. Quenching 21°C below the BP* – TB transition temperature, we observe a relatively well-localized peak in the measured periodicities centered at ~8.4 nm. The appearance of the 8.4 nm peak at higher temperatures is likely a manifestation of the FFTEM quenching process, in which some TB domains relax to the ground state pitch found at low tempeartures, in this case ~8.4 nm. The breadth of the distributions is a consequence of a number of factors, including a combination of real TB pitch variation at high temperature due to enhanced fluctuations, and the geometric effects described in section 4.9.1. The behavior that we see in Figure 4.6.5b is expected based on RSoXS measurements of neat CB7CB [70], in which the pitch distribution broadens on increasing temperature, then tightens somewhat very near the N – TB transition when many of the TB domains have melted (Figure 4.9.3). On comparing the expected periodicity of 25% CB15/CB7CB with that of 25% *5CB*/CB7CB [128], we find that both mixtures exhibit a peak at ~8.4 nm at low temperature. In this case, FFTEM indicates that the addition of the chiral CB15 plays no role in significantly altering the nanostructure of the TB phase as compared to the addition of 5CB at 25%.

We performed RSoXS experiments on a 25% CB15/CB7CB mixture to measure the TB pitch directly and shed some light on the structure of the higher temperature BP* phase. We scanned the incident x-ray photon beam energy about the carbon K-edge after discovering a scattering arc to confirm that the scattering was indeed resonant in nature. Figure 4.6.5 contains the results of an azimuthal averaging in q of 2D diffraction images on heating, cooling, and reheating a 25% CB15/CB7CB mixture. The sample had been heated to the isotropic phase for several minutes while the cell was being constructed, then subsequently quickly removed from the heat and maintained at room temperature until the measurement was taken ~12 hours later. At room temperature, we observed a relatively sharp scattering arc in the 2D images at $q \sim 0.07$ Å^{-1}

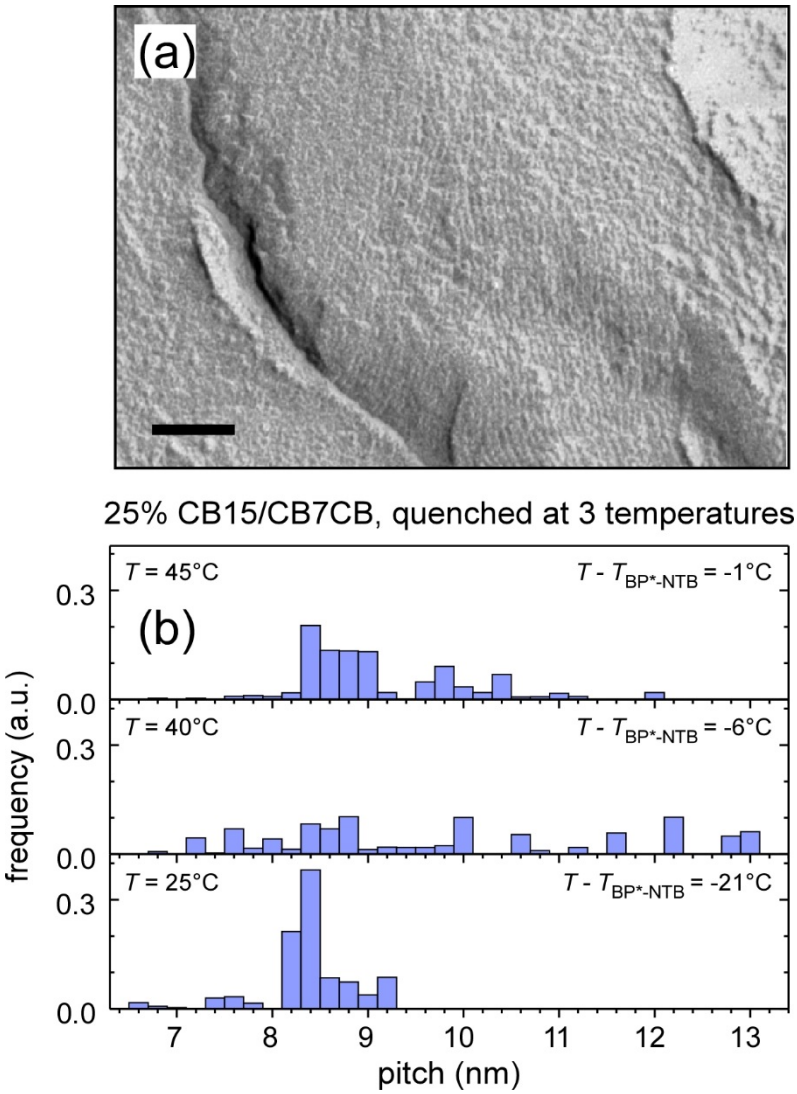

Figure 4.6.4: FFTEM image of a 25% CB15/CB7CB mixture and a histogram distribution of measured periodicities at several quenching temperatures in the TB phase. (a) The FFTEM images exhibited periodic topographical modulations in the replica which are indistinguishable from those observed for CB7CB and its mixtures with 5CB, implying that the TB helix structure is essentially unchanged on doping CB15 with respect to doping with 5CB. (b) Histograms of the measured periodicities of the mixture at three temperatures. The broad peak at ~8.4 nm in the distribution of periodicities seen at 45°C is also exhibited down to 25°C. At T = 40°C, however, the distribution is broad, as we would expect for a TB phase of CB7CB and its mixtures near the TB transition temperature. At T = 25°C, the peak at ~8.4 nm is sharper. The 8.4 nm peak here is also present in the 25% 5CB/CB7CB (Figure 4.9.7), indicating that the TB helix pitch is not altered measurably by the chiral dopant CB15.

($p \sim 9$ nm). The arc migrated toward smaller q as the cell was heated, with the peak area decreasing continuously with temperature. The scattering disappeared at 41.2°C but reappeared after heating up to 53.9°C and waiting several minutes, presumably when the BP* forms from the cholesteric phase. The scattering peak was observed at $q \sim 0.045$ Å^{-1}, or $p \sim 14$ nm, which is a significantly larger pitch than was observed in 25% 5CB/CB7CB or any other mixtures of 5CB with CB7CB measured with RSoXS ($p \lesssim 12$ nm) [128]. On cooling from this point, we observed the scattering peak area increase at fixed q, after which it remained relatively constant while the peak position shifted to larger q. The scattering arc returned to nearly the same position as on initial heating when the sample was cooled to 35.4°C. On reheating, the scattering arc followed nearly the same behavior as on the cooling run. However, at ~40°C the arc began to develop multiple peaks and to decrease in intensity. Even on heating up to 58°C this time, a very diffuse scattering was present but with an intensity that was only barely detectable. Comparing these results to a 25% 5CB/CB7CB mixture ([129], section 4.3) yields similar conclusions as those obtained by FFTEM: 20°C below the N – TB transition, 25% 5CB/CB7CB exhibits a pitch ~8.8 nm, whereas 20°C below the BP* – TB transition, 25% CB15/CB7CB exhibits a pitch of ~9.0 nm. The pitch of the 25% 5CB/CB7CB mixtures reaches ~8.5 nm at room temperature as measured by RSoXS, and the FFTEM of 25% CB15/CB7CB shows that the 25% CB15/CB7CB mixture exhibits a quenched TB pitch equal to ~8.4 nm. The FFTEM measurement implies that cooling the 25% CB15/CB7CB mixture below room temperature would cause the pitch to continue decreasing until reached ~8.4 nm. This behavior indicated a very good agreement between the two experimental methods which implies that the 25% CB15/CB7CB mixture exhibits no distinguishable nanoscale structural

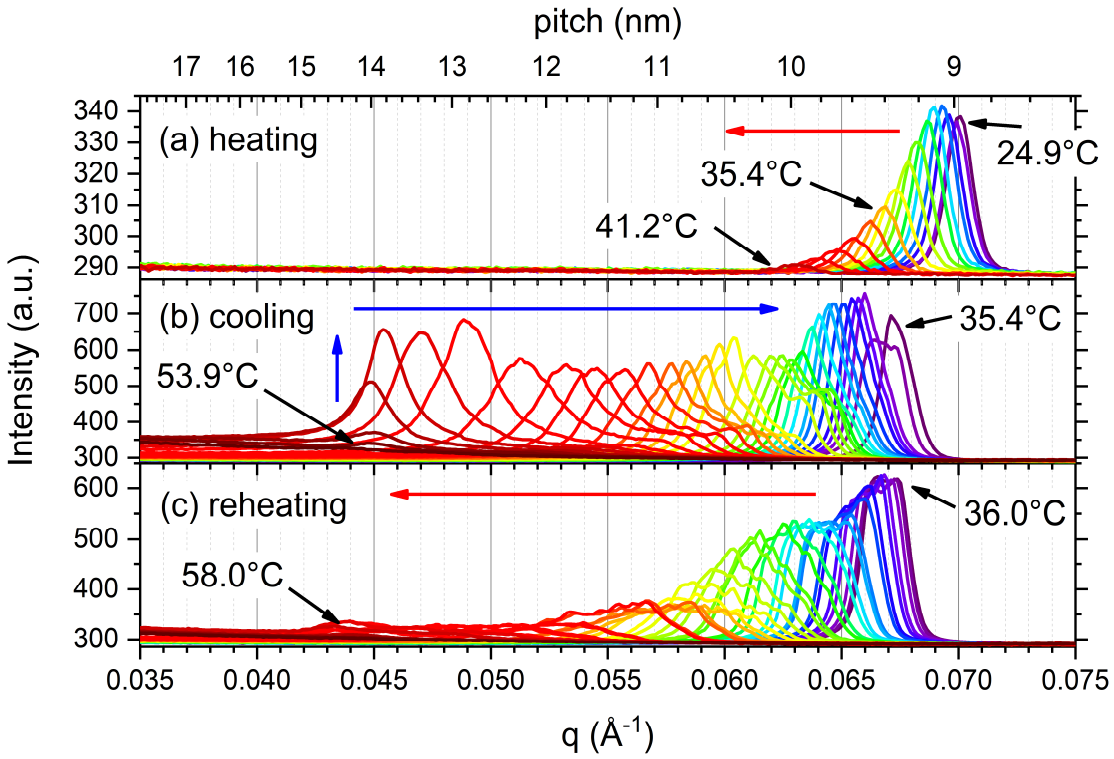

Figure 4.6.5: RSoXS observed on heating, cooling, and re-heating a 25% CB15/CB7CB mixture. 1D plots of 2D detector images created by azimuthally averaging them to find the magnitude of *q*. (a) At room temperature in the TB phase, we observe a peak corresponding to scattering from the TB helix. On heating, the peak shifts to smaller *q*, as is the trend for neat CB7CB. On approaching the cholesteric – TB transition from below, the intensity of the scattering decreases smoothly, until it is nearly undetectable at ~41°C. (b) We observed scattering on maintaining the temperature at 54°C. On subsequent cooling, the scattering peak became more intense, then shifted to larger *q*. (c) On subsequent reheating, the scattering peak decreased more slowly than the initial heating. Up to 58°C, we observed some extremely diffuse scattering.

difference from the 25% 5CB/CB7CB mixture. This indicates, again, that the molecular chirality of CB15 is not appreciably coupling to the structural chirality of the TB helix or influencing its structure.

The scattering that we observe on cooling appears well into the higher temperature phase of the 25% CB15/CB7CB mixture. On heating, we would presumably observe no scattering in the cholesteric phase in this *q*-range. Permitting the mixture to settle at ~54°C for several minutes apparently encouraged the growth of the BP* or TB phase from the cholesteric. However, it is difficult to image how a ~10 nm orientational modulation in the BP* phase would produce the

strong optical activity observed in the PLM by uncrossing the polarizers, as the optical rotation is proportional to p^3/λ^4 for $\lambda \gg p$ and would contribute virtually negligibly to the observed intensity in the optical regime [201]. It is not clear that a blue phase-like nanoscale configuration like those described in ref. [195] would give the optical properties that we observe in the PLM either. At the moment, it appears more likely that we are observing the TB phase at high temperature where the cholesteric presumably resides, the appearance of which we cannot explain at present. It is difficult to determine the nature of this BP* phase, but we can say with some certainty that it is not a conventional classical blue phase.

In summary, on studying mixtures of the rod-shaped chiral dopant CB15 with the bent, flexible LC dimer CB7CB, we find that at relatively low concentrations of CB15 we can induce a phase that has some properties of blue phases but is markedly distinct. We find no evidence that the TB phase in the mixtures is distinct or homochiral, however. Optical textures of the TB phase in the mixtures exhibit uniaxial domains which are aligned at large angles from the rubbing, implicating a surface electroclinic effect. Evidence for conglomerate domains even at the highest CB15 concentrations indicate that the TB phase remains enantiomorphic. The BP* phase exhibits no clear optical Bragg scattering, indicating a distinction from the classical blue phases. It would be interesting to further investigate the BP* phase and determine its true nature.

4.7. Differential transmission of circularly polarized resonant X-ray light by LC phases with helical superstructures

The cholesteric phase exhibits selective reflection of circularly polarized light of wavelength equal to the pitch of the helix (typically 300 – 1000 nm). Because resonant soft-x-ray scattering (RSoXS) of LCs behaves in many ways as optical birefringence in PLM [172], it may be possible to observe selective reflection of circularly-polarized resonant x-ray light from nanometer-scale helical structures in various LC phases. We investigated LC materials exhibiting three different superstructural helices: the helical nanofilament (HNF), the cholesteric phase (N*), and a conventional blue phase (BP*). We find evidence of differential transmission of left- and right-handed circularly polarized resonant x-ray light in these materials to varying degrees, a promising result that merits further investigation.

In all of our samples, we created a silicon nitride sandwich cell by melting a small amount of sample onto one substrate and laying a second substrate on top of it. The sample then cools and adopts its preferred surface anchoring. When creating a cell with CB7CB in this way, we find it adopts random planar anchoring, causing the TB helices to be randomly oriented in the plane of the cell. We therefore generally anticipate random planar anchoring in the following materials, and we find scattering features which corroborate this. We irradiated the samples with circularly-polarized x-rays of either handedness at the carbon K-edge. We arbitrarily denote each polarization as '+' and '–' and search for differential scattering since can cannot independently determine whether we have left- or right-handed circularly-polarized light at present. Determining the absolute handedness of each will require a dedicated experiment in the future.

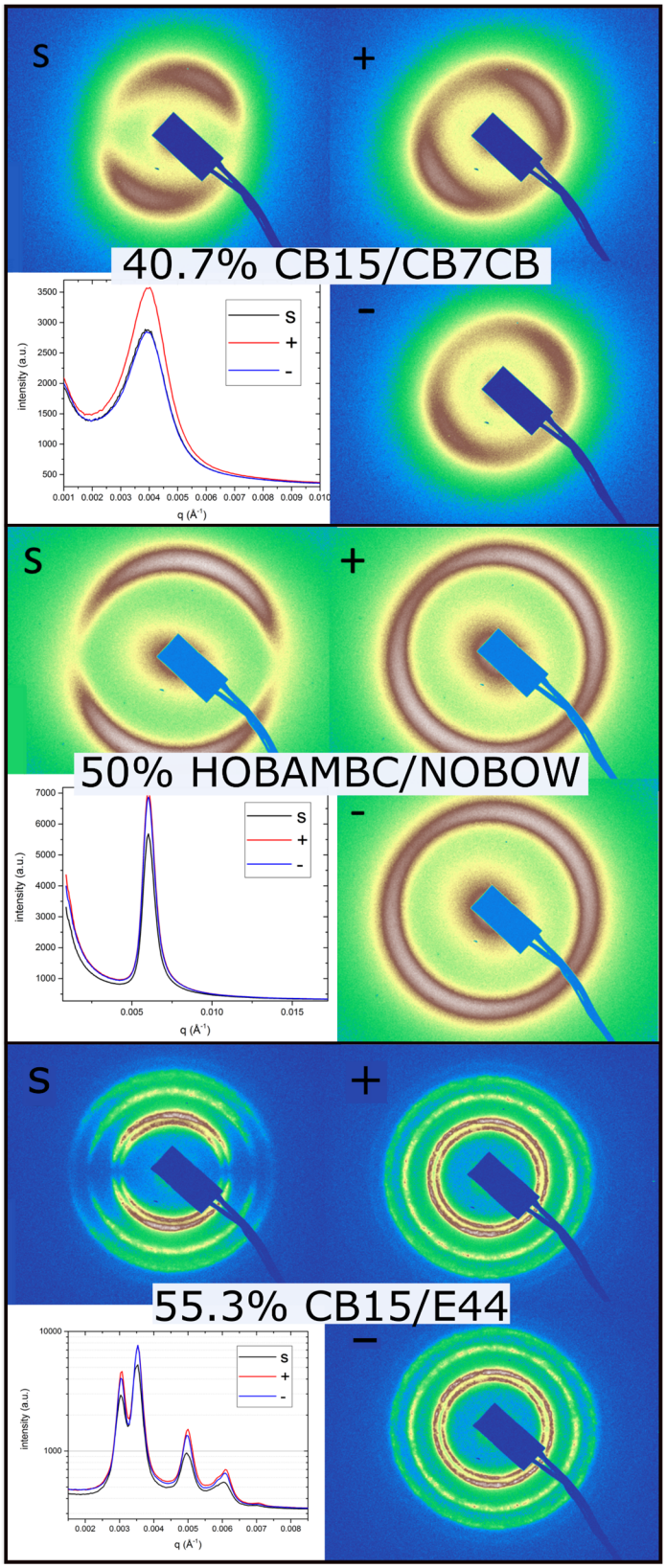

Figure 4.7.1: Circularly-polarized RSoXS of three different LC materials with helical superstructures.

A mixture of CB15 in CB7CB (40.7% CB15 by weight) exhibited a cholesteric phase when heated slightly above room temperature (Figure 4.7.1). On the incidence of a linearly s-polarized (horizontal) x-ray beam, the randomly planar-aligned cholesteric phase produces two circular scattering arcs peaked at a q value corresponding to the helix half-pitch ($p/2$ = 160 → 110 nm on heating). In the random-planar aligned cholesteric phase, maximal scattering occurs when the x-ray polarization is normal to the helix direction and minimal for polarization along the helix (perpendicular to the molecular long axis) (Figure 4.7.1), leading to the particular scattering pattern. When we apply circularly-polarized light of '+' handedness, the scattering increases significantly compared with the s-polarized incident beam, and the scattering feature is nearly circular (since the circularly-polarized light scatters

equally from different orientations of domains). The '–' handedness of light, however, affects no increase in intensity with respect to the s-polarized incident light. This demonstrates a clear differential behavior of left- and right-handed circularly-polarized light in this sample.

The 50% mixture of HOBAMBC in NOBOW forms the helical nanofilament (HNF) phase at room temperature and is known to exhibit an effectively 100% enantiomeric excess of left-handed HNFs [202]. On irradiating the sample with s-polarized light, we observe the two circular scattering arcs, as in the cholesteric material (Figure 4.7.1), indicating random planar anchoring of the HNFs in the cell. On applying the '+' handedness of circularly-polarized light, the intensity increases significantly. Applying the '–' handedness, the signal is nearly identical to that of the '+' handedness, indicating no appreciable differential treatment of left- and right-handed circularly-polarized light in this case.

The 55.3% mixture of CB15 and E44 exhibits a conventional blue phase near room temperature. This blue phase is a 3D cubic fluid composed of double-twist cylinders (see section 1.1.3) which form 3D crystallites that are randomly oriented in this sample. We therefore expect to observe a variety of scattering features corresponding to the various crystal planes which satisfy the Bragg condition, as we see. On application of s-polarized incident light, the sample exhibits a collection of scattering arcs, with minima along the polarization direction (horizontal) and maxima perpendicular to this (vertical) (Figure 4.7.1), for the same reasons as for the cholesteric phase. On applying the '+' and '–' handedness of circularly-polarized light, the scattering arcs become circular, with the intensity of the peaks in both cases increasing by about the same amount. Interestingly, each scattering peak appears to respond independently to changing the sign of the handedness of the incident beam. Only more experiments will elucidate this strange behavior.

In summary, we demonstrate a distinctive differential transmission of left- and right-handed circularly-polarized light in a cholesteric phase, with less clear results for the HNF and blue phase samples. Definitive demonstration of differential transmission of left- and right-handed circularly polarized x-ray light would permit the probing of the structural handedness of samples at the nanoscale, either to demonstrate homochirality in a TB or other LC phase of a single handedness or to possibly induce homochirality in a susceptible sample. It would be useful for investigating helical and chiral structures as we do with optical light, but for nanoscale structures such as those found in the TB phase.

4.8. RSoXS OF CB7CB AT THE NITROGEN K-EDGE

To this point, LC researchers have only used the resonant soft x-ray scattering (RSoXS) technique at the carbon K-edge to probe LC order and structure [70,121,129,130]. However, RSoXS may be used to investigate the inner core electron resonances of other atoms, including nitrogen, oxygen, or fluorine. This would potentially permit the resolution of various different kinds of orientational ordering in a single phase. For example, the carbon K-edge tends to exhibit a single large peak which is an average of excitations into the many carbon-bonded subgroups of CB7CB. However, the nitrogen atoms in CB7CB are located at the ends of the arms and encodes the orientation of the individual rigid arms of the molecule. Although we expect no different ordering when probing the carbon K-edge or the nitrogen K-edge in the TB phase of CB7CB, there may be phases with complex ordering which can benefit from such distinction. Here, I demonstrate RSoXS at the nitrogen K-edge in the TB phase of CB7CB.

At room temperature, I checked for the RSoXS signal from CB7CB at the carbon K-edge. When I found a region with significant scattering, I scanned about the nitrogen K-edge (~400 eV) and observed scattering (Figure 4.8.1a). When plotting the scattering peak area against the beam energy(Figure 4.8.1b), we observe two prominent peaks near the nitrogen K-edge along with additional fine structure which is very similar to that found in a near-edge x-ray absorption fine structure experiment on 8CB using the nitrogen K-edge [203]. Utilizing the K-edge resonances of other atoms may reveal additional structure in the orientational ordering of various LC phases that may change the paradigm of their understanding.

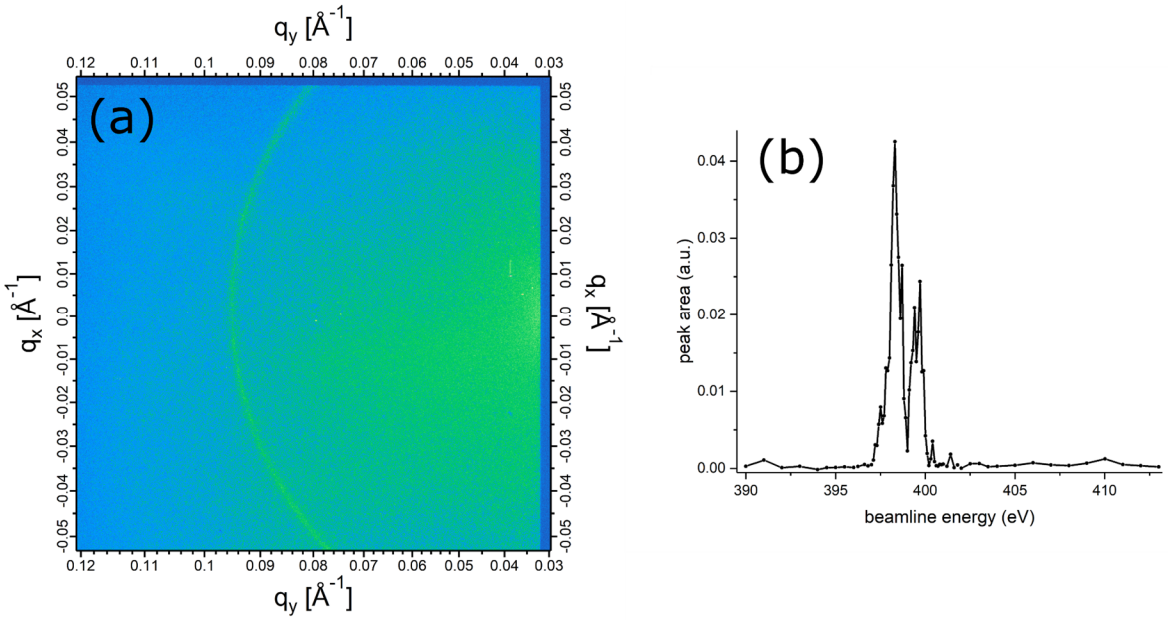

Figure 4.8.1: RSoXS of the TB phase of CB7CB at the nitrogen K-edge.
(a) An RSoXS detector image of CB7CB at the nitrogen K-edge. When the beamline energy is scanned about the K-edge resonance (~400 eV), we observe resonant scattering from the TB phase of CB7CB. (b) A plot of the area under the scattering peak in scattering as a function of beamline energy.

4.9. FFTEM AND THE TB PHASE

4.9.1. Initial experiments on the TB phase

Driven of the success of the freeze-fracture transmission electron microscopy (FFTEM) method in illuminating the nanoscale structure of many LC phases [52,53], our group carried out FFTEM experiments on the TB phase. In 2013, the Boulder [59] and Kent State University [85] groups demonstrated independently that it is possible to observe the nanoscale modulation of the TB phase using FFTEM. While our determination of the TB pitch was obtained from focal conic defects, the Kent group pointed out that in rare cases they observed anomalously small TB pitches in their sample. They could not explain this but suggested they may be regions with molecules of different conformation existing in the sample contributing to this [85]. Despite this, the Kent group determined the length scale of the TB pitch to be ~8 – 9 nm. The unresolved experimental issues with FFTEM kept it from quantitative usage beyond this.

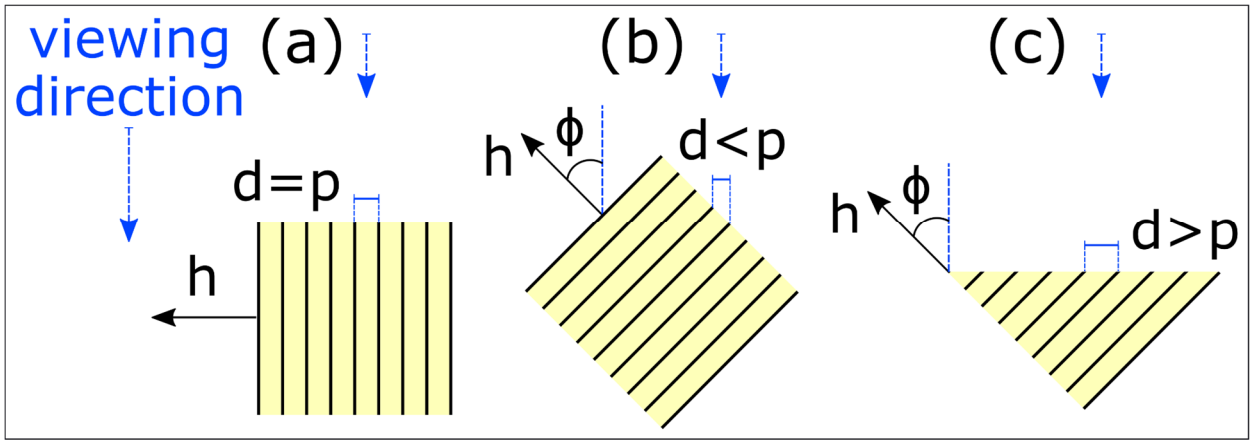

Figure 4.9.1: Geometrical effects in an FFTEM experiment of a sample with a 1D modulation. The blue arrow is the viewing direction which represents the direction of the incident beam in the TEM. (a) When the helix axis h is normal to the viewing direction, the measured periodicity d is the true periodicity p of the material. (b) When h is not normal to the viewing direction and the fracture plane contains h, then $d < p$. (c) When h is not normal to the viewing direction and the fracture plane does not contain h but is normal to the viewing direction, then $d > p$.

After our initial study was published [59], we realized that there was a distribution of TB pitches in a single FFTEM sample. We subsequently recognized that geometrical effects may tend to yield measured FFTEM periodicities which are shorter or longer than expected (Figure 4.9.1). These effects surely contributed to the observations of anomalously small periodicities by the Kent group [85]. With these considerations in mind, we implemented a statistical approach to measuring the FFTEM images of the TB pitch, helping us to quantify FFTEM measurements and to take these geometrical effects into account.

4.9.2. Quantitative characterization of FFTEM images via the FFTEM statistical method

I implemented a statistical method for quantitatively investigating FFTEM images in the TB phase which considers many FFTEM images and weights their measured periodicities to determine the probability or frequency of observing a given pitch on the entire replica. In this way, we could characterize the pitch in a sample and fix the procedure we used so that it could be reproducible for others.

The methodology is as follows: we measure the pitch within a given TB domain by taking a spatial Fourier transform of a region of uniform periodicity (Figure 4.9.2) and record its area to use as a weighting factor. This process is carried out for each TB domain in each of many images (~30 – 50) and the data are plotted in a weighted histogram. The majority of the fracture area will exhibit a pitch value which corresponds very nearly to p_{TB}, with a distribution around this value which is due to the geometrical effects described in the previous section. This is because our thin film samples (~10 μm) tend to fracture in the plane of the film in our FFTEM experiments (the fracture surface is mostly flat). But geometrical effects do contribute some anomalous values to the observed distribution. See Figure 4.9.2 for an example of how we implement this method.

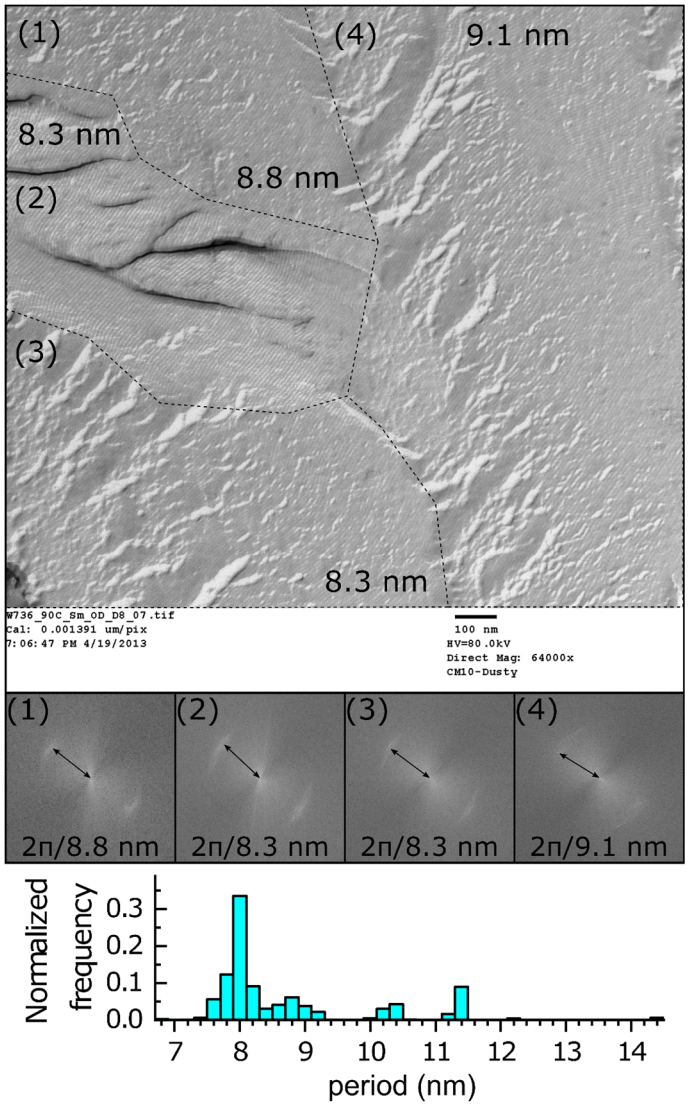

Figure 4.9.2: Example of the FFTEM statistical method.
Above is a raw FFTEM image of CB7CB quenched at 90°C in the TB phase. The image contains four distinct domains with a different periodicities and orientations of the TB helix axis. First, we partition the image into individual domains over which the pitch does not change significantly. We then perform a spatial Fast Fourier Transform (FFT) in each region. The FFT of each region exhibits peaks or arcs corresponding to the local periodicity and helix orientation. We then use a peak-finding function to reproducibly measure the FFT image and determine the pitch value. We then measure the real-space area of the domain over which we determined the pitch. We now have a set of data which includes 4 pairs of measurements: a periodicity and a corresponding area. We perform these steps for many images. We may then carry out a conventional weighted average where the periodicity is weighted by its corresponding domain area. We can plot these results as a histogram distribution. This FFTEM experiment on CB7CB quenched at 90°C yields the highest frequency of measurements around 8 nm. Knowing that CB7CB prefers to align in a random-planar configuration in an untreated clean glass cell, and that the fracture is nearly horizontal in such a thin cell, we expect to observe a peak at the true pitch value, p_{TB}. The distribution of observations in the near vicinity of the peak are likely due to the geometrical effects noted in Figure 4.9.1. The small spurious peaks with longer period can be explained by a real softening of the pitch structure, which was definitively measured using RSoXS (section 3.2.5). At low temperature in the TB phase, these peaks disappear (Figure 4.9.3).

4.9.3. FFTEM of the LC phases of CB7CB

Using this statistical methodology, we measured the temperature dependence of the pitch of CB7CB with FFTEM (Figure 4.9.3). When we quench CB7CB at 99°C, just below the N – TB transition, we measure a broad pitch distribution which exhibits prominent peaks at ~8 nm and ~9 nm, but with a tail that extends out to ~13 nm. On further cooling, this tail becomes smaller, until only a single peak centered around 8 nm remains at room temperature.

The presence of the significant tail at elevated temperatures in the TB phase was a mystery until we performed resonant soft x-ray scattering (RSoXS) on CB7CB. We now know that this distribution of periodicities at high temperatures represents the real behavior of CB7CB [70]: a

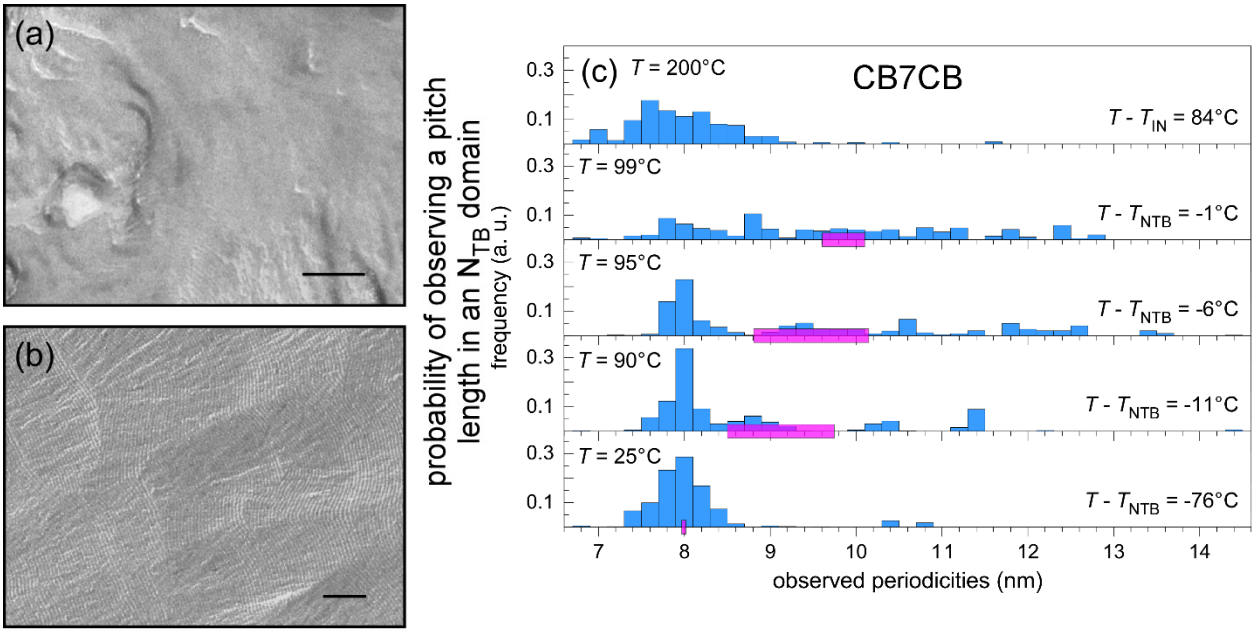

Figure 4.9.3: FFTEM images of CB7CB quenched from the isotropic phase and histogram distributions of TB pitch at five temperatures.
On quenching CB7CB from 200°C using copper planchettes, (87°C above the clearing point), we find some domains which are amorphous (a) and some which contain well-oriented TB modulations of ~8 nm spacing (b). (c) Distribution of periodicities in neat CB7CB as a function of quenching temperature, with the measured pitch range obtained by RSoXS at the given temperature overlaid as a pink bar.

spatial and temporal variation of the pitch at high temperature due to increased fluctuations in the TB helix and domain pinning.

In 2013, the Boulder group reported FFTEM results from CB7CB in the nematic phase, as well as in the TB phase [59]. These FFTEM images showed a lack of periodic modulations in the N phase, demonstrating that the quenching process was quick enough to be able to distinguish the two phases in FFTEM. However, subsequent experiments in the N phase of CB7CB revealed many periodic modulations throughout the cell. To check our procedure, we even elevated the temperature to the isotropic phase, believing this would surely be a high enough temperature that we would not encounter periodic modulations, as the CB7CB would have to pass through two different phase transitions during the quench. Indeed, we could still observe the periodic modulations associated with the TB phase, albeit only filling ~50% of the fracture surface (Figure 4.9.3a,b). Even switching from glass planchettes to copper planchettes to improve heat transfer across the cell still yielded a fracture surface filled with TB modulations. I performed the following investigation to determine the efficacy of our procedure in studying the TB phase and other fluid phases.

We began by performing experiments on CB7CB in glass planchettes in which we targeted each of its LC phases and quenched them in liquid propane as we do in our FFTEM experiments (Figure 2.2.2). We then placed the quenched sample into a chilled microscope to determine what happened during the quench (Figure 4.9.4). We found that before and after quenching the TB phase at room temperature, we observed very little difference in the PLM textures (Figure 4.9.4a,b). However, quenching from higher temperature in the TB phase and from the nematic and isotropic phases of CB7CB, we found significant differences in the textures (Figure 4.9.4c-h), indicating

significant change in the nanoscale morphology in the post-quenched state from the pre-quenched state.

Figure 4.9.4: PLM images of CB7CB before and after quenching in liquid propane.
We cooled glass planchette cells filled with CB7CB to the desired temperature under the microscope, took an image of the texture ("before quench" column), then quenched the cell in liquid propane. We then reduced the temperature of the microscope stage to ~130 K, placed the cell back under the microscope, and observed the textures ("after quench" column). (a) 76°C below the N – TB transition, the phase exhibits disordered stripe textures in an untreated glass cell. (b) After rapidly quenching the cell, we recover a texture and birefringence similar to that in (a), except that thermal contraction leaves cracks in the sample. (c) 0.1°C below the N – TB transition, we observe the blocky textures of the TB phase. (d) After quenching, we do not recover the original texture, but one similar to that observed in (b). (e) 0.1°C below the I – N transition, the nematic is mostly homeotropic. (f) After quenching, the cell has more birefringence. Based on FFTEM experiments in this temperature range in which we observed TB modulations, a significant fraction of this cell must be filled with the TB phase. (g) 87°C above the clearing point of CB7CB, we observe a featureless isotropic sample. (h) After quenching, we find grainy birefringent textures coexisting with some dark regions. Based on FFTEM experiments in this temperature range in which we observe large, micron-scale domains with 8 nm modulations and a comparable number of amorphous domains, these grainy domains must be made of the TB phase, while the dark regions are either isotropic or nematic.

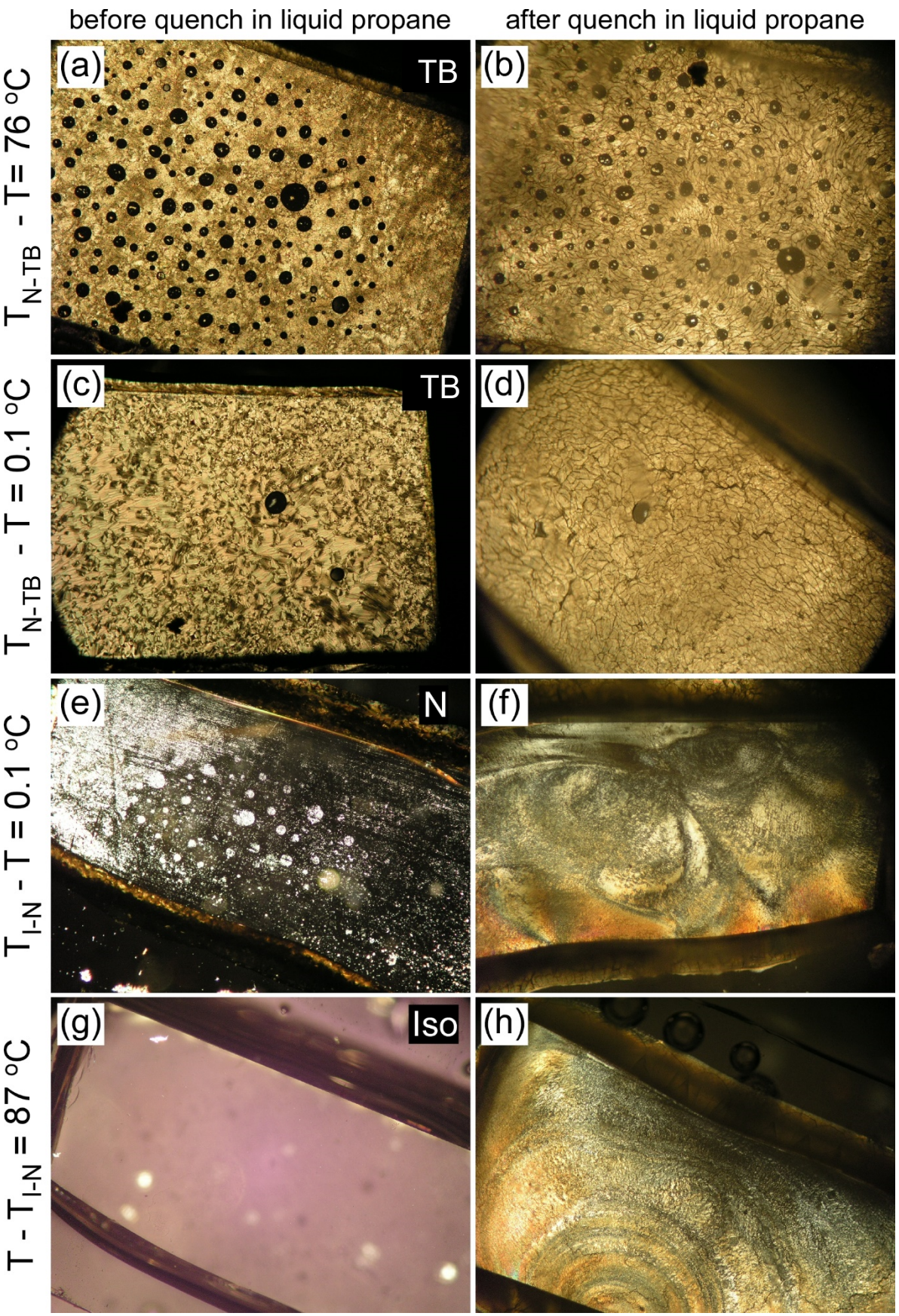
before quench in liquid propane
after quench in liquid propane
T_{N-TB} - T= 76 °C
T_{N-TB} - T = 0.1 °C
T_{I-N} - T = 0.1 °C
T - T_{I-N} = 87 °C
(a)
TB
(b)
(c)
TB
(d)
(e)
N
(f)
(g)
Iso
(h)

Next, we quenched the nematic and TB phases and maintained them at room-temperature (Figure 4.9.5). We found clear indications of crystallization after ~10 minutes at room temperature. This indicates the following: despite the fact that the quench does not reliably vitrify the isotropic or nematic phases of CB7CB, the sample does not enter a crystal phase either. This observation

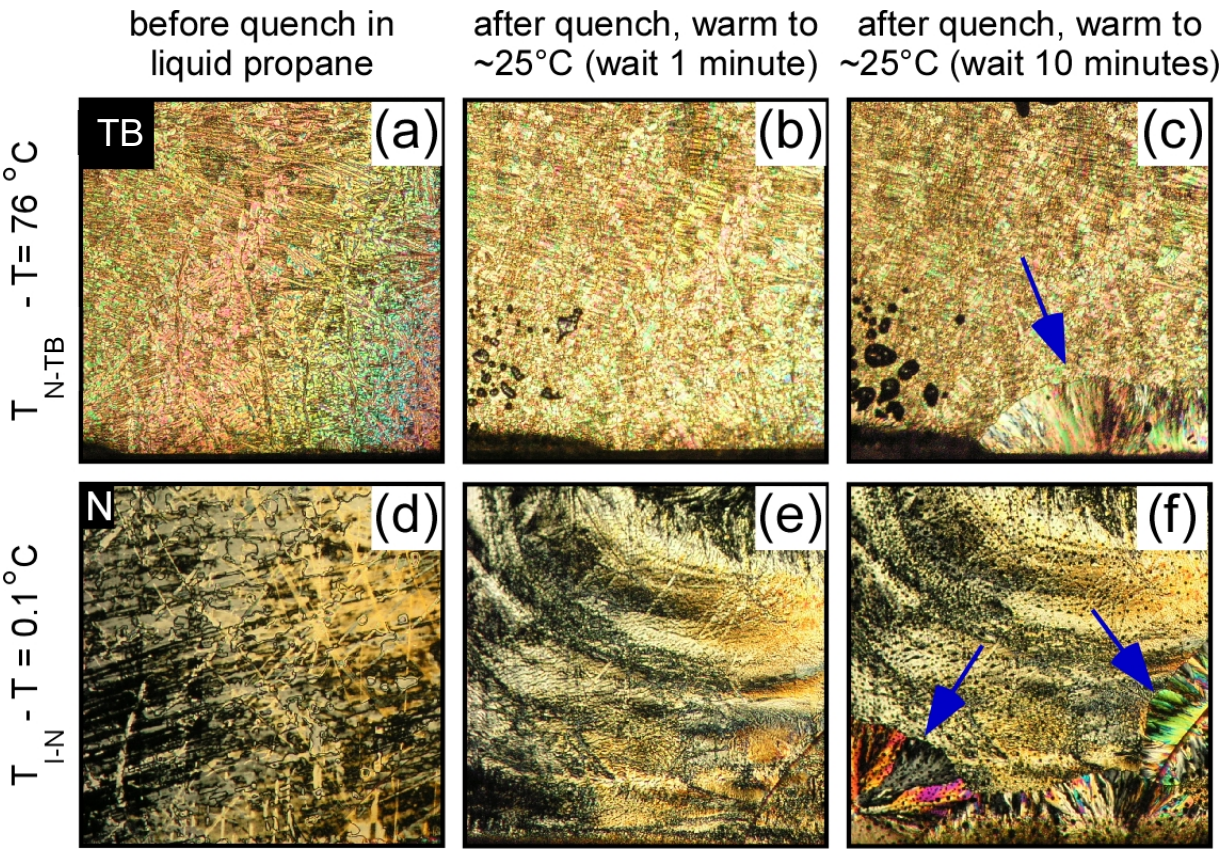

Figure 4.9.5: PLM images of CB7CB before and after quenching and after warming to room temperature.
We bring glass planchette cells filled with CB7CB to the desired temperature under the microscope, take an image of the texture ("before quench" column), then quench the cell in liquid propane (90 K). We then place the cell back into the microscope stage, which is maintained at 25°C, and observe the textures after 1 minute and 10 minutes. (a) 76°C below the N – TB transition, we find a disordered stripe texture in the untreated glass cell. (b) After quenching and subsequent warming to room temperature and waiting 1 minute, we find a similar texture to that in (a) but with air bubbles forming throughout the cell. These come from cracks which form on thermal contraction of the phase during quenching which coalesce into bubbles when the sample warms. (c) After 10 minutes, spherulitic crystal domains begin to grow. (d) 0.1°C below the I – N transition, the nematic exhibits director fluctuations and characteristic Schlieren textures. (e) After quenching and subsequent warming to room temperature and waiting 1 minute, we find that the texture looks very different from (d), and there is a prominent crack in the glass from the rapid quenching. (f) After 10 minutes at room temperature, spherulitic crystal domains begin to grow at the edges of the sample.

proves that the TB topographical modulations are in fact vitrified TB domains and not features of a crystal phase.

To understand how quickly we quench our samples in FFTEM, I treated the quenching system as a 1D transient heat flow problem as shown in Figure 4.9.6a. During quenching, the cell is immersed in a ~2 cm diameter reservoir of liquid propane, which is maintained at 90 K by a large liquid nitrogen reservoir. The thermal diffusivity of liquid propane at 90 K is $\alpha \sim 10^{-7}$ m^2 s^{-1} [204]), and that of glass and typical LCs at room temperature is $\alpha \sim 10^{-7}$ m^2 s^{-1} [205,206]. We therefore assume that the whole cell is made entirely of a slab of thermal diffusivity $\alpha = 1 \cdot 10^{-7}$ m^2 s^{-1}, and that it does not vary with temperature. We believe these to be reasonable approximations given that the thermal diffusivity of glass increases by only ~25% from 300 K to 100 K, and that the LC sample makes up a small portion of the whole cell. Using this information, I calculated the transient temperature and the average initial cooling rate at the center of the LC (Figure 4.9.6b). The average cooling rate of the cell during the first second of quenching is ~150 K·s^{-1} for T_i = 500 K, while it is ~75 K·s^{-1} for T_i = 300 K. 5CB vitrifies at cooling rates equal to or greater than ~0.02 K·s^{-1} [207], and MBBA vitrifies at cooling rates equal to or greater than ~0.67 K·s^{-1} [208]. The calculated cooling rates are quick enough to vitrify typical LCs like 5CB and MBBA but are apparently not quick enough to quench the isotropic or nematic phase of CB7CB. Since the cooling rate for copper planchettes dropped into liquid propane is ~104 K·s^{-1} [204], and to vitrify the isotropic phase to a glassy state we need to cool on the order of ~100 K, we place an upper limit on the timescale of formation of micron-scale, well-oriented TB domains in CB7CB at <10 ms. Therefore, it is best to rely on other experimental methods to study the TB phase. It is also important to take care when performing FFTEM on nematics and other phases which are expected to be very fluid.

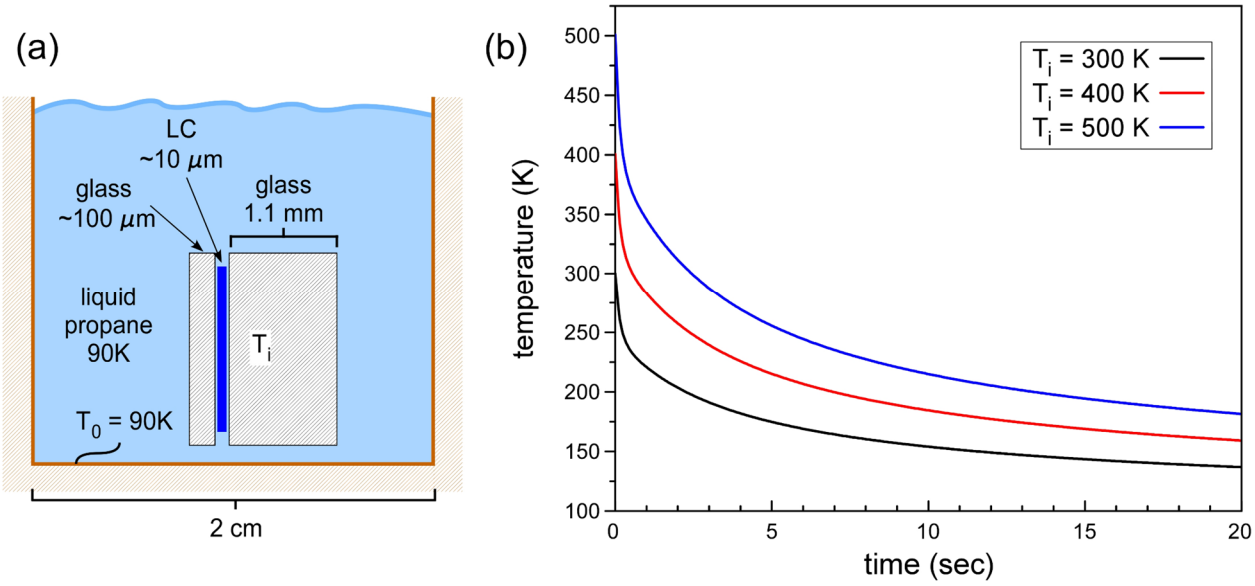

Figure 4.9.6: Modeling the transient heat flow in an FFTEM cell.
(a) Schematic of the FFTEM quenching geometry. The cell is immersed in a 2 cm wide reservoir of liquid propane maintained at 90 K. The cell is composed of two glass substrates of thickness 100 μm and 1.1 mm respectively, with the LC in between. The entire cell is maintained at the starting temperature T_i until it contacts the liquid propane. We then calculate the temperature at the position of the LC film as a function of time. (b) Temperature as a function of time for three initial temperatures of the cell.

4.9.4. FFTEM experiments on mixtures of CB7CB and 5CB

A natural experiment to carry out to understand the variation of the nanoscale structure of the TB phase is to make mixtures of CB7CB with a well-understood nematic guest, such as 5CB. Thus, we made eight mixtures of 5CB and CB7CB of different concentrations and systematically measured the helix pitch of the TB phase using FFTEM, quenching at a temperature ~10°C below the N – TB phase transition. We then recorded dozens of FFTEM images of each mixture in the TB phase. The mixtures exhibit the characteristic TB surface topography modulations.

We compared the pitch distributions of a series of mixtures of 5CB and CB7CB to investigate the concentration dependence of the observed periodicity (Figure 4.9.7a). We found that the pitch does in fact depend on the 5CB concentration. The pitch distribution shifts modestly toward larger pitch values on increasing 5CB concentration, from 8 nm in the $x = 0$ mixture to 9.2 nm in the $x = 37.5$ (where x is the weight fraction of 5CB in CB7CB). This agrees quite well with the corresponding RSoXS measurement (shown in pink bars in Figure 4.9.7). Interestingly, we found that at concentrations above $x = 50.0$, the distribution in the observed periodicities broadens dramatically and shifts to larger periodicity. This could be due to something exciting, such as a novel phase transition in this system or a discontinuous change in the TB pitch, or something more routine such as phase separation on quenching. We could not verify the behavior with RSoXS because these mixtures form the TB phase below room temperature, and the RSoXS beamtime was not capable of reaching these regimes at the time. This would be an interesting experiment to carry out in the future.

We observed nanometer-scale modulations in all the mixtures until we reach concentrations of $x \geq 75.0$. Even when this mixture is quenched at -20°C, a temperature which

should correspond to the TB phase according to a binary phase diagram of the mixtures, we do not observe clear nanometer-scale modulations in FFTEM.

Next, we used FFTEM to investigate the temperature-dependence of a 25% 5CB/CB7CB mixture to discern any influence that the 5CB may have on the TB pitch as a function of temperature (Figure 4.9.7b). Just below the N – TB phase transition, we measured a very broad distribution in periodicity, with values ranging from ~7 – 14 nm, likely due to enhanced fluctuations in the TB helix at high temperature. Several degrees below the N – TB transition, the periodicity tightens around p = ~8.5 nm. This behavior persists until 29°C, at which point the pitch

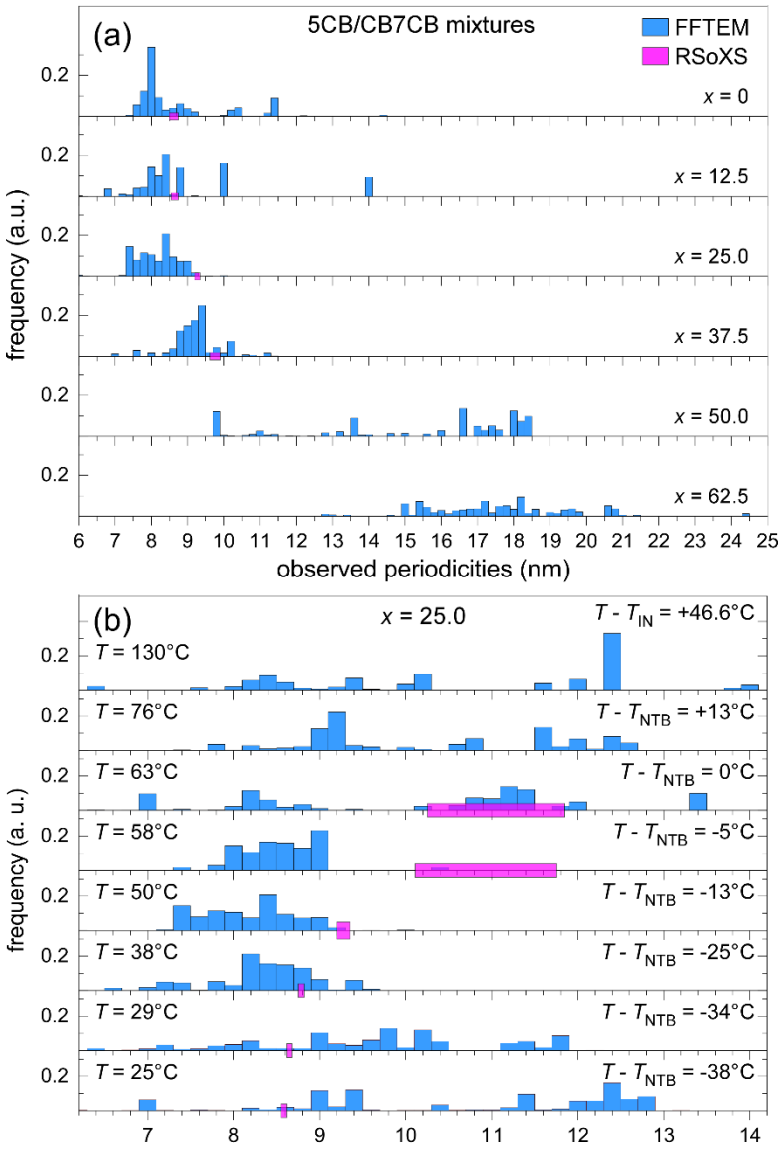

Figure 4.9.7: Weighted frequency of measured periodicities in 5CB/CB7CB mixtures.
(a) weighted distributions of the periodicities of several 5CB/CB7CB mixtures indicate that the heliconical pitch increases steadily up to x = 37.5. RSoXS data overlaid onto the FFTEM distributions show roughly the same conclusion but are shifted slightly to longer pitch lengths. For x = 50.0 and 62.5, the measured periodicity of these samples becomes very broad and the mean periodicity increases dramatically beyond those found in the mixtures with lesser 5CB concentration. (b) Distribution of periodicities in the x = 25.0 mixture as a function of quenching temperature. RSoXS data under the same experimental conditions is overlaid as pink bars.

distribution broadens once again. We attribute this behavior to the 5CB in the mixture, since this kind of peak spreading of the distribution at low temperature does not occur in the neat CB7CB (Figure 4.9.3). This may be due to phase separation during the quench or crystallization in the sample.

4.9.5. FFTEM experiments on 50% mixtures of CB7CB and the nCBs

On varying the tail length of the nematic dopant in 50% *n*CB/CB7CB mixtures from $n = 5$ to 8, we find only a very subtle apparent decrease in the periodicity of the distributions, as shown in Figure 4.9.8.

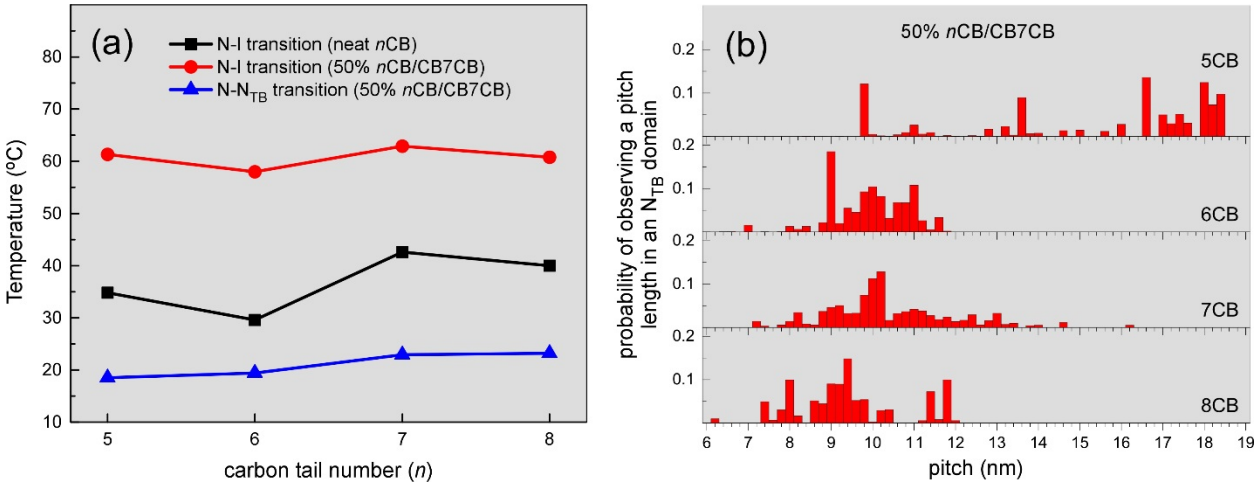

Figure 4.9.8: Phase diagram and TB helix pitch distributions of 50% mixtures of *n*CB/CB7CB (*n* = 5 to 8) as measured by FFTEM.
(a) Binary phase diagram of 50% *n*CB/CB7CB mixtures and neat *n*CB indicate that the odd-even effect in the I – N transition temperature of the *n*CB series is also present in the I – N transitions of the mixtures, but not in the N – TB transition. (b) Measured helix pitch distribution as a function of carbon tail number *n* in 50% *n*CB/CB7CB mixtures. The pitch distributions of the mixtures are quite broad and show only a very weak decrease in the TB pitch with increasing *n*.

4.9.6. The role of FFTEM in studying the TB phase

With demonstrations of the usefulness of RSoXS, FFTEM has become a much less desirable method of determining the TB pitch of an LC material. However, most research groups do not have routine access to RSoXS, and FFTEM may be more readily available. FFTEM does provide a relatively accurate measure of the low temperature, ground state TB pitch of a material. This can provide a sense of the scale which can guide RSoXS experiments when they become available.

5. REFERENCES

[1] W. Brostow, Polymer **31**, 979 (1990).

[2] C. on L. C. Polymers, *Liquid Crystalline Polymers.* (National Academies Press, Washington, 1990).

[3] M. Nakata, G. Zanchetta, B. D. Chapman, C. D. Jones, J. O. Cross, R. Pindak, T. Bellini, and N. A. Clark, Science **318**, 1276 (2007).

[4] T. Bellini, G. Zanchetta, T. P. Fraccia, R. Cerbino, E. Tsai, G. P. Smith, M. J. Moran, D. M. Walba, and N. A. Clark, PNAS **109**, 1110 (2012).

[5] T. Fraccia, G. Smith, N. Clark, and T. Bellini, Crystals **8**, 5 (2017).

[6] H. K. Bisoyi and S. Kumar, Chem. Soc. Rev. **40**, 306 (2010).

[7] Y. Garbovskiy and A. Glushchenko, Nanomaterials **7**, 361 (2017).

[8] M. Shuai, A. Klittnick, Y. Shen, G. P. Smith, M. R. Tuchband, C. Zhu, R. G. Petschek, A. Mertelj, D. Lisjak, M. Čopič, J. E. Maclennan, M. A. Glaser, and N. A. Clark, Nat. Commun. **7**, 10394 (2016).

[9] I. Muševič, *Liquid Crystal Colloids* (Springer International Publishing, Cham, 2017).

[10] I. I. Smalyukh, Annu. Rev. Condens. Matter Phys. **9**, (2018).

[11] P. van der Asdonk, H. C. Hendrikse, M. Fernandez-Castano Romera, D. Voerman, B. E. I. Ramakers, D. W. P. M. Löwik, R. P. Sijbesma, and P. H. J. Kouwer, Adv. Funct. Mater. **26**, 2609 (2016).

[12] M.-H. Li and P. Keller, Philos. Trans. Royal Soc. A **364**, 2763 (2006).

[13] J. P. F. Lagerwall and G. Scalia, Current Applied Physics **12**, 1387 (2012).

[14] P. Oswald and P. Pieranski, *Nematic and Cholesteric Liquid Crystals* (Taylor & Francis Group, 2005).

[15] I. Dierking, *Textures of Liquid Crystals* (John Wiley & Sons, 2006).

[16] L. M. Blinov, *Structure and Properties of Liquid Crystals* (Springer Netherlands, Dordrecht, 2011).

[17] P. G. de Gennes and J. Prost, *The Physics of Liquid Crystals* (Clarendon Press, 1995).

[18] L. Onsager, Ann. N. Y. Acad. Sci. **51**, 627 (1949).

[19] S. Al-Zangana, M. Iliut, M. Turner, A. Vijayaraghavan, and I. Dierking, Adv. Opt. Mater **4**, 1541 (2016).

[20] A. Mertelj, D. Lisjak, M. Drofenik, and M. Čopič, Nature **504**, 237 (2013).

[21] M. López-Valdeolivas, D. Liu, D. J. Broer, and C. Sánchez-Somolinos, Macromolecular Rapid Communications **39**, 1700710 (2018).

[22] A. H. Gelebart, D. J. Mulder, G. Vantomme, A. P. H. J. Schenning, and D. J. Broer, Angewandte Chemie International Edition **56**, 13436 (2017).

[23] A. H. Gelebart, G. Vantomme, E. W. Meijer, and D. J. Broer, Advanced Materials **29**, 1606712 (2017).

[24] P. S. Noonan, P. Mohan, A. P. Goodwin, and D. K. Schwartz, Adv. Funct. Mater. **24**, 3206 (2014).

[25] Platypus Technologies (n.d.).

[26] H.-S. Kitzerow and C. Bahr, editors , *Chirality in Liquid Crystals* (Springer, New York, 2001).

[27] *Chiral Technology Market - Global Industry Forecast, Share, Size, Growth And Industry Analysis (2011-2017)* (n.d.).

[28] J. W. Goodby, J. Mater. Chem. **1**, 307 (1991).

[29] F. Reinitzer, Monatshefte Für Chemie (Wein) **9**, 421 (1888).
[30] T. J. Sluckin, D. A. Dunmur, and H. Stegemeyer, editors , *Crystals That Flow: Classic Papers from the History of Liquid Crystals*, 1 edition (CRC Press, London ; New York, 2004).
[31] V. A. Belyakov and V. E. Dmitrienko, Physics-Uspekhi **28**, 535 (1985).
[32] T. Seideman, Rep. Prog. Phys. **53**, 659 (1990).
[33] P. P. Crooker, in *Chirality in Liquid Crystals* (Springer, 2001), pp. 186–222.
[34] H. Kikuchi, in *Liquid Crystalline Functional Assemblies and Their Supramolecular Structures*, edited by T. Kato (Springer Berlin Heidelberg, Berlin, Heidelberg, 2008), pp. 99–117.
[35] B. Pansu, M. H. Li, and H. T. Nguyen, J. Phys. II France **7**, 13 (1997).
[36] E. Grelet, B. Pansu, M.-H. Li, and H. T. Nguyen, Phys. Rev. Lett. **86**, 3791 (2001).
[37] D. Coates and G. W. Gray, Phys. Lett. A **45**, 115 (1973).
[38] H. Stegemeyer, T. Blümel, K. Hiltrop, H. Onusseit, and F. Porsch, Liquid Crystals **1**, 3 (1986).
[39] D. L. Johnson, J. H. Flack, and P. P. Crooker, Phys. Rev. Lett. **45**, 641 (1980).
[40] S. Meiboom and M. Sammon, Phys. Rev. Lett. **44**, 882 (1980).
[41] S. Meiboom and M. Sammon, Phys. Rev. A **24**, 468 (1981).
[42] V. Belyakov, E. Demikhov, V. Dmitrienko, and V. Dolganov, Zh. Eksp. Teor. Fiz **89**, 2035 (1985).
[43] M. J. Costello, S. Meiboom, and M. Sammon, Physical Review A **29**, 2957 (1984).
[44] H. Delacroix, J.-M. Gilli, I. Erk, and P. Mariani, Phys. Rev. Lett. **69**, 2935 (1992).
[45] G. R. Luckhurst, Thin Solid Films **393**, 40 (2001).
[46] C. Tschierske and D. J. Photinos, J. Mater. Chem. **20**, 4263 (2010).
[47] L. J. Yu and A. Saupe, Phys. Rev. Lett. **45**, 1000 (1980).
[48] M. Cestari, S. Diez-Berart, D. A. Dunmur, A. Ferrarini, M. R. de la Fuente, D. J. B. Jackson, D. O. Lopez, G. R. Luckhurst, M. A. Perez-Jubindo, R. M. Richardson, J. Salud, B. A. Timimi, and H. Zimmermann, Phys. Rev. E **84**, 031704 (2011).
[49] H. Takezoe and Y. Takanishi, Jpn. J. Appl. Phys. **45**, 597 (2006).
[50] R. A. Reddy and C. Tschierske, J. Mater. Chem. **16**, 907 (2006).
[51] D. R. Link, G. Natale, R. Shao, J. E. Maclennan, N. A. Clark, E. Körblova, and D. M. Walba, Science **278**, 1924 (1997).
[52] L. E. Hough, M. Spannuth, M. Nakata, D. A. Coleman, C. D. Jones, G. Dantlgraber, C. Tschierske, J. Watanabe, E. Körblova, D. M. Walba, J. E. Maclennan, M. A. Glaser, and N. A. Clark, Science **325**, 452 (2009).
[53] L. E. Hough, H. T. Jung, D. Krüerke, M. S. Heberling, M. Nakata, C. D. Jones, D. Chen, D. R. Link, J. Zasadzinski, G. Heppke, J. P. Rabe, W. Stocker, E. Körblova, D. M. Walba, M. A. Glaser, and N. A. Clark, Science **325**, 456 (2009).
[54] D. A. Coleman, J. Fernsler, N. Chattham, M. Nakata, Y. Takanishi, E. Körblova, D. R. Link, R.-F. Shao, W. G. Jang, J. E. Maclennan, O. Mondainn-Monval, C. Boyer, W. Weissflog, G. Pelzl, L.-C. Chien, J. Zasadzinski, J. Watanabe, D. M. Walba, H. Takezoe, and N. A. Clark, Science **301**, 1204 (2003).
[55] M. Abramowitz, *Basics and Beyond* (Melville, 2003).
[56] M. W. Davidson and M. Abramowitz, Encyclopedia of Imaging Science and Technology (2002).
[57] G. H. Brown and W. G. Shaw, Chem. Rev. **57**, 1049 (1957).

[58] S. Kumar, *Liquid Crystals: Experimental Study of Physical Properties and Phase Transitions* (Cambridge University Press, 2001).
[59] D. Chen, J. H. Porada, J. B. Hooper, A. Klittnick, Y. Shen, M. R. Tuchband, E. Korblova, D. Bedrov, D. M. Walba, M. A. Glaser, J. E. Maclennan, and N. A. Clark, PNAS **110**, 15931 (2013).
[60] S. R. Renn and T. C. Lubensky, Phys. Rev. A **38**, 2132 (1988).
[61] H.-S. Kitzerow, in *Chirality in Liquid Crystals* (Springer, 2001), pp. 296–354.
[62] H. F. Gleeson and L. S. Hirst, Chem. Eur. J. of Chem. Phys. **7**, 321 (2006).
[63] J. Stöhr, *NEXAFS Spectroscopy* (Springer, Berlin; New York, 1996).
[64] F. Liu, C. Wang, J. K. Baral, L. Zhang, J. J. Watkins, A. L. Briseno, and T. P. Russell, J. Am. Chem. Soc. **135**, 19248 (2013).
[65] J. M. Virgili, Y. Tao, J. B. Kortright, N. P. Balsara, and R. A. Segalman, Macromolecules **40**, 2092 (2007).
[66] C. Wang, D. H. Lee, A. Hexemer, M. I. Kim, W. Zhao, H. Hasegawa, H. Ade, and T. P. Russell, Nano Lett. **11**, 3906 (2011).
[67] J. R. Tumbleston, B. A. Collins, L. Yang, A. C. Stuart, E. Gann, W. Ma, W. You, and H. Ade, Nat. Photonics **8**, 385 (2014).
[68] B. A. Collins, J. E. Cochran, H. Yan, E. Gann, C. Hub, R. Fink, C. Wang, T. Schuettfort, C. R. McNeill, M. L. Chabinyc, and H. Ade, Nat. Mater. **11**, 536 (2012).
[69] C. Zhu, C. Wang, A. Young, F. Liu, I. Gunkel, D. Chen, D. Walba, J. Maclennan, N. Clark, and A. Hexemer, Nano Lett. **15**, 3420 (2015).
[70] C. Zhu, M. R. Tuchband, A. Young, M. Shuai, A. Scarbrough, D. M. Walba, J. E. Maclennan, C. Wang, A. Hexemer, and N. A. Clark, Phys. Rev. Lett. **116**, (2016).
[71] F. Liu, M. A. Brady, and C. Wang, Eur. Polym. J. **81**, (2016).
[72] J. Ilavsky, J. Appl. Crystallogr. **45**, 324 (2012).
[73] F. Zhang, J. Ilavsky, G. G. Long, J. P. G. Quintana, A. J. Allen, and P. R. Jemian, Metall. Mater. Trans A **41**, 1151 (2010).
[74] R. B. Meyer, in *Molecular Fluids*, edited by R. Balian and G. Weil (Gordon and Breach, New York, 1976), pp. 273–373.
[75] I. Dozov, Eur. Phys. Lett. **56**, 247 (2001).
[76] R. Memmer, Liquid Crystals **29**, 483 (2002).
[77] P. J. Barnes, A. G. Douglass, S. K. Heeks, and G. R. Luckhurst, Liquid Crystals **13**, 603 (1993).
[78] V. P. Panov, M. Nagaraj, J. K. Vij, Y. P. Panarin, A. Kohlmeier, M. G. Tamba, R. A. Lewis, and G. H. Mehl, Phys. Rev. Lett. **105**, 167801 (2010).
[79] A. Hoffmann, A. G. Vanakaras, A. Kohlmeier, G. H. Mehl, and D. J. Photinos, Soft Matter **11**, 850 (2015).
[80] E. Gorecka, M. Salamonczyk, A. Zep, D. Pociecha, C. Welch, Z. Ahmed, and G. H. Mehl, Liquid Crystals **42**, 1 (2015).
[81] G. H. Mehl, P. Karahaliou, C. Welch, Z. Ahmed, and E. Ramou, Soft Matter (2015).
[82] A. G. Vanakaras and D. J. Photinos, Soft Matter (2016).
[83] A. Kumar, A. G. Vanakaras, and D. J. Photinos, ArXiv Preprint ArXiv:1708.06392 (2017).
[84] K. Adlem, M. Čopič, G. R. Luckhurst, A. Mertelj, O. Parri, R. M. Richardson, B. D. Snow, B. A. Timimi, R. P. Tuffin, and D. Wilkes, Phys. Rev. E **88**, (2013).
[85] V. Borshch, Y.-K. Kim, J. Xiang, M. Gao, A. Jákli, V. P. Panov, J. K. Vij, C. T. Imrie, M. G. Tamba, G. H. Mehl, and O. D. Lavrentovich, Nat. Commun. **4**, 2635 (2013).

[86] R. B. Meyer, *Structural Problems in Liquid Crystal Physics. , 1973* (Les Houches Summer School in Theoretical Physics, 1976).
[87] P. K. Challa, V. Borshch, O. Parri, C. T. Imrie, S. N. Sprunt, J. T. Gleeson, O. D. Lavrentovich, and A. Jákli, Phys. Rev. E **89**, (2014).
[88] J. P. Hurault, J. Chem. Phys. **59**, 2068 (1973).
[89] N. A. Clark and R. B. Meyer, Appl. Phys. Lett. **22**, 493 (1973).
[90] A. Zep, S. Aya, K. Aihara, K. Ema, D. Pociecha, K. Madrak, P. Bernatowicz, H. Takezoe, and E. Gorecka, J. Mater. Chem. C **1**, 46 (2013).
[91] D. Chen, M. Nakata, R. Shao, M. R. Tuchband, M. Shuai, U. Baumeister, W. Weissflog, D. M. Walba, M. A. Glaser, J. E. Maclennan, and N. A. Clark, Phys. Rev. E **89**, 022506 (2014).
[92] M. G. Tamba, S. M. Salili, C. Zhang, A. Jákli, G. H. Mehl, R. Stannarius, and A. Eremin, RSC Adv. **5**, 11207 (2015).
[93] E. Gorecka, N. Vaupotič, A. Zep, D. Pociecha, J. Yoshioka, J. Yamamoto, and H. Takezoe, Angew. Chem. **127**, 10293 (2015).
[94] C. T. Archbold, E. J. Davis, R. J. Mandle, S. J. Cowling, and J. W. Goodby, Soft Matter **11**, 7547 (2015).
[95] Y. Wang, G. Singh, D. M. Agra-Kooijman, M. Gao, H. K. Bisoyi, C. Xue, M. R. Fisch, S. Kumar, and Q. Li, CrystEngComm **17**, 2778 (2015).
[96] V. P. Panov, J. K. Vij, and G. H. Mehl, Liquid Crystals **44**, 147 (2016).
[97] R. J. Mandle and J. W. Goodby, Soft Matter **12**, 1436 (2016).
[98] P. A. Henderson and C. T. Imrie, Liquid Crystals **38**, 1407 (2011).
[99] C. S. P. Tripathi, P. Losada-Pérez, C. Glorieux, A. Kohlmeier, M.-G. Tamba, G. H. Mehl, and J. Leys, Phys. Rev. E **84**, (2011).
[100] R. J. Mandle, E. J. Davis, C. T. Archbold, S. J. Cowling, and J. W. Goodby, J. Mater. Chem. C **2**, 556 (2013).
[101] N. Sebastián, D. O. López, B. Robles-Hernández, M. R. de la Fuente, J. Salud, M. A. Pérez-Jubindo, D. A. Dunmur, G. R. Luckhurst, and D. J. B. Jackson, Phys. Chem. Chem. Phys. **16**, 21391 (2014).
[102] Z. Ahmed, C. Welch, and G. H. Mehl, RSC Adv. **5**, 93513 (2015).
[103] S. M. Jansze, A. Martínez-Felipe, J. M. D. Storey, A. T. M. Marcelis, and C. T. Imrie, Angew. Chem. Int. Ed. **54**, 643 (2015).
[104] R. Mandle and J. Goodby, Soft Matter **12**, 1436 (2016).
[105] R. J. Mandle, C. C. A. Voll, D. J. Lewis, and J. W. Goodby, Liquid Crystals **43**, 13 (2015).
[106] A. A. Dawood, M. C. Grossel, G. R. Luckhurst, R. M. Richardson, B. A. Timimi, N. J. Wells, and Y. Z. Yousif, Liquid Crystals **43**, 2 (2016).
[107] R. J. Mandle, C. T. Archbold, J. P. Sarju, J. L. Andrews, and J. W. Goodby, Scientific Reports **6**, 36682 (2016).
[108] R. J. Mandle, Soft Matter **12**, 7883 (2016).
[109] D. A. Paterson, M. Gao, Y.-K. Kim, A. Jamali, K. L. Finley, B. Robles-Hernández, S. Diez-Berart, J. Salud, M. R. de la Fuente, B. A. Timimi, H. Zimmermann, C. Greco, A. Ferrarini, J. M. D. Storey, D. O. López, O. D. Lavrentovich, G. R. Luckhurst, and C. T. Imrie, Soft Matter **12**, 6827 (2016).
[110] D. A. Paterson, J. Xiang, G. Singh, R. Walker, D. M. Agra-Kooijman, A. Martínez-Felipe, M. Gao, J. M. D. Storey, S. Kumar, O. D. Lavrentovich, and C. T. Imrie, J. Am. Chem. Soc. **138**, 5283 (2016).

[111] W. D. Stevenson, Z. Ahmed, X. B. Zeng, C. Welch, G. Ungar, and G. H. Mehl, ArXiv:1612.01180 [Cond-Mat] (2016).
[112] C. T. Archbold, R. J. Mandle, J. L. Andrews, S. J. Cowling, and J. W. Goodby, Liquid Crystals **44**, 2079 (2017).
[113] D. A. Paterson, J. P. Abberley, W. T. Harrison, J. M. Storey, and C. T. Imrie, Liquid Crystals **44**, 127 (2017).
[114] A. N. Scarbrough, M. R. Tuchband, E. D. Korblova, R. Shao, Y. Shen, J. E. Maclennan, M. A. Glaser, N. A. Clark, and D. M. Walba, Mol. Cryst. Liq. Cryst. **647**, 430 (2017).
[115] S. P. Sreenilayam, V. P. Panov, J. K. Vij, and G. Shanker, Liquid Crystals **44**, 244 (2016).
[116] R. Walker, D. Pociecha, J. P. Abberley, A. Martinez-Felipe, D. A. Paterson, E. Forsyth, G. B. Lawrence, P. A. Henderson, J. M. D. Storey, E. Gorecka, and C. T. Imrie, Chem. Commun. (2018).
[117] R. J. Mandle and J. W. Goodby, RSC Adv. **6**, 34885 (2016).
[118] R. J. Mandle and J. W. Goodby, ChemPhysChem **17**, 967 (2016).
[119] R. J. Mandle, M. P. Stevens, and J. W. Goodby, Liquid Crystals **44**, 2046 (2017).
[120] A. Al-Janabi, R. J. Mandle, and J. W. Goodby, RSC Adv. **7**, 47235 (2017).
[121] M. R. Tuchband, D. A. Paterson, M. Salamończyk, V. A. Norman, A. N. Scarbrough, E. Forsyth, E. Garcia, C. Wang, J. M. D. Storey, D. M. Walba, S. Sprunt, A. Jákli, C. Zhu, C. T. Imrie, and N. A. Clark, ArXiv:1710.00922 [Cond-Mat] (2017).
[122] C. Greco, G. R. Luckhurst, and A. Ferrarini, Soft Matter **10**, 9318 (2014).
[123] V. P. Panov, R. Balachandran, M. Nagaraj, J. K. Vij, M. G. Tamba, A. Kohlmeier, and G. H. Mehl, Appl. Phys. Lett. **99**, 261903 (2011).
[124] V. P. Panov, R. Balachandran, J. K. Vij, M. G. Tamba, A. Kohlmeier, and G. H. Mehl, Appl. Phys. Lett. **101**, 234106 (2012).
[125] C. Meyer, G. R. Luckhurst, and I. Dozov, Phys. Rev. Lett. **111**, 067801 (2013).
[126] L. Beguin, J. W. Emsley, M. Lelli, A. Lesage, G. R. Luckhurst, B. A. Timimi, and H. Zimmermann, J. Phys. Chem. B **116**, 7940 (2012).
[127] Y. Bouligand, M. O. Soyer, and S. Puiseux-Dao, Chromosoma **24**, 251 (1968).
[128] M. R. Tuchband, M. Shuai, K. A. Graber, D. Chen, L. Radzihovsky, A. Klittnick, L. Foley, A. Scarbrough, J. H. Porada, M. Moran, E. Korblova, D. M. Walba, M. A. Glaser, J. E. Maclennan, and N. A. Clark, ArXiv:1511.07523 [Cond-Mat] (2015).
[129] M. R. Tuchband, M. Shuai, K. A. Graber, D. Chen, C. Zhu, L. Radzihovsky, A. Klittnick, L. M. Foley, A. Scarbrough, J. H. Porada, M. Moran, J. Yelk, D. Bedrov, E. Korblova, D. M. Walba, A. Hexemer, J. E. Maclennan, M. A. Glaser, and N. A. Clark, ArXiv:1703.10787 [Cond-Mat] (2017).
[130] M. Salamończyk, N. Vaupotič, D. Pociecha, C. Wang, C. Zhu, and E. Gorecka, Soft Matter **13**, 6694 (2017).
[131] C. Meyer, G. R. Luckhurst, and I. Dozov, J. Mater. Chem. C **3**, 318 (2015).
[132] I. Haller, Progress in Solid State Chemistry **10**, 103 (1975).
[133] J. P. Jokisaari, G. R. Luckhurst, B. A. Timimi, J. Zhu, and H. Zimmermann, Liquid Crystals **42**, 708 (2015).
[134] B. Robles-Hernández, N. Sebastián, M. R. de la Fuente, D. O. López, S. Diez-Berart, J. Salud, M. B. Ros, D. A. Dunmur, G. R. Luckhurst, and B. A. Timimi, Phys. Rev. E **92**, 062505 (2015).
[135] C. Greco and A. Ferrarini, Phys. Rev. Lett. **115**, 147801 (2015).

[136] H. B. Kolli, G. Cinacchi, A. Ferrarini, and A. Giacometti, Faraday Discuss. **186**, 171 (2016).
[137] S. M. Shamid, S. Dhakal, and J. V. Selinger, Phys. Rev. E **87**, (2013).
[138] B. W. Klus, W. K. Bajdecki, and M. A. Karpierz, Photonics Lett. Pol. **4**, (2012).
[139] N. Vaupotič, M. Čepič, M. A. Osipov, and E. Gorecka, Phys. Rev. E **89**, (2014).
[140] E. G. Virga, Phys. Rev. E **89**, 052502 (2014).
[141] G. Barbero, L. R. Evangelista, M. P. Rosseto, R. S. Zola, and I. Lelidis, Phys. Rev. E **92**, 030501 (2015).
[142] C. Meyer and I. Dozov, Soft Matter **12**, 574 (2015).
[143] Z. P. A. Sh, S. M. Shamid, V. Borshch, P. K. Challa, M. G. Tamba, C. Welch, G. H. Mehl, J. T. Gleeson, A. Jakli, O. D. Lavrentovich, D. W. Allender, J. V. Selinger, and S. Sprunt, ArXiv:1512.03102 [Cond-Mat] (2015).
[144] P. D. Gregorio, E. Frezza, C. Greco, and A. Ferrarini, Soft Matter **12**, 5188 (2016).
[145] C. Meyer, Liquid Crystals **43**, 2144 (2016).
[146] M. A. Osipov and G. Pajak, Eur. Phys. J. E **39**, (2016).
[147] N. Vaupotič, S. Curk, M. A. Osipov, M. Čepič, H. Takezoe, and E. Gorecka, Phys. Rev. E **93**, (2016).
[148] W. Tomczyk, G. Pająk, and L. Longa, ArXiv:1606.00633 [Cond-Mat] (2016).
[149] R. S. Zola, G. Barbero, I. Lelids, M. P. Rosseto, and L. R. Evangelista, ArXiv:1602.07530 [Cond-Mat] (2016).
[150] M. P. Rosseto, R. R. R. de Almeida, R. S. Zola, G. Barbero, I. Lelidis, and L. R. Evangelista, ArXiv:1705.11176 [Cond-Mat] (2017).
[151] C. T. Imrie, G. R. Luckhurst, D. Demus, J. Goodby, G. W. Gray, H.-W. Spiess, and V. Vill, in *Handbook of Liquid Crystals Set* (Wiley-VCH Verlag GmbH, 1998), pp. 799–833.
[152] R. J. Mandle and J. W. Goodby, ChemPhysChem **17**, 967 (2016).
[153] R. J. Mandle and J. W. Goodby, RSC Adv. **6**, 34885 (2016).
[154] F. P. Simpson, R. J. Mandle, J. N. Moore, and J. W. Goodby, J. Mater. Chem. C 5102 (2017).
[155] C. T. Imrie, P. A. Henderson, and J. M. Seddon, J. Mater. Chem. **14**, 2486 (2004).
[156] G. R. Luckhurst, Macromol. Symp. **96**, 1 (1995).
[157] C. T. Imrie, P. A. Henderson, and G.-Y. Yeap, Liquid Crystals **36**, 755 (2009).
[158] C. T. Imrie and P. A. Henderson, Chem. Soc. Rev. **36**, 2096 (2007).
[159] K. Hori, M. Iimuro, A. Nakao, and H. Toriumi, J. Mol. Struct. **699**, 23 (2004).
[160] T. Sekine, T. Niori, M. Sone, J. Watanabe, S.-W. Choi, Y. Takanishi, and H. Takezoe, Jpn. J. Appl. Phys. **36**, 6455 (1997).
[161] C. Dressel, W. Weissflog, and C. Tschierske, Chem. Commun. (2015).
[162] C. Dressel, F. Liu, M. Prehm, X. Zeng, G. Ungar, and C. Tschierske, Angew. Chem. Int. Ed. **53**, 13115 (2014).
[163] J. H. Porada and D. Blunk, J. Mater. Chem. **20**, 2956 (2010).
[164] E. Barry, Z. Hensel, Z. Dogic, M. Shribak, and R. Oldenbourg, Phys. Rev. Lett. **96**, (2006).
[165] S. Parthasarathi, D. S. S. Rao, N. B. Palakurthy, C. V. Yelamaggad, and S. Krishna Prasad, J. Phys. Chem. B (2016).
[166] C. McBride and C. Vega, J. Chem. Phys. **117**, 10370 (2002).
[167] J. D. Axe, in *Solitons and Condensed Matter Physics* (Springer, 1978), pp. 234–245.
[168] R. Spal, C.-E. Chen, T. Egami, P. J. Nigrey, and A. J. Heeger, Physical Review B **21**, 3110 (1980).

[169] M. Bates and D. Frenkel, J. Chem. Phys. **109**, 6193 (1998).
[170] P. Mach, R. Pindak, A.-M. Levelut, P. Barois, H. T. Nguyen, C. C. Huang, and L. Furenlid, Phys. Rev. Lett. **81**, 1015 (1998).
[171] P. Mach, R. Pindak, A.-M. Levelut, P. Barois, H. T. Nguyen, H. Baltes, M. Hird, K. Toyne, A. Seed, J. W. Goodby, C. C. Huang, and L. Furenlid, Phys. Rev. E **60**, 6793 (1999).
[172] A.-M. Levelut and B. Pansu, Phys. Rev. E **60**, 6803 (1999).
[173] G. W. Gray, K. J. Harrison, J. A. Nash, J. Constant, D. S. Hulme, J. Kirton, and E. P. Raynes, in *Liquid Crystals and Ordered Fluids*, edited by J. F. Johnson and R. S. Porter (Springer US, 1974), pp. 617–643.
[174] V. G. K. M. Pisipati, Z. Naturforsch **58a**, 661 (2003).
[175] P. G. de Gennes and J. Prost, *The Physics of Liquid Crystals* (Clarendon Press, 1995).
[176] P. Chatelain, Acta Crystallogr. **1**, 315 (1948).
[177] P. G. De Gennes, Mol. Cryst. **7**, 325 (1969).
[178] G. Durand, L. Leger, F. Rondelez, and M. Veyssie, Phys. Rev. Lett. **22**, 1361 (1969).
[179] Orsay Liquid Crystal Group, J. Chem. Phys. **51**, 816 (1969).
[180] P. E. Cladis, D. Demus, J. Goodby, GW Gray, H.-W. Spiess **106**, 277 (1996).
[181] H. F. Gleeson and L. S. Hirst, Chem. Eur. J. of Chem. Phys. **7**, 321 (2006).
[182] P. Mach, R. Pindak, A.-M. Levelut, P. Barois, H. T. Nguyen, H. Baltes, M. Hird, K. Toyne, A. Seed, J. W. Goodby, C. C. Huang, and L. Furenlid, Phys. Rev. E **60**, 6793 (1999).
[183] F. Liu, C. Wang, J. K. Baral, L. Zhang, J. J. Watkins, A. L. Briseno, and T. P. Russell, J. Am. Chem. Soc. **135**, 19248 (2013).
[184] J. M. Virgili, Y. Tao, J. B. Kortright, N. P. Balsara, and R. A. Segalman, Macromolecules **40**, 2092 (2007).
[185] J. K. Whitesell, Chem. Rev. **89**, 1581 (1989).
[186] T. P. Yoon, Science **299**, 1691 (2003).
[187] N. M. Maier, P. Franco, and W. Lindner, J. Chromatogr. A **906**, 3 (2001).
[188] T. J. Ward and K. D. Ward, Anal. Chem. **84**, 626 (2012).
[189] J. W. Emsley, P. Lesot, G. R. Luckhurst, A. Meddour, and D. Merlet, Phys. Rev. E **87**, (2013).
[190] H. J. Coles and M. N. Pivnenko, Nature **436**, 997 (2005).
[191] H. Kikuchi, M. Yokota, Y. Hisakado, H. Yang, and T. Kajiyama, Nat Mater **1**, 64 (2002).
[192] H. Yoshida, Y. Tanaka, K. Kawamoto, H. Kubo, T. Tsuda, A. Fujii, S. Kuwabata, H. Kikuchi, and M. Ozaki, Appl. Phys. Express **2**, 121501 (2009).
[193] E. Karatairi, B. Rožič, Z. Kutnjak, V. Tzitzios, G. Nounesis, G. Cordoyiannis, J. Thoen, C. Glorieux, and S. Kralj, Phys. Rev. E **81**, 041703 (2010).
[194] M. Nakata, Y. Takanishi, J. Watanabe, and H. Takezoe, Phys. Rev. E **68**, 041710 (2003).
[195] S. M. Shamid, D. W. Allender, and J. V. Selinger, ArXiv Preprint ArXiv:1405.5584 (2014).
[196] E. Grelet, B. Pansu, M.-H. Li, and H. T. Nguyen, Phys. Rev. E **65**, (2002).
[197] J. Yamamoto, I. Nishiyama, M. Inoue, and H. Yokoyama, Nature **437**, 525 (2005).
[198] J. Xue and N. A. Clark, Phys. Rev. Lett. **64**, 307 (1990).
[199] R.-F. Shao, J. E. MacLennan, N. A. Clark, D. J. Dyer, and D. M. Walba, Liquid Crystals **28**, 117 (2001).
[200] M. Nakata, G. Zanchetta, M. Buscaglia, T. Bellini, and N. A. Clark, Langmuir **24**, 10390 (2008).
[201] H. de Vries, Acta Crystallographica **4**, 219 (1951).

[202] M. R. Tuchband, D. Chen, B. Horanyi, M. Shuai, Y. Shen, E. Korblova, D. M. Walba, N. Kapernaum, F. Giesselmann, M. A. Glaser, J. E. Maclennan, and N. A. Clark, Liquid Crystals **43**, 1083 (2016).
[203] K. Weiss, C. Wöll, and D. Johannsmann, J. Chem. Phys. **113**, 11297 (2000).
[204] M. J. Costello, R. Fetter, and M. Höchli, Journal of Microscopy **125**, 125 (1982).
[205] G. Yang, A. D. Migone, and K. W. Johnson, Physical Review B **45**, 157 (1992).
[206] M. Marinelli, F. Mercuri, U. Zammit, and F. Scudieri, Physical Review E **58**, 5860 (1998).
[207] T. Mansaré, R. Decressain, C. Gors, and V. K. Dolganov, Molecular Crystals and Liquid Crystals **382**, 97 (2002).
[208] R. Decressain, E. Cochin, T. Mansare, and M. More, Liquid Crystals **25**, 517 (1998).